# Big Bang Relic Neutrinos and Their Detection

DISSERTATION

zur Erlangung des Doktorgrades

des Fachbereichs Physik

der Universität Hamburg

vorgelegt von

BIRGIT EBERLE

aus Stuttgart

Hamburg

2005

**Abstract**

The existence of the cosmic neutrino background (C$\nu$B) is predicted by Big Bang Theory, and its properties are closely related to the ones of the cosmic microwave background, which is measured with amazing accuracy. Although belonging to the most abundant particles of the universe, the relic neutrinos evade direct detection so far.

Cosmological probes provide limits on neutrino parameters, but their sensitivity is due to the gravitational interaction of the neutrinos solely, except for Big Bang Nucleosynthesis. Furthermore, these observations require a highly model dependent interpretation and in addition do not prove the existence of the C$\nu$B of today.

In this work, we explore the feasibility to detect the cosmic neutrino background in a more direct way, i.e. by means of scattering based experiments aiming for the present day relic neutrinos. We approach the problem using different methods and take advantage of the recent improvements in the experimental bounds on the neutrino masses and mixings as well as the cosmological parameters. For the detection of the low energetic relic neutrino flux at Earth by elastic scattering on nuclei in a torsion balance experiment, experimental progress beyond the estimates for the next decade is required. C$\nu$B detection via inverse beta decay at hadron colliders presents no promising option for the conceivable future. The most promising approach to detect the C$\nu$B within the next decade, is provided by the analysis of absorption dips in the extreme energy cosmic neutrino (EEC$\nu$) flux. For these to be revealed with statistics sufficient for C$\nu$B detection, almost certainly a quasi-degenerate neutrino mass spectrum and a flux as large as the cascade limit are required. Absorption dips are most sensitive to neutrino properties, therefore they can be claimed to present the most solid proof of the C$\nu$B.

# Contents

# Chapter 1

# Introduction

Big Bang relic neutrinos are theoretically predicted to be the second most abundant particles in the universe after the photons. Since neutrinos interact only weakly, they decoupled, when the universe was just one second old, and exist since then. The decoupled neutrinos attended Big Bang Nucleosynthesis in the first minutes of the universe, the epoch of recombination $\sim 380000$ years later, when the cosmic microwave background was imprinted on the last scattering surface in the sky, and the epoch of large scale structure formation at the universe's age of $\sim 10^9$ years. Today, the relic neutrinos properties might still carry a signature of the universe at their decoupling time. The impact of the C$\nu$B on the universe's history is already measured by cosmological probes and the resulting bounds on neutrino properties are quite stringent. However, these results are highly model dependent and – except for Big Bang Nucleosynthesis – sensitive to the gravitational impact of the neutrinos solely, ignoring the characteristical weak interactions of the neutrinos. Furthermore, these experiments probe the features of the cosmic neutrino background in earlier stages of the universe but not in the present time.

Fortunately, experimental neutrino physics and cosmology belong to the most rapidly evolving areas in physics. The revolutionary findings are, in short, that neutrinos have mass and that we live in a flat, cold dark matter universe with cosmological constant. With these updated parameters, it is worthwhile to investigate the feasibility to detect the C$\nu$B in a more direct way by means of scattering based experiments. In this work, we analyze the C$\nu$B detection potential for Earth based torsion balances, for experiments utilizing a hadron collider beam, and for methods employing astrophysical sources, ranging from the lowest to the highest energies.

The outline of this work is as follows. In the first part, we present general neutrino properties followed by features of neutrinos in cosmology, with a theoretical introduction and parameters measured by experiments, respectively. In the second part, we explore the possibility to detect the C$\nu$B via neutrino-nucleon scattering.

We calculate the force on a torsion balance induced by the relic neutrino flux and examine C$\nu$B induced inverse beta decay processes at hadron colliders. In the third part, we investigate neutrino-neutrino scattering based methods invoking astrophysical sources. We study the emission and absorption features of extreme energetic neutrinos on the cosmic neutrino background due to resonant annihilation at the $Z$-resonance.

# Part I

# About Neutrinos

# Chapter 2

# Neutrino properties

In the last few years, we have learned that neutrinos produced in a well-defined flavor eigenstate can be detected, after traveling a macroscopic distance, in a different flavor eigenstate. Furthermore, it has been established that the probability of flavor change $P(\nu_\alpha \to \nu_\beta)$ depends on the energy and propagation distance of the neutrinos. The simplest interpretation of this phenomenon is that neutrinos have distinct, nonzero masses and that the mass eigenstates are different from the weak eigenstates. This being the case, neutrinos undergo oscillations and $P(\nu_\alpha \to \nu_\beta)$ is the oscillation probability.

In this chapter, we present the theoretical basics of neutrino features as well as the experimental results.

Throughout this work, we use the convention $\hbar = c = 1$.

## 2.1 Theoretical Basics

In the following we give a brief theoretical overview over the very basics of neutrino physics. We start with the Standard Model interactions, proceed to masses and end with the mixing matrix.

### 2.1.1 Standard Model Interactions

The Standard Model (SM) interactions of neutrinos are in excellent agreement with experimental data for energies up to a few hundred GeV. The Standard Model Charged Current (CC) and Neutral Current (NC) Lagrangians are given by

$$\mathcal{L}_I^{\mathrm{CC}} = -\frac{g}{2\sqrt{2}} j_\alpha^{\mathrm{CC}} W^\alpha + \mathrm{h.c.} \,, \tag{2.1}$$

$$\mathcal{L}_I^{\mathrm{NC}} = -\frac{g}{2\cos\theta_W} j_\alpha^{\mathrm{NC}} Z^\alpha + \mathrm{h.c.} \,, \tag{2.2}$$

with $g = e/\sin\theta_W$ being the weak $SU(2)_W$ Standard Model coupling, $e$ being the absolute value of the electron charge, $\theta_W$ the Weinberg (weak mixing) angle, $W^\alpha$ and $Z^\alpha$ the fields of charged $W^\pm$ and neutral $Z^0$ vector bosons, $j_\alpha^{\rm CC}$ the leptonic charged current and $j_\alpha^{\rm NC}$ the neutrino neutral current,

$$j_\alpha^{\rm CC} = \sum_l \bar{\nu}_{lL}\, \gamma_\alpha\, l_L \qquad \text{and} \qquad j_\alpha^{\rm NC} = \sum_l \bar{\nu}_l\, \gamma_\alpha\, \nu_{lL}\,, \tag{2.3}$$

respectively, where the subscript $l$ denotes the flavor eigenstate ($e$, $\mu$, $\tau$) and the subscript $L$ denotes the left-handed chirality eigenstate. Due to experimental evidence, only left-chiral neutrinos interact. In the Standard Model, neutrinos are strictly massless and consequently right-chiral neutrinos do not exist.

For energies far below the $Z$ and $W$ poles, the weak interactions effectively reduce to four fermion interactions with the Fermi-coupling constant

$$\frac{G_F}{\sqrt{2}} = \frac{1}{8}\frac{g^2}{M_W^2} = \frac{1}{8}\frac{g^2}{\cos^2\theta_W\, M_Z^2}\,, \tag{2.4}$$

which is $G_F = 1.166 \times 10^{-5}\ \text{eV}^2$.

## 2.1.2 Neutrino Masses

Extending the description beyond the Standard Model, we consider the inclusion of masses of the neutrinos. In addition to the active neutrinos, $\nu_L$, i.e. left-chiral neutrinos transforming as $SU(2)_W$ doublet components, we allow for sterile neutrinos $N_R$, which are defined as right-chiral neutrinos transforming as $SU(2)_W$ singlets, i.e. they participate in no interactions except for Higgs and beyond the Standard Model interactions.

Mass terms arise due to the coupling of fields of opposite chiralities. For three families, the most general neutrino mass term can be written using a $(6 \times 6)$ mass matrix as

$$\mathcal{L}_m = \frac{1}{2}(\bar{\nu}_L\ \bar{N}_L^c) \begin{pmatrix} m_T & m_D \\ m_D^t & m_S \end{pmatrix} \begin{pmatrix} \nu_R^c \\ N_R \end{pmatrix} + \text{h.c.}\,, \tag{2.5}$$

where $\nu = (\nu_e,\, \nu_\mu,\, \nu_\tau)$ and $N = (N_e,\, N_\mu,\, N_\tau)$ represent a three flavor component vector of active and sterile neutrinos, respectively, while $\nu_R^c$ and $N_L^c$ denote their corresponding CPT conjugates.

The Dirac mass term in Eq. (2.5), $m_D \bar{\nu}_L N_R + h.c.$, connects an active with a sterile anti-neutrino and vice versa, i.e. coupling two distinct spinors. If the other contributions vanish, $m_S = m_T = 0$, the neutrinos are Dirac particles, and a conserved lepton number can be formulated.

The Majorana mass terms in Eq. (2.5), $\frac{1}{2} m_T \bar{\nu}_L \nu_R^c + h.c.$ for the active and $\frac{1}{2} m_S \bar{N}_L^c N_R + h.c.$ for the sterile neutrinos, connect neutrinos with their own CPT conjugates, which

7

implies lepton flavor violation.

In general both, Majorana and Dirac mass terms, can be involved. For example, the hierarchy $m_S(m_T) \ll m_D$ leads to two quasi-degenerate Majorana neutrinos (pseudo-Dirac). Another well-known example is the sea-saw model with $m_S \gg m_D$ and $m_T = 0$, which generates a large and very small neutrino mass scale in a natural way.

### 2.1.3   Neutrino Mixing and Flavor Change

The diagonalization of the neutrino mass matrix determines the neutrino masses $m_i$ as well as the corresponding neutrino mass eigenstates $\nu_i$ in terms of the flavor eigenstates $\nu_\alpha$,

$$\nu_i = \sum_\alpha U_{i\alpha} \nu_\alpha , \qquad (2.6)$$

where $U$ is the mixing matrix. The standard parameterization of the leptonic (Pontecorvo, Maki, Nakagawa, Sakata) mixing matrix $U_{PMNS}$ for the restricted case of three active neutrinos reads [1]

$$U_{PMNS} =$$

$$
\begin{array}{cccc}
 & \nu_1 & \nu_2 & \nu_3 \\
\begin{array}{c} \nu_e \\ \nu_\mu \\ \nu_\tau \end{array} &
\left( \begin{array}{ccc}
c_{12}c_{13} & s_{12}c_{13} & s_{13}e^{-i\delta} \\
-s_{12}c_{23} - c_{12}s_{23}s_{13}e^{i\delta} & c_{12}c_{23} - s_{12}s_{23}s_{13}e^{i\delta} & s_{23}c_{13} \\
s_{12}s_{23} - c_{12}c_{23}s_{13}e^{i\delta} & -c_{12}s_{23} - s_{12}c_{23}s_{13}e^{i\delta} & c_{23}c_{13}
\end{array} \right)
\end{array}
$$

$$\times \operatorname{diag} \left( \mathrm{e}^{-i\alpha_1/2}, \mathrm{e}^{-i\alpha_2/2}, 1 \right), \qquad (2.7)$$

with $c_{ij} \equiv \cos\theta_{ij}$ and $s_{ij} \equiv \sin\theta_{ij}$, where $\theta_{ij}$ are the three mixing angles, while $\delta$, $\alpha_1$ and $\alpha_2$ are the $CP$-violating phases. The Majorana phases $\alpha_1$ and $\alpha_2$ have physical consequences only if neutrinos are Majorana particles.

Since neutrinos are produced and detected as flavor eigenstates, which in general differ from their mass eigenstates, flavor change can occur by propagation. Using a quantum mechanical Ansatz, the time evolution is given by the Schrödinger equation

$$|\nu_i(t)\rangle = e^{-i(E_i t - p_i L)} |\nu_i\rangle , \qquad (2.8)$$

and the probability of $\nu_\alpha \to \nu_\beta$ transitions evaluates as

$$P(\nu_\alpha \to \nu_\beta) = |\langle \nu_\beta | \nu_\alpha(L)\rangle|^2 = |\sum_i U_{\alpha i}^* \exp(-i\Delta m_i^2 \, L/2E) \, U_{\beta i}|^2 \qquad (2.9)$$

$$= \delta_{\alpha\beta} + 2 \sum_{i>j} \operatorname{Re} \left[ U_{\alpha i}^* U_{\beta i} U_{\alpha j} U_{\beta j}^* \left( \exp(-i\Delta m_{ij}^2 L/2E) - 1 \right) \right],$$

which describes neutrino oscillations in terms of the mass squared differences $\Delta m_{ij}^2 = m_i^2 - m_j^2$, the propagation length $L$ and the neutrino energy $E$.

If neutrinos travel through matter, their interactions with it can significantly modify their propagation. The interplay between (flavor-non-changing) neutrino-matter interactions and neutrino mixings, account for a particular flavor change behavior, known as the Mikheyev-Smirnov-Wolfenstein (MSW) effect [2, 3].

The $\nu_e$–$\nu_e$ element of the Hamiltonian $\mathcal{H}$ contains the interaction energy

$$V \;=\; \sqrt{2}\,G_F\,N_e \tag{2.10}$$

arising from CC $\nu_e$ scattering off ambient electrons with $N_e$ being their density. The NC interactions $\nu_e$–$\nu_e$, $\nu_\mu$–$\nu_\mu$ and $\nu_\tau$–$\nu_\tau$ are flavor independent. Excluding active-sterile mixing, this common interaction energy simply adds a multiple of the identity matrix to the Hamiltonian $\mathcal{H}$ and hence has no effect on flavor transitions. The Hamiltonian in $\nu_e$–$\nu_x$-space is given by

$$\begin{aligned}
\mathcal{H}(r) &= \mathcal{H}_V + \mathcal{H}_M(r) \\
&= \frac{\Delta m^2}{4E}\left( \begin{array}{cc} -\cos 2\theta & \sin 2\theta \\ \sin 2\theta & \cos 2\theta \end{array} \right) + \left( \begin{array}{cc} V(r) & 0 \\ 0 & 0 \end{array} \right),
\end{aligned} \tag{2.11}$$

where $\mathcal{H}_V$ is the Hamiltonian in vacuum and $\mathcal{H}_M(r)$ its modification due to matter, where $r$ accounts for possible spatial variation in the matter density.

## 2.2  Measurements of Neutrino Parameters

Up-to-date neutrino data [4, 5, 6, 7] can be explained by three flavor neutrino oscillations, with the exception of the LSND anomaly [8]. We will ignore the latter in the following, except for Subsec. 2.2.4, where we will comment on the LSND anomaly.

### 2.2.1  Neutrino Mixing Parameters

The leptonic mixing matrix $U_{PMNS}$ is very different from the quark mixing matrix. Whereas the latter has small mixing angles, two of the leptonic mixing angles are large. Detailed combined analyses of all neutrino data are consistent, at 3-$\sigma$ confidence level [9] with:

- $\sin^2 \theta_{12} = 0.30 \pm 0.08$, mostly from solar and KamLAND data;

- $\sin^2 \theta_{23} = 0.50 \pm 0.18$, mostly from atmospheric neutrino data;

- $\sin^2 \theta_{13} \leq 0.047$, mostly from atmospheric and Chooz data.

The CP violating phases $\delta$, $\alpha_1$ and $\alpha_2$ are not measured. Some linear combination of $\alpha_1$ and $\alpha_2$ may be revealed in neutrinoless double beta decay experiments. The phase $\delta$ may be measurable in oscillation experiments, if $\theta_{13} \neq 0$. A better knowledge of $\theta_{13}$ would be preferable for that purpose.

### 2.2.2 Neutrino Mass Spectrum

The neutrino mass spectrum is experimentally not determined – the hierarchy could either be normal or inverted, which is not determined, and neither is the absolute mass scale known.

**Mass Squared Splittings**

One of the key result of the oscillation experiments are the mass squared splittings. In order to relate the elements of the oscillation probability (2.9) to experimental observables, it is necessary to define the neutrino mass eigenstates, i.e. to "order" the neutrino masses. In this part[1], this will be done in the following way: $m_2^2 > m_1^2$ and $\Delta m_{21}^2 < |\Delta m_{31}^2|$.
Combined analyses of neutrino data [9] offer the following results:

- $\Delta m_{21}^2 = (8.1 \pm 1.0) \times 10^{-5}$ eV$^2$, mostly from solar and KamLAND data;

- $|\Delta m_{31}^2| = (2.2 \pm 1.0) \times 10^{-3}$ eV$^2$, mostly from atmospheric neutrino data.

Depending on the sign of $\Delta m_{31}^2$, one may have either a normal hierarchy, which is analogous to the quarks and charged leptons, or the inverted hierarchy. Quasi-degenerate patterns refer to the possibility that the overall mass scale is large compared to the mass differences.
Both the absolute mass scale and the sign of $\Delta m_{31}^2$ are not determined by present-day experiments. As discussed in the following, other than oscillation experiments pose limits on the absolute scale, whereas the sign of $\Delta m_{31}^2$ is unknown up to now – we will discuss its possible observability at future experiments in subsection 2.2.2.

**Absolute Scale of the Neutrino Mass**

The absolute scale of neutrino masses can be probed in endpoint spectrum measurements of (e.g. tritium) beta decay, which measure the quantity

$$m_\beta^2 \;=\; \sum_i |U_{ei}|^2 m_i^2 \,. \tag{2.12}$$

---

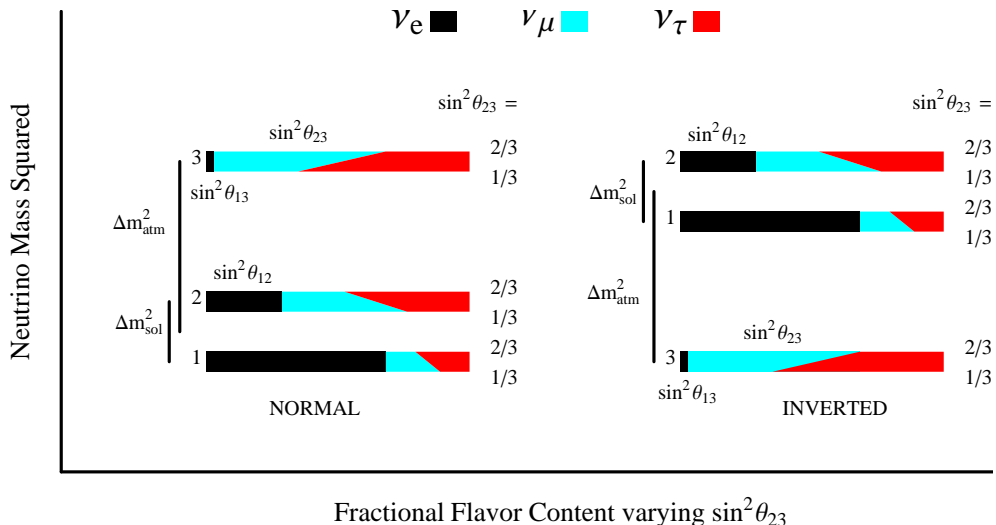[1]Note, that in the part II and III, we will denote throughout the smallest neutrino mass with $m_{\nu_1}$.

Figure 2.1: Flavor content of the neutrino mass eigenstates for variation of $\sin^2\theta_{23}$ from the minimum allowed value of $\approx 1/3$ (bottom of the bars) to the maximum allowed value $\approx 2/3$ (top of the bars), using the following fixed values for the other mixing parameters: $\sin^2\theta_{12} = 0.30$, $\sin^2\theta_{13} = 0.03$ and $\delta = \pi/2$. From Ref. [10].

The present upper limit is $m_\beta < 2.23$ eV at the confidence level 95% [11], whereas the future KATRIN experiment should be sensitive to $m_\beta \sim 0.2$ eV [12].

Cosmological large scale structure (LSS) observations are sensitive to

$$\sum_i m_i \,. \tag{2.13}$$

Combining cosmic microwave background (CMB) with LSS data yields $\sum m_i \lesssim 1.2$ eV [13], while including more data sets pushes the limit down to $\sum m_i \lesssim 0.42$ eV [14]. These limits are much more stringent than those obtained from tritium beta decay experiments, but also much more model dependent – more on that topic will be presented in the next chapter, see Subsec. 3.1.6.

The neutrinoless double beta decay amplitude is proportional to the effective mass

$$m_{\beta\beta} \;=\; \sum_i U_{ei}^2 m_i \,. \tag{2.14}$$

There is a claimed observation [15] of neutrinoless double beta decay corresponding to $0.17 < m_{\beta\beta} < 2.0$ eV. If confirmed, this would imply, that the neutrino masses are degenerate. Proposed experiments would be sensitive to $m_{\beta\beta} \sim 0.02$ eV, while a significant uncertainty due to the nuclear matrix element would remain for the case that events of that type are actually observed.

11

**Pattern**

Eventually it will be possible to distinguish the normal and inverted hierarchies with long baseline (LBL) experiments, where the neutrinos traverse Earth matter. The interaction energy $V$ (2.10) changes sign, if we consider antineutrinos instead of neutrinos. Using the known values for $|\Delta m^2_{31}|$ and $\theta_{13}$, this implies, that for $\Delta m^2_{31} > 0$ ($\Delta m^2_{31} < 0$) the transition probability $P(\nu_e \to \nu_\mu)$ is enhanced (suppressed) and $P(\bar{\nu}_e \to \bar{\nu}_\mu)$ is suppressed (enhanced) by matter effects. Thus a comparison of the $\nu_e \to \nu_\mu$ CC rate with the $\bar{\nu}_e \to \bar{\nu}_\mu$ CC rate discriminates between the two signs of $\Delta m^2_{31}$.

### 2.2.3  Majorana Versus Dirac

The only practical way to distinguish Majorana and Dirac masses of neutrinos experimentally is given by neutrinoless double beta decay. Its observation would imply Majorana masses. Unfortunately, the converse is not true – non-observation of neutrinoless double beta decay could be either due to Dirac masses or due to a an invisibly small $m_{\beta\beta}$ in a normal hierarchy.

### 2.2.4  The Number of Neutrinos

The most precise measurements of the number of light active neutrinos $N_\nu$ originate from studies of $Z$ boson production in $e^+e^-$ collisions at LEP. The invisible width $\Gamma_{\text{inv}}$ of the $Z$ boson is assumed to be due to $N_\nu$ light neutrino species. In order to reduce the model dependence, the ratio of the neutrino to charged leptonic partial widths in the Standard Model, $(\Gamma_\nu/\Gamma_l)_{\text{SM}}$ rather than $(\Gamma_\nu)_{\text{SM}}$ is used to determine the number of light neutrino types:

$$N_\nu \;=\; \frac{\Gamma_{\text{inv}}}{\Gamma_l}\left(\frac{\Gamma_l}{\Gamma_\nu}\right)_{\text{SM}}. \tag{2.15}$$

The combined result from the four LEP experiments is $N_\nu = 2.984 \pm 0.008$ [16] for active neutrinos with masses below 45 GeV.

A complementary constraint is given by big bang nucleosynthesis (BBN). The predicted $^4$He abundance depends sensitively on the competition between weak and expansion rates, and therefore on the number of relativistic particles at the time of BBN, $T \sim 1$ MeV. The result is $2.67 \lesssim N_{\text{eff}} \lesssim 3.85$ [17], where $N_{\text{eff}}$ counts the effective number of neutrinos with masses below 1 MeV. More on that topic will be presented in the next chapter, see Subsec. 3.1.3.

The LSND experiment measured the neutrino flux produced by positively charged pion decay – in the Standard Model given by: $\pi^+ \to \mu^+\nu_\mu \to e^+\nu_e\bar{\nu}_\mu\nu_\mu$ – and observed a small $\bar{\nu}_e$ flux. Interpreted in terms of oscillations, the LSND anomaly points

12

to a mass squared difference $\Delta m_{\rm LSND}^2 \sim 1$ eV$^2$. If there are three neutrino mass eigenstates, the condition $\Delta m_{21} + \Delta m_{13} + \Delta m_{32} = 0$ must be fulfilled. Obviously, $\Delta m_{\rm LSND}^2$ cannot be the missing mass squared difference $\Delta m_{32}^2$ within the $3\nu$ framework, therefore this observation strongly suggests the existence of one or more light sterile neutrinos. A combination of solar, KamLAND, reactor and accelerator data exclude both, the (2+2) and the (3+1) schemes [18]. Other possible explanations of the LSND anomaly are the $5\nu$ scenario [19] or the violation of CPT [20, 21].

The MiniBooNE experiment at Fermilab is aimed at confirming or refuting the LSND result. It is already taking data.

# Chapter 3

# Neutrinos and Cosmology

In the first section of this chapter, a very brief introduction to cosmology is presented. In the second section, the impact of the cosmic neutrino background on the evolutionary history of the universe in different epochs is explained, including the corresponding neutrino parameters determined by cosmological probes.

## 3.1  Cosmology Basics

In this section we provide the cosmological basics first and end with a subsection dedicated to the standard cosmic neutrino background history as provided by big bang theory. More can be found in e.g. [22, 23].

### 3.1.1  Geometry

The universe we observe is homogeneous and isotropic on large scales. The most general space time metric consistent with that is the Friedmann-Robertson-Walker (FRW) metric, which can be written in the form

$$ds^2 \;\; = \;\; dt^2 - a^2(t) \left( \frac{dr^2}{1 - k\,r^2} + r^2(d\theta^2 + \sin^2\theta d\phi^2) \right), \qquad (3.1)$$

where $a(t)$ is the cosmic scale factor, normalized such that $k$ is equal to $+1$, $-1$ or $0$, referring to an open, closed or flat universe, respectively. The comoving coordinates are $t$, $r$, $\phi$ and $\theta$, such that an observer at rest in the comoving frame remains at rest ($r$, $\phi$ and $\theta = $ const.) as the universe expands.
The Einstein equations are given by

$$R_{\mu\nu} - \frac{1}{2}g_{\mu\nu}R \;\; = \;\; 8\pi G T_{\mu\nu} + \Lambda g_{\mu\nu}, \qquad (3.2)$$

where $R_{\mu\nu}$ is the Ricci tensor, $R = g_{\mu\nu}R_{\mu\nu}$ the Ricci scalar, $\Lambda$ is the cosmological constant, $g_{\mu\nu}$ is the metric tensor, $T_{\mu\nu}$ is the stress-energy tensor and $G = m_P^{-2}$ the gravitational coupling constant with the Planck mass $m_P$. For the homogeneous and isotropic distribution of matter, the stress-energy tensor becomes that of a perfect fluid

$$
\begin{aligned}
T_0^0 &= \rho \\
T_i^j &= -p\delta_i^j \,.
\end{aligned}
\tag{3.3}
$$

In this case the Einstein equations reduce to the so called Friedmann equations

$$
H^2 \equiv \left(\frac{\dot{a}}{a}\right)^2 = \frac{8\pi\,G}{3}\sum_i \rho_i - \frac{k}{a^2} + \frac{\Lambda}{3}
\tag{3.4}
$$

$$
\frac{\ddot{a}}{a} = -\frac{4\pi G}{3}\sum_i (\rho_i + 3p_i) + \frac{\Lambda}{3}
\tag{3.5}
$$

where $H$ is the Hubble parameter and $i$ indexes all possible types of energy in the universe. From (3.4) and (3.5) the covariant law of energy conservation follows,

$$
\dot{\rho} + 3H(\rho + p) = 0.
\tag{3.6}
$$

For the simple equation of state $p = w\rho$, where $w$ is independent of time, the energy density evolves as

$$
\rho(a) \propto a(t)^{-3(1+w)}\,.
\tag{3.7}
$$

For radiation, the equation of state parameter is $w_R = 1/3$, for matter $w_M \simeq 0$ and for a cosmological constant it is[1] $w_\Lambda = -1$.
Similarly, it is sometimes convenient to think of any nonzero spatial curvature as a component of the cosmological energy budget with $w_k = -1/3$.
The critical or closure energy density is expressed as

$$
\rho_c = \frac{3H^2}{8\pi G}\,,
\tag{3.8}
$$

which corresponds to a flat universe, i.e. $k = 0$.
Defining the energy content of the universe in terms of the critical energy density as the density parameter,

$$
\Omega_i = \rho_i/\rho_c\,,
\tag{3.9}
$$

---

[1]The equation of state parameter of the vacuum energy is a key parameter for the fate of the universe, therefore, it is common to use $w$ to stand for this vacuum equation of state. In general, this $w$ of a vacuum energy does not need to be $w = -1$ and also does not need to be constant.

$\Omega_{\text{tot}} > 1$ corresponds to $k = +1$, $\Omega_{\text{tot}} = 1$ to $k = 0$ and $\Omega_{\text{tot}} < 1$ to $k = -1$. Then, the evolution of the expansion rate can be written in terms of its values today,

$$H^2(z) = H_0^2 \left( \Omega_R (1+z)^4 + \Omega_M (1+z)^3 + \Omega_k (1+z)^2 + \Omega_\Lambda \right) , \qquad (3.10)$$

where $\Omega_i$ are the present-day energy densities in terms of the critical energy of radiation, matter, curvature and cosmological constant, respectively, and $H_0$ is the Hubble constant. Note that throughout this work, present-day parameters are denoted by the subscript zero.

In Eq. (3.10), we have introduced the redshift $z$ by the definition $a_0/a = (1+z)$. The scale parameter of today $a_0$, corresponds to $z = 0$. Usually – and that is where the name comes from – redshift is introduced by the ratio of wavelengths. The wavelength $\lambda_0$ of a photon observed today over the wavelength $\lambda$ of the same photon emitted at distance $z$, defines redshift by the following relation $\lambda_0/\lambda \equiv (1+z)$. As the universe expands, de Broglie wavelengths are stretched in the same way, thus the time evolution of undisturbed momenta is given by $p(z) = p_0/(1+z)$.

In cosmology, redshift is often used as a time equivalent $dz = (1+z) H(z) \, dt$, where $t = r/c$ is the time, that a photon needs to travel the distance $r$.

From equation (3.10), we can read off the evolution of the expansion rate of the universe – again assuming, that $w$ and therefore $\Omega_i$ is constant[2]. At early times, the universe was radiation dominated, at some point in time, matter started to dominate over radiation, and even later, curvature may take over, if a cosmological constant did not already do so

## 3.1.2 Thermodynamics

The number density $n$, the energy density $\rho$ and the pressure $p$ of a dilute, weakly-interacting gas of particles with $g$ internal degrees of freedom is given in terms of its phase space distribution function $f(\vec{p})$:

$$n = \frac{g}{(2\pi)^3} \int f(\vec{p}) \, d^3 p \qquad (3.11)$$

$$\rho = \frac{g}{(2\pi)^3} \int E \, f(\vec{p}) \, d^3 p \qquad (3.12)$$

$$p = \frac{g}{(2\pi)^3} \int \frac{|\vec{p}|^2}{3E} \, f(\vec{p}) \, d^3 p \qquad (3.13)$$

where $E^2 = |\vec{p}|^2 + m^2$. For species in equilibrium the phase space distribution function $f$ is given by

$$f(\vec{p}) = \left[ \exp((E - \mu)/T) \pm 1 \right]^{-1} , \qquad (3.14)$$

---

[2]The evolution with time may be due to a time dependent dark energy component, or due to the fact, that relativistic particles become nonrelativistic.

where $\mu$ is the chemical potential and $T$ the temperature. The upper sign $+1$ pertains to Fermi-Dirac species and the lower sign $-1$ to Bose-Einstein species. We assume in the following until otherwise stated, that the chemical potentials are zero. In the relativistic limit $(T \gg m)$ we get

$$
n = \begin{cases} \frac{\zeta(3)}{\pi^2} g\, T^3 & \text{Bosons} \\ \frac{3}{4} \frac{\zeta(3)}{\pi^2} g\, T^3 & \text{Fermions} \end{cases} \tag{3.15}
$$

$$
\rho = \begin{cases} \frac{3\zeta(4)}{\pi^2} g\, T^4 & \text{Bosons} \\ \frac{7}{8} \frac{3\zeta(4)}{\pi^2} g\, T^4 & \text{Fermions} \end{cases} \tag{3.16}
$$

$$
p = \frac{1}{3}\,\rho\,, \tag{3.17}
$$

where $\zeta(3) = 1.20206\ldots$ is the Riemann zeta function of 3 and $\zeta(4) = \pi^4/90$. In the non-relativistic limit $(T \ll m)$ the number density, energy density and pressure are the same for Bosons and Fermions

$$
n = g \left( \frac{m\,T}{2\pi} \right)^{3/2} \exp\left( -m/T \right) \tag{3.18}
$$

$$
\rho = mn \tag{3.19}
$$

$$
p = nT \ll \rho\,. \tag{3.20}
$$

The average energy per particle for a relativistic species derives as

$$
\langle\, E\,\rangle \equiv \frac{\rho}{n} = 3\,\frac{\zeta(4)}{\zeta(3)}\,T \qquad \text{Bosons} \tag{3.21}
$$

$$
\langle\, E\,\rangle \equiv \frac{\rho}{n} = \frac{7}{2}\,\frac{\zeta(4)}{\zeta(3)}\,T \qquad \text{Fermions} \tag{3.22}
$$

and for a non-relativistic species

$$
\langle\, E\,\rangle = m + (3/2)\,T\,. \tag{3.23}
$$

The energy density of a non-relativistic species is exponentially suppressed, therefore, the total energy content in the early universe may be written as – or in general the energy density in radiation

$$
\rho_R = \frac{3\,\zeta(4)}{\pi^2}\,g_*\,T^4\,, \tag{3.24}
$$

where the $g_*$ counts the number of relativistic degrees of freedom

$$
g_* = \sum_{i=\text{bosons}} g_i \left( \frac{T_i}{T} \right)^4 + \frac{7}{8} \sum_{i=\text{fermions}} g_i \left( \frac{T_i}{T} \right)^4\,, \tag{3.25}
$$

summed over species and spin states, where the factor 7/8 accounts for the difference in Fermi and Bose statistics.

In local thermal equilibrium, the entropy in a comoving volume $S = a^3 (\rho + p)/T$ is conserved[3], $dS = 0$, and therefore a fiducial and useful quantity. Since it is dominated by the contribution of relativistic particles, the entropy can written to a good approximation as

$$ S = \frac{2\pi^2}{45} g_{*S} T^3 a^3 \,, \tag{3.26} $$

where

$$ g_{*S} = \sum_{i=\text{bosons}} g_i \left(\frac{T_i}{T}\right)^3 + \frac{7}{8} \sum_{i=\text{fermions}} g_i \left(\frac{T_i}{T}\right)^3 \,, \tag{3.27} $$

which is equivalent to $g_*$, if all particles have a common temperature $T$.

If massive particles would remain in thermal equilibrium until the present, its abundances would be absolutely negligible because of the exponential factor $n \propto (m/T)^{3/2} \exp(-m/T)$. However, the interactions of a certain species freeze out when the interaction rate $\Gamma$ becomes smaller than the expansion rate $H$.

### 3.1.3 Big Bang Nucleosynthesis

At **T = 10 MeV**, the relativistic degrees of freedom in the universe are photons, neutrinos, electron and positrons, such that $g_* = 10.75$. All the weak rates are much larger than the expansion rate, such that the neutron to proton ratio $(n_n/n_p) \equiv n/p \simeq 1$. The light elements are in equilibrium, but their abundances are very small due to the fact that the baryon-to-photon-ratio $\eta = n_B/n_\gamma \simeq 6 \times 10^{-10}$ is small.

Around **T = 2.5 MeV**, neutrinos decouple. Shortly thereafter, at around $T \simeq m_e/3 \simeq 170$ keV, the $e^\pm$ pairs annihilate, transferring their entropy to the photons. At about this time, the weak interaction rates that interconvert neutrons to protons freeze out and the neutron to proton ratio is given by

$$ (n/p)_{\text{freeze}} = \exp(-Q/T_F) \simeq 1/6 \,, \tag{3.28} $$

with the freeze-out temperature $T_F \simeq 1$ MeV and the mass difference of neutron to proton $Q = m_n - m_p \simeq 1.29$ MeV.

After freeze-out, the neutron to proton ratio decreases due to occasional weak interaction and free neutron decay. The light nuclear species are still in nuclear statistical equilibrium with very small abundances.

---

[3]We have assumed that the chemical potentials are negligible, $|\mu| \ll T$.

Around $\mathbf{T} = \mathbf{0.3}$ to $\mathbf{0.1}$ $\mathbf{MeV}$ : At this time, $g_*$ has decreased to its present-day value, $g_* = \sim 3.36$, and the neutron to proton ratio is $(n/p)_{\mathrm{nuc}} \simeq 1/7$. When the number density of those photons, that have enough energy to photo-dissociate deuterium has decreased so far that it is comparable to the baryon density – the so-called light element bottleneck is broken – Big Bang Nucleosynthesis (BBN) seriously begins.

The number densities are too low to allow nuclei to be produced in many-body reactions. Instead, they must be built up in sequences of two-body reactions. The light elements D, $^3$He and $^3$H build up and $^4$He is then synthesized rapidly. Essentially all available neutrons get bound into $^4$He, which is the most tightly bound light species. Therefore, the number of $^4$He after nucleosynthesis is one half of the number of neutrons before nucleosynthesis $(n/p)_{\mathrm{nuc}}$ and a rough estimate gives for the mass fraction $X_A = A\, n_A / N_N$ of $^4$He

$$X_4 \equiv \frac{4n_4}{n_N} = \frac{4(n_n/2)}{n_n + n_p} = \frac{2(n/p)_{\mathrm{nuc}}}{1 + (n/p)_{\mathrm{nuc}}} \simeq \frac{1}{4}\,. \tag{3.29}$$

Some $^7$Li is synthesized, but no significant synthesis of heavier elements takes place. At this time, when the fuel for synthesizing heavier elements, $^4$He, is provided, Coulomb-barrier suppression, which rises with decreasing temperature, is very significant. This fact, together with the absence of tightly bound isotopes with mass 5 and 8 and the negligible rate of many body reactions, suppresses the synthesis of heavier elements.

Furthermore, substantial amounts of D and $^3$He are left unburned, since the rates for the reactions to burn them to $^4$He become small as the mass fractions $X_2$, $X_3$ become small and the reactions freeze out. Since these rates are proportional to the baryon to photon ratio $\eta$, the unburned abundances of D and $^3$He should decrease with increasing $\eta$.

The four light nuclides D, $^3$He, $^4$He, $^7$Li follow different evolutionary paths in the post-BBN universe.

Deuterium gets destroyed – burned to $^3$He and further – as it passes through a star. Therefore, the actual abundance serves as a lower limit to the primordial value. It can be observed in "young" systems, in high redshift, low-metallicity absorption line systems, where its value should be very close to its primordial one.

For $^3$He, the post-BBN evolution is much more complex. The more tightly bound $^3$He with a larger Coulomb barrier is more robust than D to nuclear burning. But in stars, $^3$He is burned to $^4$He and beyond. This processing should have increased since the big bang and since formation of the solar system. Its dependence on stellar processing should also be visible in a gradient in abundance with galactocentric distance. None of this is observed. However, there are model-dependent uncertainties, therefore the

abundance of $^3$He does not serve as a good measure for cosmological parameters.

In the post-BBN epochs, $^3$He gets burned to $^4$He. Therefore, the $^4$He abundance observed today can serve as an upper bound to the primordial value. It is observed in extragalactic, low-metallicity regions.

$^7$Li is fragile, therfore easily destroyed as it cycles through stars. As with the other light nuclei, the dominant uncertainties are systematics.

### 3.1.4 Density Perturbations

A given density perturbation – wherever it may come from, this is the question of the initial conditions – is either larger than the horizon (superhorizon scale) or smaller (subhorizon scale) at a certain time. Since the length scale of a perturbation grows as the universe expands, but the horizon grows faster, a given superhorizon perturbation will enter the horizon at a certain point in time.

On superhorizon scales, there is no causal connection. Therefore, a given perturbation pertains its initial configuration - and may give hints, if observed, to the initial conditions of the universe, which are commonly assumed to be either curvature perturbations (adiabatic) or isocurvature perturbations (isothermal).

On subhorizon scales, things are causally connected. Therefore, microphysics (e.g. pressure) is important. Expanding the density field $\rho(\mathbf{x}, t)$ linearly in a small parameter $\delta(\mathbf{x}, t)$,

$$\rho(\mathbf{x}, t) = \rho_0(t)(1 + \delta(\mathbf{x}, t)) \,, \tag{3.30}$$

defines the density contrast $\delta(\mathbf{x})$. Using the fundamental classical equations for fluid motion (Euler, continuity and Poisson equation), expanding all fields – the density, velocity and the gravitational potential – linearly, Fourier transforming everything and doing some algebra, one obtains a second order ordinary differential equation for the amplitude of $\delta$,

$$\ddot{\delta}(\mathbf{k}) + 2\frac{\dot{a}}{a}\dot{\delta}(\mathbf{k}) + \left( \frac{v_s^2 |\mathbf{k}|^2}{a^2} - 4\,\pi G \rho_0 \right) \delta(\mathbf{k}) \;=\; 0 \,, \tag{3.31}$$

where $\delta(\mathbf{k})$ is an abbreviation for the Fourier transform of $\delta(\mathbf{x})$ and $v_s = (\partial p/\partial \rho)^{1/2}$ is the speed of sound, which evolves with time. This equation describes the gravitational amplification of density perturbations, where gravity tends to enhance the density contrast and pressure to restore. There is a critical wavenumber, corresponding to a critical wavelength $\lambda \equiv 2\pi a/|\mathbf{k}|$, known as the Jeans wavelength

$$\lambda_J \;=\; v_s \sqrt{\frac{\pi}{G\rho_0}} \,, \tag{3.32}$$

for which the gravity-pressure term becomes zero. If

1. $k < k_J$, there will be a solution where the fluctuations can grow. This growth depends on the Hubble rate. It would be exponential for a static universe, while for a matter dominated universe it behaves like a power law.

2. $k > k_J$, the solution corresponds to that of a damped harmonic oscillator with damping rate $H = \dot{a}/a$.

The above equation (3.31) is only applicable for linear perturbation theory in a Newtonian treatment, i.e. for subhorizon modes and if no relativistic effects have to be taken into account.

In the real-world case, we need to consider relativistic effects and four components instead of one: Cold Dark Matter (CDM), baryons, photons and neutrinos. Neutrinos and photons are described by their momentum distribution functions, and their time evolution is given by the Boltzmann equation. CDM and baryons are described as well by the Boltzmann equation, but the fluid description (3.31) must be incorporated. Neutrinos and CDM are collisionless, interacting only gravitational, while baryons and photons interact with each other. Thus, before recombination, they are described as a single tightly coupled fluid, where the photons provide the pressure and the baryons the inertia.

The corresponding derivations and equations are omitted here. Instead, we present the results in short:

For subhorizon modes in the matter dominated era, the perturbations can grow or oscillate as given in 1. and 2.. For radiation, curvature and cosmological constant domination, the growth is inhibited - the expansion is too fast.

On superhorizon scales, no causal connection exists, therefore superhorizon density perturbations can grow, even in a radiation dominated universe. Superhorizon modes do not grow, if they are isothermal, whereas their adiabatic counterparts do. In the present-day cosmological models adiabatic perturbations are assumed, because they are the only ones which fit the data.

Two other length scales must be taken into account, the collisionless damping scale and the collisional damping scale. Collisionless particles can stream out of overdense regions into underdense regions, in the process smoothing out inhomogeneities below the free streaming scale $\lambda_{FS}$. The collisional damping scale is called Silk damping scale and is described in the CMB treatment of Sec. 3.1.5.

Once the density contrast becomes large, $\delta \gtrsim 1$, linear perturbation theory (Eq. 3.31) fails, the density perturbation separates from the general expansion ($\lambda_{phys} \propto a$), and remains constant in physical size – structure formation begins.

Putting the pieces together, we give a short overview for the evolution in time of the growth of density perturbations: Before recombination, the Jeans length is enormous, due to the sound speed being of the order of the speed of light. Thus, perturbations which have entered the horizon do not grow much early on, logarithmically at best.

As the universe becomes matter dominated around $z \approx 10^4$, the perturbations in the dark matter component begin to grow. The baryons fall into the CDM potential wells, the baryon-photon fluid gets compressed, photonic pressure resists and at some point stops the collapse which bounces back before recollapsing again. At $z \approx 10^3$, recombination causes the Jeans length to drop drastically, down to a comoving size smaller than present-day galaxies, and perturbations in the baryons begin to grow as well. In comparison to CDM, baryons form much denser objects in the process of structure formation, since they can dissipate away their energy to the photons.

### 3.1.5 The Cosmic Microwave Background

When the temperature of the expanding universe dropped below 3000 K, at $T \simeq 0.5$ eV or at redshift $z \simeq 1100$, the photon energy became too small to ionize hydrogen. The electrons combined with the protons and helium nuclei to form neutral atoms. We refer to this time as the epoch of recombination. The universe became transparent within a narrow redshift range of $z \sim 200$. Then the photons propagated freely losing energy almost merely due to redshift with some small perturbations on their way to us. We therefore observe a thin shell of photons, the surface of last scattering – with finite thickness and plus some small processing that occurred en route to us. This surface is a snapshot in the sky of the universe at the time of recombination.

This cosmic background radiation (CBR) is the most perfect blackbody ever seen with a temperature of $T_\gamma = 2.725$ K. Observations show that there are departures from perfect isotropy at the $10^{-5}$ level, seen as temperature differences over a wide range of angular scale. These anisotropies of the Cosmic Microwave Background (CMB) sky are usually expressed by using spherical harmonic expansion,

$$\frac{\Delta T(\theta, \phi)}{T} = \sum_{lm} a_{lm} Y_{lm}(\theta, \phi) \,. \tag{3.33}$$

The temperature fluctuations are related to the density perturbations in the photons at recombination by $\Delta T/T \propto \Delta \rho_\gamma / \rho_\gamma$. The basic picture of the origin of primary fluctuations before recombination was described in the last section. In addition, there are effects which arise due to effects during recombination, mainly due to Silk damping, and after recombination the effects are due to curvature and projection.

We distinguish primary fluctuations - these are the ones which carry the characteristical imprints from time around recombination - from secondary ones (the ones generated along the line of sight), where then tertiary are the foregrounds.

There are three basic primary effects:

i.) Gravitational (Sachs-Wolfe) perturbations. Photons from high density regions at last scattering have to climb out of potential wells and are thus redshifted (cooler).

ii) Intrinsic or adiabatic perturbations. In high density regions, the coupling of matter and radiation can compress the radiation as well, giving a higher temperature. A
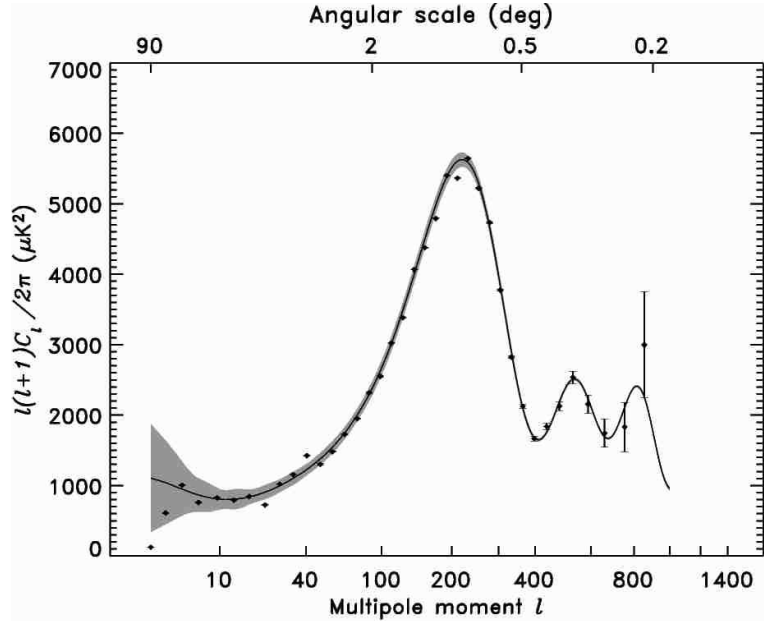
Figure 3.1: Angular power spectrum of the cosmic microwave background. Solid line: best fit ΛCDM from Spergel, gray band: $1\sigma$ error due to cosmic variance on the cut sky. From Ref. [24].

denser spot recombines later. It is therefore less redshifted and appears hotter.

iii) Velocity or Doppler perturbations. The plasma has a non-zero velocity at recombination which leads to Doppler shifts in frequency and hence in brightness temperature.

The secondary fluctuations can be shortly summarized as gravity induced (mainly integrated Sachs-Wolfe effect and lensing) and those due to reionization.

The integrated Sachs-Wolfe effect (ISW) arises when gravitational potentials are evolving with time. The depth of a potential well has increased, while a photon propagates through it. Therefore it gains a net redshift and appears cooler. In a matter-dominated universe, gravitational potentials remain constant. In models with significantly less than the critical density in matter (as so called ΛCDM model), the gravitational potentials are still evolving at recombination. The same is the case at late times, when the universe makes a transition from matter domination to either vacuum energy domination or a significantly curved space time metric, giving an integrated Sachs-Wolfe contribution.

Now, we are able to understand the CMB anisotropy spectrum, as shown in Fig. 3.1. The description of the physics underlying the power spectrum can be separated into three main regions, characterized by the multipole $l$:

23

The horizon scale at last scattering corresponds to $l \lesssim 100$. Anisotropies larger than that have not evolved significantly, therefore giving hints about the initial conditions. Assuming a nearly scale invariant-spectrum at early times, the plateau in the angular power spectrum is flat. Time variation in the potentials leads to a rise in the spectrum at lowest $l$s due to the ISW effect.

On sub-degree scales, $100 \lesssim l \lesssim 1000$, the rich structure in the anisotropy spectrum is the consequence of the gravity-driven acoustic oscillations before recombination. The perturbations inside the horizon at last scattering have been able to evolve causally and produce anisotropy at the last scattering epoch which reflects that evolution. The frozen-in phases of these sound waves imprint a dependence on the cosmological parameters, which gives CMB anisotropies their great constraining power. At the point of recombination, the acoustic oscillations were frozen in and projected on the sky as a harmonic series of peaks. The main peak is the mode that went through 1/4 of a period, reaching maximal compression, and therefore a temperature higher than the average. The even peaks are maximal underdensities, which are generally of smaller amplitude, since the rebound has to fight against the baryon inertia[4]. The troughs, which do not extend to zero power, are partially filled by the Doppler effect because they are at the velocity maxima.

An additional effect comes from projection. The scale associated with the peaks is the sound horizon at last scattering, which can be calculated as a physical length scale. This scale is projected at the sky, leading to an angular scale which depends on the background cosmology. Hence the angular positions of the peaks are a sensitive probe of the spatial curvature of the universe ($\Omega_{\text{tot}}$). For an open universe, the peaks are lying at larger $l$s and for a closed universe at smaller $l$s.

On even shorter scales, $l \gtrsim 1000$, the finite duration of the recombination has an observable effect. During this time, the photons can still interact with the baryons and random walk a distance. If the photon mean free path is larger than the wavelength of a given mode, but the photons did not decouple altogether, this mode will get suppressed. This effect is called photon diffusion or Silk damping.

### 3.1.6 Large Scale Structure

The matter power spectrum $P(k, \tau)$ can be decomposed into a primordial part $P_{init}(k)$, given by the "initial conditions", and the transfer function $T(k, \tau)$, which reflects the time evolution given by the assumed cosmological model,

$$P(k, \tau) \;=\; P_{init}(k) \, T^2(k, \tau), \tag{3.34}$$

where $k$ is the wavenumber and $\tau$ is the conformal time. Due to the lack of any preferred length scale in absence of a physical theory, the primordial power spectrum

---

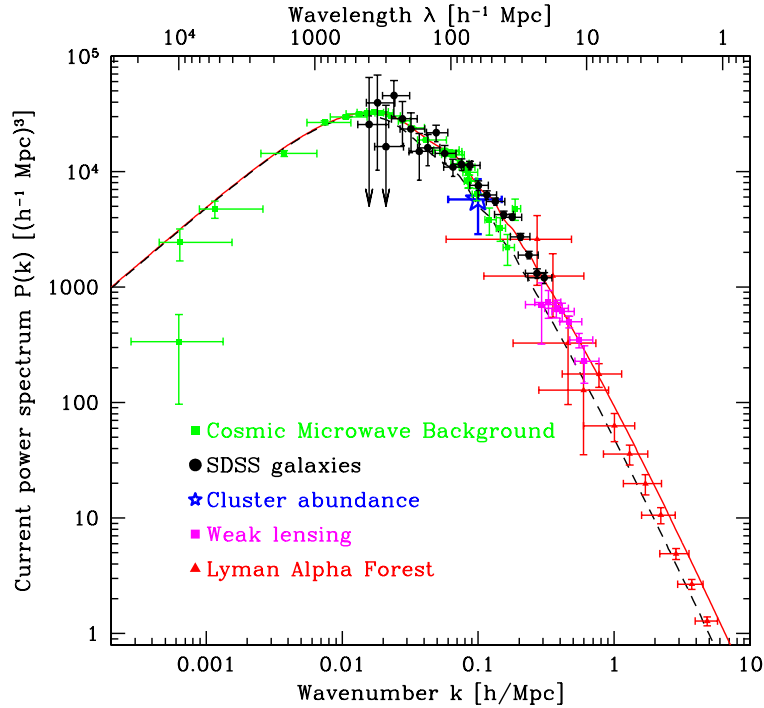[4]Note, that the power spectrum is the amplitude squared.

Figure 3.2: Cosmological constraints for the current matter power spectrum, with the parameters $\Omega_M = 0.28$, $h = 0.72$, $\Omega_B/\Omega_M = 0.16$ (solid line) and as before but with 7% of CDM replaced by neutrinos, corresponding to $\sum m_\nu = 1$ eV (dashed line). From Ref. [25].

is assumed to follow a featureless power law

$$P_{init}(k) \propto k^n \,. \tag{3.35}$$

The power spectrum of today, $P(k) \equiv P(k, \tau = \tau_0)$, is defined as the Fourier transform of the two-point correlation function of the density perturbations,

$$P(k) = \langle |\delta(k)|^2 \rangle \,. \tag{3.36}$$

What is observed with large-scale structure surveys is the power spectrum of the galaxies. Unfortunately, the power spectrum of the visible matter (galaxies) traces not exactly the power spectrum of all matter

$$P_{gal}(k) = b(k)^2 P_m(k) \,. \tag{3.37}$$

The bias parameter $b(k)$ is usually assumed to be a slow function of the wavenumber $k$ or, even a scale independent parameter $b$.

In a radiation dominated universe, density perturbations are frozen in as soon as they enter the horizon, whereas the (adiabatic) superhorizon scaled perturbations grow. If the perturbations enter the horizon in a matter dominated time, they continue rising as they did before. The small scales, which enter the horizon first, cannot grow in amplitude until matter-radiation equality. If we start with a featureless power law for the power spectrum, the small scales, which enter the horizon before matter-radiation equality $t_{EQ}$, are decreased in amplitude in comparison to the large ones. Thus, the turning point in the matter power spectrum is directly related to the size of the horizon at matter-radiation equality, see Fig. 3.2.

### 3.1.7 The Cosmic Neutrino Background

About one second after the Big Bang, neutrinos decouple from the primeval plasma – their interactions freeze out. Being undisturbed since that moment, the present-day parameters of the cosmic neutrino background are entirely determined by the very early universe history. Only very late, neutrinos might cluster, if they are heavy enough.

**A Brief Thermal Neutrino History**

In the following, we derive the present day C$\nu$B properties in the case of instantaneous decoupling, no later distortion of the momentum distributions and a vanishing chemical potential. This so inferred standard scenario is assumed throughout this work, if not otherwise stated.

To derive the neutrino decoupling temperature, we compare the interaction rate with the expansion rate. By solving the Boltzmann equation and assuming the neutrinos to be in complete scattering equilibrium, one gets the neutrino interaction rate

$$\Gamma_\nu = \frac{16\,G_F^2}{\pi^3}\,T^5(s_w^4 + (\pm 1/2 + s_w^2)^2)\,, \tag{3.38}$$

where difference of the upper sign $(\nu_e)$ to the lower sign $(\nu_{\mu,\tau})$ is due to the fact that electrons and positrons still belong to the equilibrium plasma. The early universe expansion rate is given by

$$H = 1.66\,g_*^{1/2}\,\frac{T^2}{M_{Pl}}\,. \tag{3.39}$$

Using the criterion $H = \Gamma|_{T=T_D}$, we find the neutrino temperatures of decoupling from the primeval plasma $T_D(\nu_e) \simeq 2.4$ MeV and $T_D(\nu_{\mu,\tau}) \simeq 3.7$ MeV, assuming $g_* = 10.75$ as it is the case in the Standard Model.

At the time the neutrinos decoupled, they were highly relativistic. If a neutrino had the momentum $p_D$ at decoupling, it would have the redshifted momentum $p(t) =$

$p_D \, a_D / a(t)$ at a later time $t$, where $a$ is the scale parameter. Thus, the original Fermi-Dirac momentum distribution function pertains its original relativistic form, even if the neutrinos are non-relativistic today, but it is characterized by an effective temperature $T = T_D \, a_D / a$.

After neutrino decoupling, photons and neutrinos still share a common temperature, until the temperature drops below $T \sim m_e / 3$. Then the $e^+ e^-$ pairs annihilate, transferring their entropy to the photon gas, while the neutrino temperature is unaffected. Since the entropy $S = (2\pi^2 / 45) \, g_{*S} \, T^3 \, a^3$, see Eq. (3.26), in a comoving volume of a given species in thermal equilibrium is conserved, we obtain the ratio of neutrino to photon temperature simply by counting the degrees of freedom. Before the $e^+ e^-$ pairs annihilate, the particles in equilibrium are $e^+$, $e^-$ and $\gamma$ and thus $g_{*S}^{\mathrm{eq}} = 11/2$, where $g_{*S}^{\mathrm{eq}}$ denotes the relativistic degrees of freedom in equilibrium. After $e^+ e^-$ annihilation only the photons survive, therefore $g_{*S}^{\mathrm{eq}} = 2$. Since the neutrino temperature scales with $a^{-1}$, by setting $S_{before} = S_{after}$ before and after annihilation, we get for the ratio of the neutrino to photon temperature,

$$\frac{T_\nu}{T_\gamma} \;=\; \left( \frac{4}{11} \right)^{1/3} , \tag{3.40}$$

which remains constant as the universe expands.

Now we are able to derive all neutrino parameters as they are inferred by standard big bang theory. The CMB temperature, which is measured to high accuracy to be $T_{\gamma 0} = 2.725$ K today, allows us to derive the present-day neutrino temperature from Eq. (3.40),

$$T_{\nu 0} \;\simeq\; 1.945 \text{ K} . \tag{3.41}$$

Furthermore, the present-day[5] averaged number density per species, momentum and root mean squared momentum derive as

$$\langle \, n_{\nu 0} \, \rangle \;=\; \frac{3}{22} \, \langle \, n_{\gamma 0} \, \rangle \simeq 56 \text{ cm}^{-3} \tag{3.42}$$

$$\langle \, |\vec{p}_{\nu 0}| \, \rangle \;=\; \frac{7}{2} \frac{\zeta(4)}{\zeta(3)} \left( \frac{4}{11} \right)^{1/3} T_{\gamma 0} \simeq 5.314 \times 10^{-4} \text{ eV} \tag{3.43}$$

$$\langle \, \vec{p}_{\nu 0}^2 \, \rangle^{1/2} \;=\; \left( 15 \frac{\zeta(5)}{\zeta(3)} \right)^{1/2} \left( \frac{4}{11} \right)^{1/3} T_{\gamma 0} \simeq 6.044 \times 10^{-3} \text{ eV} , \tag{3.44}$$

where the neutrino number density scales with redshift $z$ as $\langle \, n_\nu(z) \, \rangle = \langle \, n_{\nu 0} \, \rangle (1 + z)^3$ and the momentum as $\langle \, |\vec{p}_\nu(z)| \, \rangle = \langle \, |\vec{p}_{\nu 0}| \, \rangle (1 + z)$.

---

[5]Note, that throughout this work, we denote present-day parameters with subscript zero.

**Neutrino Clustering**

If neutrinos are heavy enough, such that their velocities become less than the escape velocity of a massive object, the relic neutrinos fall into the potential wells of the latter – and are clustered today. For instance, the neutrinos of our local neighborhood could cluster to the halo of the Milky Way. As a general result, their original Fermi-Dirac distribution is distorted. In particular, their average velocities, the frame, in which their velocities are isotropic and their number density may be locally modified. Neutrino clustering has been extensively studied in Ref. [26], some of their results are shown in Tab. 3.1.

| | $n_\nu / \langle n_\nu \rangle$ | $\langle |\vec{p}_\nu| \rangle$ [eV] | $\langle |\beta_\nu| \rangle$ |
|---|---|---|---|
| **clustered $\nu$'s** | | | |
| $m_\nu = 0.6$ eV | 20 | $8.5 \times 10^{-4}$ | $1.4 \times 10^{-3}$ |
| $m_\nu = 0.45$ eV | 10 | $6.7 \times 10^{-4}$ | $1.5 \times 10^{-3}$ |
| $m_\nu = 0.3$ eV | 4 | $5.4 \times 10^{-4}$ | $1.8 \times 10^{-3}$ |
| $m_\nu = 0.15$ eV | 1.6 | $4.9 \times 10^{-4}$ | $3.2 \times 10^{-3}$ |
| **unclustered $\nu$'s** | | | |
| $m_\nu = 0.1$ eV | 1 | $5 \times 10^{-4}$ | 0.06 |
| $m_\nu = 0.01$ eV | 1 | $5 \times 10^{-4}$ | 0.5 |
| $m_\nu = 0.001$ eV | 1 | $5 \times 10^{-4}$ | 0.987 |
| $m_\nu = 0.0001$ eV | 1 | $5 \times 10^{-4}$ | 0.9999 |

Table 3.1: Relic neutrino parameters on Earth: Overdensity, averaged momentum and averaged velocity for different neutrino masses. If $m_\nu \geq 0.15$ eV, clustering becomes significant. The kinematical parameters $\langle |\vec{p}_\nu| \rangle$ and $\langle |\beta_\nu| \rangle$ are evaluated in the rest frame of the C$\nu$B. The values in the clustered case are taken from [26].

## 3.2 C$\nu$B Parameters from Cosmological Probes

The impact of neutrinos to the universes evolutionary history is briefly outlined, and the current constraints from cosmological probes on neutrino parameters are presented.

### 3.2.1 The Absolute Scale of the Neutrino Mass

The cosmic neutrino number density per flavor is $n_{\nu\bar{\nu}} = 112$ cm$^{-3}$ assuming negligible asymmetry. If neutrinos have masses and are nonrelativistic today, we find for the

cosmic mass fraction

$$\Omega_\nu \, h^2 \;=\; \sum_\nu^{N_\nu} m_\nu \, / \, 92.5 \text{ eV} \,, \tag{3.45}$$

where $N_\nu$ is the number of neutrino species and $h$ is the Hubble constant in units of $100$ km s$^{-1}$ Mpc$^{-1}$. From the requirement that neutrinos do not overclose the universe, $\Omega_\nu \leq 1$, one gets the traditional so-called Gershtein-Zeldovich limit [27] $m_\nu \lesssim 46$ eV$/N_\nu$.

Neutrinos as the main source of dark matter are experimentally excluded. Firstly by the Tremaine-Gunn bound [28], which by phase space arguments estimates the lower bound of the neutrino mass $\sim 25$ eV for making up all dark matter in the Milky Way. This is excluded by current mass limits of e.g. tritium beta decay, $m_\nu < 2.2$ eV. Secondly, the now established small masses of the neutrinos imply that they stay relativistic for a long time after their decoupling, allowing them to stream freely, erasing density fluctuations on small scales. If neutrinos make up all dark matter, this implies a top-down scenario of structure formation, where large scales form first, fragmenting into smaller ones. This neutrino dark matter prediction is in contradiction with observation.

In general, neutrinos tend to free-stream out of potential wells, erasing density perturbations. Free streaming is efficient on scales below the Jeans length.
In the neutrino mass range of $10^{-3}$ eV to $0.3$ eV, the transition to the non-relativistic regime takes place at the time of structure formation, and the matter power spectrum is directly affected in a mass-dependent way. On scales smaller than the present-day free streaming wavelength the damping is maximal, corresponding to the wavenumbers

$$k > k_{\text{FS}} = 0.63 \left( \frac{m_\nu}{1 \text{ eV}} \right) h \, \text{Mpc} \,. \tag{3.46}$$

On the largest scales, those which are always larger than the Jeans length, neutrinos cluster just like CDM, therefore, these scales are not affected by free streaming. Finally, there is a range of intermediate wavelengths which become smaller than the Jeans wavelength and then encompass it again – these scales interpolate between the two regimes. The net effect on the power spectrum is a damping of all wavelengths smaller than the horizon scale at the time of the transition of neutrinos to a non-relativistic regime [29]

$$k > k_{\text{nr}} = 0.026 \left( \frac{m_\nu \Omega_M}{1 \text{ eV}} \right)^{1/2} h \, \text{Mpc} \,, \tag{3.47}$$

with a suppression factor

$$\frac{\Delta P(k)}{P(k)} \simeq -8\frac{\Omega_\nu}{\Omega_M} \, . \tag{3.48}$$

At scales smaller than the free streaming scale, the neutrino fluctuations are washed out completely, therefore the relative suppression of power is proportional to the ratio of neutrino energy density to the overall matter density.

Thus, the shape of the power spectrum is influenced by neutrinos in a characteristical way.

Neutrinos of sub-eV mass are relativistic (or semi-relativistic) at the time of recombination $T_{rec} \sim 0.3$ eV. The enhanced ratio of radiation to matter at the time of recombination affects the CMB mainly due to an enhanced early ISW effect. Since this is a subdominant effect, it is very difficult to constrain the neutrino mass with CMB data.

On the other hand, LSS data alone can not constrain the neutrino mass, because of degeneracies with other parameters. But combining data from CMB and LSS, the bound gets very stringent:

$$\sum m_\nu \lesssim 1.8 \text{ eV} \qquad \text{using WMAP + SDSS [30]}$$

$$\sum m_\nu \lesssim 1.2 \text{ eV} \qquad \text{using WMAP + other CMB + 2dF + H}_0 \text{ [13]}$$

$$\sum m_\nu \lesssim 0.6 \text{ eV} \qquad \text{using WMAP + other CMB + 2dF + SDSS + H}_0 \text{ [31]} \, .$$

### 3.2.2 The Effective Number of Neutrino Species

The energy density of relativistic particles in the universe is usually assumed to be given by that of the electrons, the positrons, the photons and three thermally decoupled neutrinos before $e^+e^-$ annihilation occurs (pre), and after by that of the photons and neutrinos solely (post). These contributions fix the evolution of the universe in the radiation dominated epoch. For BBN considerations the pre-annihilation contributions are relevant, while for CMB and structure formation the post-annihilation contributions are important. Thus, in the presence of sterile neutrinos, the total energy density of the universe during the radiation dominated epoch would be significantly affected and change the expansion rate $H_{\mathrm{RD}} = (8\pi G \rho_R/3)^{1/2}$. Although a nonstandard expansion rate could be due to different reasons, e.g. a change in the strength in gravity, all effects are parameterized by a single quantity – the effective

number of neutrino species, $N_{\text{eff}}$, defined by the relation

$$\rho_R = \left(11 + \frac{7}{8} N_{\text{eff}}\right) \frac{\pi^2}{15} T_\gamma^4 \qquad \text{pre} \qquad (3.49)$$

$$= \left(1 + \frac{7}{8} \left(\frac{4}{11}\right)^{4/3} N_{\text{eff}}\right) \frac{\pi^2}{15} T_\gamma^4 \quad \text{post}. \qquad (3.50)$$

Here, $\rho_R$ stands for the total energy density of relativistic particles and $\rho_\gamma = \pi^2/15\, T_\gamma^4$ is the contribution of photons.

The value of $N_{\text{eff}}$ is constrained by BBN from the comparison of theoretical predictions with the measured primordial $^4$He abundances[6]. For $N_{\text{eff}}$ larger than than the standard value, the expansion rate is increased, leading to an increased neutron-to-proton freeze out ratio $(n/p)_f$. Thus the primordial $^4$He abundance must be larger than in the standard scenario.

For $N_{\text{eff}}$ larger than standard, the time of matter radiation equality $(t_{\text{EQ}})$ is delayed, and occurs closer to the epoch of recombination. Furthermore, the universe is younger at recombination, therefore the sound horizon at recombination is smaller. The resulting main effect on the CMB anisotropy spectrum is a more pronounced peak structure and a shift in the positions of the peaks towards larger $l$s – see e.g. [32]. The delayed matter-radiation equality impacts on the matter power spectrum, because a shorter matter-dominated stage implies less growth for perturbations inside the Hubble radius. As a consequence, the maximum of the matter power spectrum will be shifted to lower wavenumbers $k$.

Recent BBN analyses give the bound

$$2.67 \lesssim N_{\text{eff}} \lesssim 3.85 \qquad (3.51)$$

at 68% C.L.[17]. Combined analyses of CMB and LSS data [33] find the allowed range $0.9 \le N_{\text{eff}} \le 7.0$, whereas including BBN data in addition tightens the bound to $2.3 \le N_{\text{eff}} \le 3.0$ [33].

### 3.2.3 Neutrino Asymmetry

It is usually assumed that the cosmological lepton asymmetry is vanishingly small. The baryon asymmetry is $\eta \simeq 6 \times 10^{-10}$ [34] and the electric charge asymmetry is probably zero. Thus, by analogy, the asymmetry between leptons and antileptons is also assumed to be small. Moreover, there are theoretical reasons for this – for $SU(5)$

---

[6]The existing degeneracy of the parameters $N_{\text{eff}}$ and the baryon-to-photon ratio $\eta = (n_B - n_{\bar{B}})/n_\gamma$ in the $^4$He abundance can be removed by using measurements of primordial deuterium or CMB measurements to infer $\eta$.

grand unification models, the difference between baryonic and leptonic charges $(B-L)$ is conserved, therefore, baryon and lepton asymmetry must be of the same order – and similarly in simple models of $SO(10)$. Nevertheless, a nonzero neutrino degeneracy parameter is no established fact.

For a nonzero neutrino chemical potential $\mu_\nu$ or a nonzero degeneracy parameter $\xi_\nu = \mu_\nu/T$, the latter being invariant under cosmic expansion, the number density and energy density of relativistic neutrinos plus antineutrinos of one flavor are

$$n_{\nu\bar{\nu}} = T_\nu^3 \frac{3\zeta(3)}{2\pi^2} \left( 1 + \frac{2\ln(2)\xi_\nu^2}{3\zeta(3)} + \frac{\xi_\nu^4}{72\zeta(3)} + \mathcal{O}(\xi_\nu^6) \right) \tag{3.52}$$

$$\rho_{\nu\bar{\nu}} = T_\nu^4 \frac{7\pi^2}{120} \left( 1 + \frac{30}{7} \left( \frac{\xi_\nu}{\pi} \right)^2 + \frac{15}{7} \left( \frac{\xi_\nu}{\pi} \right)^4 \right) . \tag{3.53}$$

Thus, a nonzero chemical potential results in an increase of the energy density of neutrinos – considering this, the same arguments as above for $N_{\text{eff}}$ apply.

In addition, an electron neutrino chemical potential modifies the neutron to proton ratio $n/p \propto \exp(-\xi_{\nu_e})$. Depending on the sign of $\xi_{\nu_e}$, this effect can increase or decrease the helium abundance and can compensate for the effect of the other flavors. Including compensation effects and restricting the radiation density from other probes, we get [35]

$$-0.01 \lesssim \xi_{\nu_e} \lesssim 0.22 \qquad , \qquad |\xi_{\nu_{\mu,\tau}}| \lesssim 2.6 \, . \tag{3.54}$$

However, since neutrinos are almost maximally mixed, oscillations imply that the individual lepton numbers are not conserved. If flavor equilibrium is achieved before $n/p$ freeze out, then the restrictive BBN limit for electron neutrinos applies to all flavors [36, 37, 38].

# Part II

# Neutrino-Nucleon Scattering

In this part, we analyze the possibilities of relic neutrino detection via neutrino-nucleon and neutrino-nucleus scattering. In the first chapter we study the force on a torsion balance induced by the C$\nu$B flux [39, 40, 41, 42, 43, 44, 45, 48, 49]. In the second chapter, we explore the chance of inverse beta decay processes to be observable at hadron colliders.

In general, the center of mass energies relevant for these processes are lowered tremendously by the small momentum and the small mass of the neutrinos, resulting in a small cross section. On the other hand, a large enhancement in the cross section from coherent interactions is expected, since the reduced de Broglie wavelength $\lambdabar$ of a big bang neutrino with momentum $|\vec{p}_{\nu 0}| = 5 \times 10^{-4}\,\text{eV}$

$$\lambdabar_{\nu 0} = \frac{1}{|\vec{p}_{\nu 0}|} \simeq 0.4 \text{ mm} \tag{3.55}$$

is macroscopic.

# Chapter 4

# Torsion Balance

Due to the peculiar motion of the solar system with respect to the C$\nu$B, the Earth gets permanently penetrated by a flux of relic neutrinos. With regard to a measurement of this C$\nu$B flux, some neutrino optical approaches – total reflection, refraction, angular momentum transfer to an anisotropic medium – have been considered [39, 46, 47] to give a linear effect in $G_F$, but they have been proven to vanish [40, 41], except for the so called Stodolsky effect [39]. This effect arises due to the energy split of two electron spin states in the cosmic neutrino bath, and is proportional to $n_\nu - n_{\bar{\nu}}$. Therefore, it can only occur for a non-vanishing neutrino asymmetry and polarized targets[1]. The Stodolsky effect can only be measured for an appropriately large neutrino asymmetry. For $\xi \simeq 2.5$, the acceleration of a torque could be $a_{G_F} \sim 10^{-27}$ cm$^2$/s for reasonable parameter choices [49]. Due to experimental restrictions on the neutrino asymmetry, we do not consider this effect further.

In the following, we instead explore the momentum transferred on an (unpolarized) target by elastic scattering of the relic neutrino flux, and discuss the possibility of measuring the resulting force on a torsion balance.

## 4.1   Kinematics and Cross Section

If neutrinos are unclustered, the averaged momentum $\langle \vec{p}_\nu \rangle$ vanishes[2] in the CBR rest frame, where the neutrino flux is isotropic. In the target rest frame moving with the velocity $\vec{\beta}_*$ with respect to the CBR, the averaged four-momentum reads

$$\langle p'_\nu \rangle = \begin{pmatrix} \gamma_* \langle E_\nu \rangle \\ \gamma_* \vec{\beta}_* \langle E_\nu \rangle \end{pmatrix} , \tag{4.1}$$

with $\gamma_* = (1 - \beta_*^2)^{-1/2}$ and $\langle E_\nu \rangle$ being the averaged energy of a relic neutrino in the CBR rest frame. The target velocity with respect to the CBR is given by the

---

[1]The Stodolsky effect also vanishes for clustered Majorana neutrinos.
[2]Note, that $|\langle \vec{p} \rangle| \neq \langle |\vec{p}| \rangle$.

peculiar motion of the solar system $\beta_* = 1.2 \times 10^{-3}$ ($v_* = 368$ km/s). Since this is a nonrelativistic velocity, $\gamma_* \simeq 1$ and thus $\langle \vec{p}_\nu' \rangle \simeq \vec{\beta}_* \langle E_\nu \rangle$ for the averaged momentum in the target frame holds.

The average norm of the momentum in the target rest frame $\langle |\vec{p}_\nu'| \rangle$ and thus the corresponding reduced wavelength $\lambdabar_\nu'$ remain unchanged compared to the respective quantities $p_\nu \equiv \langle |\vec{p}_\nu| \rangle$ and $\lambdabar_\nu$ in the CBR frame.

If neutrinos are heavy enough, $m_\nu \gtrsim 0.1$ eV, they are clustered today. As a result, the frame, in which the neutrino flux is isotropic and the neutrino momenta within this frame are modified. The neutrinos of our local neighborhood are assumed to cluster to the halo of the Milky Way. The corresponding overdensities at Earth, averaged momenta $\langle |\vec{p}_\nu| \rangle$ and velocities $\beta_\nu$ within this frame are given in Tab. 3.1. The velocity of the solar system with respect to the halo of the Milky Way is $\beta_* = 7.7 \times 10^{-4}$ ($v_* = 230$ km/s). Therefore, $\beta_* \simeq 10^{-3}$ holds for both cases, clustered and unclustered, but the values of $\langle |\vec{p}_\nu| \rangle$ and $\beta_\nu$ can differ, in which amount is dependent on the neutrino mass.

In the non-relativistic case, the discrimination between Majorana and Dirac neutrinos becomes important. We start by assuming the neutrinos to be Dirac species, and include a correction factor later to the calculations.

We consider the elastic scattering process $\nu_\alpha n \to \nu_\alpha n$, where $\nu_\alpha$ is a neutrino of flavor $\alpha$ and $n$ is a single particle of the target material. The matrixelement of the neutral current interaction is given by

$$
\begin{aligned}
\mathcal{M} &= \frac{G_F}{\sqrt{2}} [\, \bar{u}_{\nu_\alpha}^f \, \gamma^\mu (1 - \gamma_5) \, u_{\nu_\alpha}^i \,][\, \bar{u}_n^f \, \gamma^\mu (g_v - g_a \gamma_5) \, u_n^i \,] \qquad (4.2) \\
&= \frac{G_F}{\sqrt{2}} [\, \bar{u}_{\nu_\alpha}^f \, \gamma^\mu (1 - \gamma_5) \, u_{\nu_\alpha}^i \,] \left( [\, \bar{u}_n^f \, c_L \, \gamma^\mu (1 - \gamma_5) \, u_n^i \,] \right. \\
&\qquad\qquad\qquad \left. + [\, \bar{u}_n^f \, c_R \, \gamma^\mu (1 + \gamma_5) \, u_n^i \,] \right),
\end{aligned}
$$

where $u_{\nu_\alpha}^{i,f}$ ($u_n^{i,f}$) are the initial and final neutrino (target particle) plane wave states, $G_F = 1.166 \times 10^{-5}$ eV is the Fermi coupling constant, $g_v$ and $g_a$ are the vector and axial vector couplings, and $c_L$ and $c_R$ the left- and right-handed couplings, respectively. The target particles are protons, neutrons and electrons. For the electrons, in addition, the charged current process $\nu_e e^- \to \nu_e e^-$ has to be taken into account, which fits after a Fierz transformation in the scheme of Eq. (4.2). The respective couplings are given in Tab. 4.1.

Here we consider an unpolarized target, i.e. a bound system with equally distributed spin states. Within the coherence volume, all interactions add up coherently. Averaging over spins in the initial state and summing over indistinguishable spins in the

|          | $g_v$           | $g_a$  |
|----------|-----------------|--------|
| $e^-$ ($Z^0$)   | $-1/2 + 2\,s_w^2$ | $-1/2$ |
| $e^-$ ($W^\pm$) | $1$             | $1$    |
| $p$      | $1/2 - 2\,s_w^2$ | $1/2$  |
| $n$      | $-1/2$          | $-1/2$ |

Table 4.1: The vector and axialvector couplings of electrons, protons and neutrons. The lefthanded and righthanded couplings are given by $c_L = (g_v + g_a)/2$ and $c_R = (g_v - g_a)/2$ respectively.

final state, leads to an averaged matrixelement

$$\langle \mathcal{M} \rangle \;=\; \frac{G_F}{2\sqrt{2}}\,[\,\bar{u}_\nu^f\,\gamma^\mu(1-\gamma_5)\,u_\nu^i\,][\,\bar{u}_n^f\,(c_L + c_R)\,\gamma^\mu\,u_n^i\,]\,, \tag{4.3}$$

which is sensitive to the vector coupling $g_v = (c_L + c_R)$ solely. Thus we get[3]

$$|\langle \mathcal{M} \rangle|^2 \;\simeq\; 8\,G_F^2\,m_n^2\,m_\nu^2\,\Big(\gamma_\nu^2 + \cos\theta^*\,(\gamma_\nu^2 - 1)\Big)(c_L + c_R)^2\,, \tag{4.4}$$

where $\theta^*$ is the scattering angle in the center of mass system. And $\gamma_\nu$ is the neutrino boost factor in the CBR rest frame, $E_\nu = \gamma_\nu\,m_\nu$. For comparison, the incoherent squared averaged matrixelement is given by

$$\langle\,|\,\mathcal{M}\,|^2\rangle \;\simeq\; 64\,G_F^2\,m_n^2\,m_\nu^2\,\Big(\gamma_\nu^2\,(c_L^2 + c_R^2 - c_L\,c_R) + c_L\,c_R\,\cos\theta^*\,(\gamma_\nu^2 - 1)\Big)\,. \tag{4.5}$$

For the following, we define the coherent intensity factor $I_c = 2\sum(c_L + c_R)$, where the sum for an atom $_Z^A N$ with $Z$ protons and electrons and $A - Z$ neutrons is taken over the coherently contributing individual constituents. With $2\sin\theta_W \approx 1/2$ and the couplings shown in Tab. 4.1, we get

$$
\begin{aligned}
I_{c_1}\,(_Z^A N) &= Z - A & \text{for } \nu_\mu, \nu_\tau &\quad \text{and} \\
I_{c_2}\,(_Z^A N) &= 3Z - A & \text{for } \nu_e\,,
\end{aligned}
\tag{4.6}
$$

where the difference is due to the charged current interactions of the $\nu_e$ with the electrons. The total cross section for a single nucleus $N$ reads as

---

[3]The only simplification used here is $m_n/m_\nu \gg \gamma_\nu$. If relic neutrinos are non-relativistic today, $\gamma_\nu \approx 1$ holds and may be omitted.

$$\sigma_{\nu N}^{\mathrm{coh}} \;=\; \int d\Omega \, \frac{|\mathcal{M}|^2}{64 \, \pi^2 \, s}$$

$$\simeq \; \frac{G_F^2}{8 \, \pi} \, E_\nu^2 \, I_{\mathrm{c}}^2$$

$$\simeq \; 2 \times 10^{-57} \mathrm{cm}^2 \left( \frac{E_\nu}{\mathrm{eV}} \right)^2 I_{\mathrm{c}}^2 \,. \tag{4.7}$$

For $N_N$ nuclei within a volume smaller than the coherence volume $V_{\mathrm{coh}} = 4\pi \, (\lambdabar/2\,)^3/3$ maximal constructive interference can occur, yielding the cross section

$$\sigma_{\nu N}^{\mathrm{coh}}(N_N) \;\simeq\; \frac{G_F^2}{8 \, \pi} \, E_\nu^2 \, N_N^2 \, I_{\mathrm{c}}^2 \,. \tag{4.8}$$

The same cross section applies to anti-neutrinos, where due to the lack of CC interactions with the target, the coherence factor $I_{\mathrm{c}_1}$ is valid for the electron anti-neutrinos. In comparison, the incoherent cross section is given by

$$\sigma_{\nu N}^{\mathrm{ic}}(N_N) \;=\; \frac{G_F^2}{8\pi} \, E_\nu^2 \, N_N \, I_{\mathrm{ic}}^2 \,, \tag{4.9}$$

with the incoherent intensity factor squared normalized as follows $I_{\mathrm{ic}}^2 = 8 \sum (c_L^2 + c_R^2 - c_L c_R) = 2 \sum (g_v^2 + 3g_a^2)$, and therefore given by

$$\begin{aligned}
I_{\mathrm{ic}_1}^2 &= 5Z^2 + 2(A - Z)^2 \qquad \text{for } \nu_e \qquad \text{and} \\
I_{\mathrm{ic}_2}^2 &= 3Z^2 + 2(A - Z)^2 \qquad \text{for } \nu_\mu, \, \nu_\tau \,.
\end{aligned} \tag{4.10}$$

We would like to stress, that the enhancement factor $N_N$ due to coherence can be very large. For $N_{\mathrm{coh}}^\nu$ nuclei filling the whole coherence volume, it amounts to

$$N_{\mathrm{coh}}^\nu \;=\; \frac{\pi}{6} \, \lambdabar_\nu^3 \, \rho_t \, \frac{N_A}{A} \tag{4.11}$$

$$\simeq \; 1.6 \times 10^{17} \left( \frac{\rho_t}{\mathrm{g/cm^3}} \right) \left( \frac{100}{A} \right) \left( \frac{p_\nu}{\langle |\vec{p}_{\nu 0}| \rangle} \right)^3 \,, \tag{4.12}$$

where $\rho_t$ is the mass density of the target material and $N_A$ is the Avogadro number and $\langle |\vec{p}_{\nu 0}| \rangle$ is the thermal momentum of the relic neutrinos
. So far, we have assumed, that the neutrinos are Dirac type. The relic neutrinos being non-relativistic, the discrimination between Dirac and Majorana species is important. If neutrinos are Majorana particles, the cross section is suppressed by a factor $\beta_\nu^2$, which is of order $\sim 10^{-6}$ , see Tab. 3.1.

## 4.2 Force on a Torsion Balance

The net force on the torsion balance is given by

$$F = m_t \, a = \sum_{\nu, \bar{\nu}} \Gamma_{\nu N} \, \langle \Delta \vec{p}_\nu \rangle \,, \tag{4.13}$$

where $a$ is the acceleration, $m_t$ the mass of the target, $\Gamma_{\nu N}$ is the rate of the neutrinos hitting the target and $\langle \Delta \vec{p}_\nu \rangle$ the momentum transferred by a single interacting neutrino. In order to enhance the event rate by exploiting constructive interference, we consider a target, which consists of components of the size $\lambda_\nu$ separated by random distances larger than $\lambda_\nu$. Such a target might be realized by e.g. grains of a high density material inserted in a low density substrate. The event rate is given by[4]

$$\Gamma_{\nu N} \;=\; \frac{N_N}{N^\nu_{\mathrm{coh}}} \, \sigma^{\mathrm{coh}}_{\nu N}(N^\nu_{\mathrm{coh}}) \, \phi_\nu \,. \tag{4.14}$$

The neutrino flux at Earth, i.e. the number of neutrinos per time and area, is given by

$$\phi_\nu = n_\nu \, \beta_\nu \,, \tag{4.15}$$

where $\beta_\nu$ is the velocity of the neutrinos at Earth and $n_\nu$ the corresponding neutrino number density. The corresponding values are given in Tab. 3.1. The acceleration calculates as

$$a \;=\; \frac{G_F^2 \, E_\nu^2}{8\,\pi} \, I_{\mathrm{c}}^2 \, N_N \, \frac{\rho_t}{m_N} \, \underbrace{\frac{4\pi}{3}\left(\frac{\lambda_\nu}{2}\right)^3}_{N^\nu_{\mathrm{coh}}} \sum_{\nu,\bar\nu} \underbrace{n_\nu \beta_\nu}_{\phi_\nu} \; \underbrace{E_\nu \beta_*}_{\langle \Delta \vec{p}_\nu \rangle} \underbrace{/(N_N\, m_N)}_{m_t} \tag{4.16}$$

$$\simeq\; 4 \times 10^{-30} \mathrm{cm/s^2} \left(\frac{\rho_t}{\mathrm{g\,cm^{-3}}}\right) \left(\frac{2\,I_{\mathrm{c}}}{A}\right)^2 \left(\frac{\sum \langle n_\nu \rangle}{336~\mathrm{cm^{-3}}}\right) \left(\frac{n_\nu/\langle n_\nu \rangle}{10}\right) \left(\frac{10^{-3}}{\beta_\nu}\right)^2 ,$$

where $m_N$ is the mass of the nucleus. In the last line we have taken into account a possible local overdensity $n_\nu/\langle n_\nu \rangle$ due to clustering effects[5], see Tab. 3.1.

At present, conventional Cavendish type torsion balances are able to measure accelerations $a \gtrsim 10^{-13}$ cm/s$^2$. According to Ref. [48, 50] an improvement of the sensitivity to $a \sim 10^{-23}$ cm/s$^2$ may be achieved with currently available technology. This is still far above the acceleration occurring in the above described experiment. Further improvements might be expected employing nanotechnology [51] – this is not an option for the next decade but maybe for the next thirty to forty years.

---

[4]The event rate usually is given by $\Gamma_{\nu N} = n_\nu \, n_N \, V \, |\vec\beta_{\mathrm{rel}}| \, \sigma_{\nu N}$. Here, we have used the cross section $N_N/N^\nu_{\mathrm{coh}} \sigma^{\mathrm{coh}}_{\nu N}(N^\nu_{\mathrm{coh}})$, which implies a sum over the scattering centers $N_N = n_N \, V$.

[5]This enhancement could in principle be due to asymmetry as well. The latter is in general expected to be too small to enhance the neutrino number density significantly. However, the formula would also apply in this case.

# Chapter 5

# Inverse Beta Decay at Hadron Colliders

An interesting approach probing the cosmic neutrino background presents the search for a characteristical signature at hadron colliders, in particular at the LHC [52]. The inverse beta decay of a beam nucleus or nucleon induced by the pervasive C$\nu$B,

$$^A_Z N \, \bar{\nu}_l \to \, ^A_{Z-1} N' \, l^+ \qquad \text{or} \qquad p \, \bar{\nu}_l \to n \, l^+ \, , \tag{5.1}$$

$$^A_Z N \, \nu_l \to \, ^A_{Z+1} N' \, l^- \qquad \text{or} \qquad n \, \nu_l \to p \, l^- \, , \tag{5.2}$$

leads to a change in the charge of the beam particle, which therefore exits the beam pipe and becomes accessible for detection. In Eqs. (5.1, 5.2) on the lefthandside the neutrino nucleus process and on the righthandside the neutrino nucleon process is shown. Since hadron colliders are typically able to operate with protons as well as heavy nuclei, e.g. lead (Pb), both processes are considered in the following calculations.

## 5.1 Cross Sections and Transition Probability

The matrixelement of the charged current process $p \, \bar{\nu}_l \to n \, l^+$ is given by

$$\mathcal{M} \;\; = \;\; \frac{G_F}{\sqrt{2}} \, \cos \theta_c \, [\, \bar{u}_{\nu_l} \, \gamma^\mu (1 - \gamma_5) \, u_l \,][\, \bar{u}_n \, \gamma^\mu (g_v - g_a \gamma_5) \, u_p \,] \, , \tag{5.3}$$

where $\theta_c$ is the Cabbibo angle. The corresponding averaged squared matrixelement evaluates as

$$\begin{aligned}
\langle |\mathcal{M}|^2 \rangle \;\; = \;\; & 4 \, G_F^2 \, \cos^2 \theta_c \, \big( (g_v + g_a)^2 (s - (m_p^2 + m_\nu^2))(s - (m_n^2 + m_l^2)) \\
& + (g_v - g_a)^2 (s + t - (m_p^2 + m_l^2))(s + t - (m_n^2 + m_\nu^2)) \\
& + 2 \, (g_v^2 - g_a^2) \, m_p \, m_n (t - (m_l^2 + m_\nu^2)) \big) \, .
\end{aligned} \tag{5.4}$$

The center of mass energy of the considered process is given by $s = 2\,E_p\,m_\nu + m_p^2$, leading to a kinematical threshold of

$$\gamma_p \;\geq\; \frac{\Delta M^2 + m_l^2}{2\,m_p\,m_\nu} + \frac{m_l}{m_\nu}\,, \tag{5.5}$$

where $\gamma_p = E_p/m_p$ is the boost factor of the proton, $\Delta M^2 = m_n^2 - m_p^2 \simeq 2.4 \times 10^{15}$ eV the mass squared differences of neutron and proton and $m_l$ the mass of the charged lepton. The LHC with proton energies of $E_p^{\mathrm{LHC}} = 7$ TeV will not reach this limit.

However, if we consider an appropriate next-to-next-to-next generation collider, i.e. an Ultra Large Hadron Collider (ULHC), with a proton energy of $E_p \geq 2\,\mathrm{PeV}/(m_\nu/\mathrm{eV})$, equivalently to a boost factor of

$$\gamma_p \;\geq\; \frac{2 \times 10^6 \ \mathrm{eV}}{m_\nu}\,, \tag{5.6}$$

the process $p\,\nu_e \to n\,e^+$ would be kinematically reachable. Since the corresponding processes with $l = \mu, \tau$ require much larger proton energies, $E_p > 10^{17}$ eV$/(m_\nu/\mathrm{eV})$, the following discussion is restricted to neutron plus positron production. The squared matrixelement (5.4) in this kinematical region reads

$$\langle |\mathcal{M}|^2 \rangle \;=\; 16\,G_F^2\,\cos^2\theta_c\,E_p^2\,m_\nu^2 \left(1 - \frac{\Delta M^2}{2\,E_p\,m_\nu}\right)\left((g_v^2 + 3\,g_a^2) + (g_v^2 - g_a^2)\cos\theta^*\right) \tag{5.7}$$

and the total cross section in the continuum is given by

$$\begin{aligned}
\sigma_{\nu p}^{\mathrm{CC}} \;&=\; \int d\Omega\,\frac{|\mathcal{M}|^2}{64\,\pi^2\,s} \\
&=\; \frac{G_F^2}{\pi}\,\cos^2\theta_c\,\gamma_p^2\,m_\nu^2 \left(1 - \frac{\Delta M^2}{2\,E_p\,m_\nu}\right)(g_v^2 + 3\,g_a^2) \\
&\simeq\; 10^{-41}\ \mathrm{cm}^2 \left(\frac{\gamma_p}{10^7}\right)^2 \left(\frac{m_\nu}{\mathrm{eV}}\right)^2\,, \tag{5.8}
\end{aligned}$$

where in the last line we have inserted the couplings $g_v = 1$ and $g_a = 1.27$ known from neutron decay. Note that $s \approx m_p^2$, since $\gamma_p \ll m_p/m_\nu \simeq 10^9(\mathrm{eV}/m_\nu)$.

If an ULHC collider is run with lead, both processes (5.1) and (5.2) may take place

$$^{208}_{82}\mathrm{Pb}\ \bar\nu_l \to\ ^{208}_{81}\mathrm{Tl}\ l^+ \qquad \text{and} \qquad ^{208}_{82}\mathrm{Pb}\ \nu_l \to\ ^{208}_{83}\mathrm{Bi}\ l^-\,. \tag{5.9}$$

The kinematical conditions to reach the production threshold are similar as for protons, as Tab. 5.1 shows. To perform the transition from nucleon to nucleus, we first

| | $\frac{\Delta M^2}{A}$ [eV²] | $\gamma_{Pb}$ [$\frac{\text{eV}}{m_\nu}$] |
|---|---|---|
| Pb → Tl | $9 \times 10^{15}$ | $5.5 \times 10^6$ |
| Pb → Bi | $5 \times 10^{15}$ | $3.4 \times 10^6$ |

Table 5.1: Parameters for the inverse beta decay process of lead (Pb): Mass squared differences with the neighbor nuclides Tl and Bi (left row) and the resulting minimal boost factor to reach the production threshold (right row). The atomic mass number is $A = 208$.

check, whether the interaction is coherent over the nucleus. The neutrino momentum in the rest frame of the nucleus is given by

$$|\vec{p}_\nu| \simeq E_\nu = \gamma_{Pb}\, m_\nu \qquad \text{with} \qquad \gamma_{Pb} \simeq \frac{E_{\text{nuc}}}{m_p} \simeq 10^7 \left( \frac{E_{\text{nuc}}}{10\,\text{PeV}} \right), \qquad (5.10)$$

and therefore the coherence length evaluates as

$$\lambda_\nu^{\text{ULHC}} = \frac{1}{|\vec{p}_\nu|} \simeq 2 \times 10^{-14}\,\text{m} \left( \frac{10\,\text{PeV}}{E_{\text{nuc}}} \right) \left( \frac{\text{eV}}{m_\nu} \right), \qquad (5.11)$$

where $E_{\text{nuc}} = E_N/A$ is the energy per nucleon. In comparison, the radius of the nucleus is given by $R_{Pb} \simeq 8 \times 10^{-15}$ m [53]. Thus, coherent interactions must be taken into account within the volume of each nucleus.

Approximating the upper bound for the event rate, we consider maximal constructive interference and neglect nuclear effects by treating the protons and neutrons as free particles. Either the protons (5.1) or the neutrons (5.2) interact coherently, therefore the matrixelement for inverse beta decay of a lead nucleus can be written as

$$\mathcal{M}_{Pb}^{\text{CC}} \simeq \frac{A}{2}\, \mathcal{M}_p,$$

where we have exploited the equality of the couplings and neglected kinematical differences for the neutron-proton and the proton-neutron transition, see Tab. 5.1. In this approximation, the cross section becomes

$$\begin{aligned}
\sigma_{\nu Pb}^{\text{CC}} &= \left( \frac{A}{2} \right)^2 \frac{G_F^2}{\pi}\, \gamma_{Pb}^2\, m_\nu^2 \left( 1 - \frac{\Delta M^2}{2\, E_{Pb}\, m_\nu} \right) (g_v^2 + 3\, g_a^2) \\
&\simeq 10^{-37}\,\text{cm}^2 \left( \frac{A}{208} \right)^2 \left( \frac{\gamma_{Pb}}{10^7} \right)^2 \left( \frac{m_\nu}{\text{eV}} \right)^2,
\end{aligned} \qquad (5.12)$$

evaluated sufficiently far above threshold.

## 5.2 Interaction Rates

The event rate is given by the product of the particle densities $n_\nu$ and $n_N$, the relative velocity $\beta_N$, the interaction volume $V$ and the cross section $\sigma_{\nu N}$,

$$\Gamma = n_\nu \, n_N \, \beta_N \, V \, \sigma_{\nu N} \,. \tag{5.13}$$

Using the electromagnetic current $I$ of the beam and the circumference of the collider $L$, we get the rate for inverse beta decay at the ULHC running with protons

$$\Gamma_p = n_\nu \frac{I}{Z\,e} L \, \sigma_{\nu p}^{\mathrm{CC}} \tag{5.14}$$

$$\simeq 4 \times 10^{-5} \ \mathrm{year}^{-1} \left( \frac{\langle n_{\nu_e} \rangle}{56 \ \mathrm{cm}^{-3}} \right) \left( \frac{I}{0.1 \ \mathrm{A}} \right) \left( \frac{L}{4 \times 10^4 \ \mathrm{km}} \right) \left( \frac{\gamma_p}{10^7} \right)^2 \left( \frac{m_\nu}{\mathrm{eV}} \right)^2,$$

where we have used "reasonable" next-to-next-to-next generation collider parameters as normalization references [54] and a proton energy of $E_p \simeq 10$ PeV. Running this collider with lead at the same energy per nucleon $E_{\mathrm{nuc}} \simeq 10$ PeV, the interaction rate yields

$$\Gamma_{Pb} \simeq 10^{-2} \ \mathrm{year}^{-1} \left( \frac{\sum \langle n_{\nu_e, \bar{\nu}_e} \rangle}{112 \ \mathrm{cm}^{-3}} \right) \left( \frac{I}{0.1 \ \mathrm{A}} \right) \left( \frac{L}{4 \times 10^4 \ \mathrm{km}} \right) \left( \frac{\gamma_{Pb}}{10^7} \right)^2 \left( \frac{m_\nu}{\mathrm{eV}} \right)^2. \tag{5.15}$$

To conclude, the LHC does not provide the energy necessary to reach the production threshold for CνB induced inverse beta decay events. We considered a next-to-next-to-next generation collider with an energy per nucleon $E_{\mathrm{nuc}} \simeq 10^{16}$ eV, a circumference once around the Earth and an electromagnetic current of 0.1 Ampere. We derived an upper limit for the interaction rate of $10^{-2}$ events per year.

# Part III

# Neutrino-Neutrino Scattering

In this part, we examine the possibility to detect the C$\nu$B via neutrino-neutrino scattering. Due to the lack of high density neutrino targets, astrophysical approaches will be employed.

Resonant annihilation of extreme energy cosmic neutrinos (EEC$\nu$'s) with relic anti-neutrinos (or vice versa) into $Z$-bosons leads to sizable emission and absorption effects due to the cross section enhancement near the resonance energies

$$E_i^{\text{res}} = \frac{M_Z^2}{2m_{\nu_i}} = 4.2 \times 10^{21} \text{ eV} \left( \frac{1 \text{ eV}}{m_{\nu_i}} \right), \qquad (5.16)$$

where $M_Z$ is the $Z$ boson mass and $m_{\nu_i}$ are the non-zero neutrino masses ($i = 1, 2, 3$). While emissions of decay particles manifest themselves as ultrahigh energy cosmic protons and photons ($Z$-bursts) [55, 56], the neutrino flux exhibits characteristic absorption dips [57] in this kinematical region. The required energies are far beyond the reach of accelerator beams, but extragalactic sources might provide appropriate neutrino fluxes.

The organization of this part is as follows: The idea of $Z$-bursts and possible extensions to $Z'$-bursts are shown in Chap. 6. Our thorough study of absorption dips is presented in Chap. 7.

# Chapter 6

# The $Z'$ Burst Scenario

In this chapter we explore the possibility of a light $Z'$ to account for the NuTeV anomaly and at the same time to cause the observed highest energy cosmic rays beyond the GZK cutoff.

First we review the GZK problem and the possibility to solve it with bursts of the known $Z$ boson. Neutrino mass ranges and the absolute magnitude of the required extreme energy cosmic neutrino flux are derived. Then we examine the potential of a light $Z'$ to entirely generate the NuTeV anomaly without breaking the experimental bounds. Using the derived limits we analyze the possibility to solve the GZK puzzle with the help of the $Z'$.

## 6.1  The GZK Problem

Due to interactions with the cosmic microwave background (CMB), nucleons with energies above the pion production threshold have a short attenuation length of about $50\,\mathrm{Mpc}$. Thus, for the observed spectrum a sharp drop for energies $E \gtrsim 4 \cdot 10^{19}\,\mathrm{eV}$ is predicted, known as the Greisen-Zatsepin-Kuzmin (GZK) cutoff [58, 59]. Another characteristic feature in the spectrum is a dip at $E \sim 10^{19}$ eV, followed by a bump from the pile-up-effect of the protons.

After correcting nontrivial systematics in the energy calibration, the agreement of the spectral shape calculated for protons with the measured spectra from HiRes [60] and AGASA [61] below the GZK energy is excellent. Above the GZK energy, both experiments detected events, the HiRes data being consistent with the existence of a GZK cutoff, the AGASA being inconsistent with it, see Fig. 6.1.

The conflict of the discrepancy between GZK prediction and the observation presents the unsolved puzzle of the ultra high energetic cosmic rays (UHECRs). The sources, which may explain their origin, are commonly referred to be either bottom-up type, which are astrophysical accelerators, or top-down type, which are topological defects
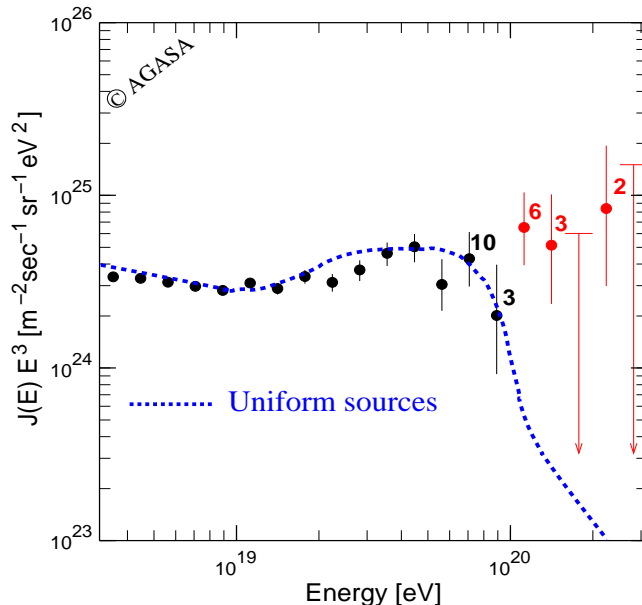
Figure 6.1: The AGASA energy spectrum multiplied by $E^3$ (number of events per energy bin shown for high energies) in comparison with the spectrum for uniformly distributed extragalactic sources (dashed curve); from Ref. [62].

or weakly interacting massive particles, with hadron production in their decay. If Lorentz invariance is not broken – and this we will assume – the sources must be well within the GZK zone of 50 Mpc.

If originating from bottom-up sources within the GZK zone, the direction of the UHECRs should be resolvable and the sources should be well known, which is not the case. Top-down sources may in principle explain the events beyond the GZK cutoff, but not without invoking physics beyond the Standard Model.

## 6.2  Z-Bursts

Extreme energetic cosmic (EEC) neutrinos from extragalactic sources reach red-shifted, but unattenuated the GZK-zone and in annihilation with a relic antineutrino at resonance energy, $E^{\text{res}} = M_Z^2/2m_\nu$, a $Z$-boson is produced. The decay products of the $Z$ are mainly protons (and photons), which are with amazing accuracy in the energy range of the events beyond the GZK cutoff, if a neutrino mass in the eV range is assumed. This is called the $Z$-burst scenario.

In the work of Ref. [63], the UHECR spectrum is modeled under the assumption, that the $Z$-burst scenario is the only source of the events beyond the GZK cutoff. If this is the case, the neutrino mass can be determined from the shape of the spectrum,

and the magnitude of the necessary EEC$\nu$ flux at resonance energy is inferred from the over-all normalization.

The procedure starts with an Ansatz for the differential proton (and photon) flux, i.e. the number of protons arriving at Earth with energy $E$ per units of energy, area, time and solid angle

$$F_{p|Z}(E) = \sum_i \int_0^\infty dE_p \int_0^{R_{max}} dr$$

$$\times \left[ \int_0^\infty dE_{\nu_i} \, F_{\nu_i}(E_{\nu_i}, r) \, n_{\bar{\nu}_i}(r) + \int_0^\infty dE_{\bar{\nu}_i} \, F_{\bar{\nu}_i}(E_{\bar{\nu}_i}, r) \, n_{\nu_i}(r) \right] \qquad (6.1)$$

$$\times \sigma_{\nu_i \bar{\nu}_i}(s) \, \mathrm{Br}(Z \to \mathrm{hadrons}) \frac{dN_{p+n}}{dE_p} (-) \frac{\partial}{\partial E} P_p(r, E_p; E) \,.$$

The photon flux arriving at Earth is obtained accordingly.

In this Ansatz, the quantities related to $Z$-production and decay, i.e. the annihilation cross section $\sigma_{\nu_i \bar{\nu}_i}(s)$, the branching ratio $\mathrm{Br}(Z \to \mathrm{hadrons})$ and the energy distribution functions $dN_i/dE_i$, are well, and the propagation functions $P_i(r, E_i; E)$ are fairly well determined, where the latter were calculated in the framework of the above mentioned reference for different assumptions. The neutrino number density is assumed to be standard, $n_{\nu_i, \bar{\nu}_i}(z = 0) = 112$ cm$^{-3}$. The residual parameters in the proton and photon flux arriving at Earth used as the fitting parameters are the neutrino mass, which determines the resonance energy, and the magnitude of the EEC$\nu$ flux at the resonance energy, which together have impact on the spectrum as described in the following. A small neutrino mass needs a large incident resonance energy,

$$E_\nu^{\mathrm{res}} = \frac{M_Z^2}{2 \, m_\nu} \qquad (6.2)$$

for $Z$-production. A large $E_\nu^{\mathrm{res}}$ results in a large Lorentz boost, thus in a large initial proton or photon energy. In this way the shape of the detected energy spectrum determines the mass of the heaviest relic neutrino[1].

Due to the small width of the $Z$ boson, a narrow width approximation can be applied $\sigma_{\nu\bar{\nu}}(s) = \delta(s/M_Z^2 - 1) \langle \sigma_{\nu\bar{\nu}} \rangle$, which limits the influence of the neutrino fluxes to their magnitude at resonance energy, $F_\nu(E_\nu^{\mathrm{res}}) = F_\nu^{\mathrm{res}}$ rather than their full energy dependence. Therefore only the overall normalization $B$ for the sum of the neutrino fluxes enter the fit, where

$$B \propto \mathrm{Br}(Z \to \mathrm{hadrons}) \langle \sigma_{\nu\bar{\nu}} \rangle E_\nu^{\mathrm{res}} F_\nu^{\mathrm{res}} \,. \qquad (6.3)$$

---

[1]The observed spectrum at Earth is sensitive to one neutrino mass scale solely: The neutrino flux is expected to fall off power like with increasing energy, therefore only the highest neutrino mass scale corresponding to the smallest resonance energy affects the UHECR spectrum.
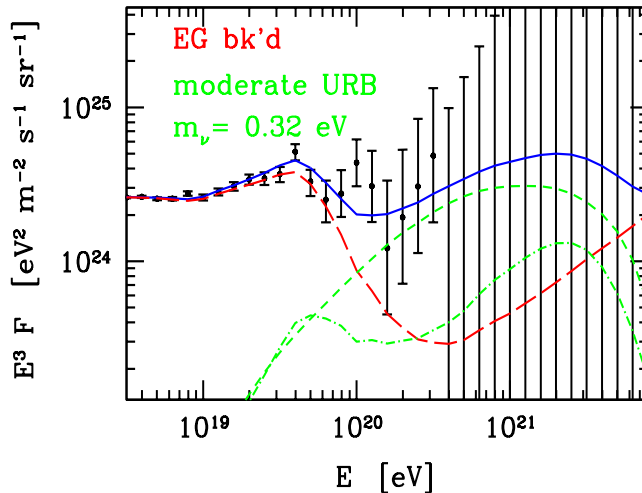
Figure 6.2: The EHECR spectrum for combined data in comparison with the best $Z$-burst fit (solid line), consisting of contributions from background protons (long-dashed), $Z$-burst protons (dash-dotted) and $Z$-burst photons (short-dashed) [63]. The neutrino flux used for the fit is close to the observational upper bound. Adapted from Ref. [64].

This purely $Z$-burst induced spectrum shows up mainly as a bump beyond the GZK cutoff. A second component is added, which is the spectrum of the diffuse background of ordinary cosmic rays, which should have the experimentally observed form of an power law injection spectrum. This is shown in Fig. 6.2.

The result – for the phenomenologically most plausible case, that ordinary cosmic rays are protons of extragalactic origin – is, that the required mass of the heaviest neutrino has to lie in the range $0.08 \text{ eV} \leq m_\nu \leq 1.30 \text{ eV}$. If the highest energy cosmic rays are protons rather than photons, the range narrows down to $0.08 \text{ eV} \leq m_\nu \leq 0.40 \text{ eV}$. Obviously remarkable is, that this is exactly above the lower limit inferred from atmospheric neutrino mass squared splittings and and below the current cosmological upper bounds.
The required neutrino fluxes must be tremendous. Nevertheless, these high fluxes are not yet excluded, but saturating the current observational upper bounds.

## 6.3 The NuTeV Anomaly

The NuTeV collaboration measured $\sin^2 \theta_W$ in $\nu_\mu$ deep inelastic scattering. Although this is a high-precision determination, realized with separate neutrino- and antineutrino beams, high statistics and improved control over experimental systematics, the resulting value [65] $\sin^2 \theta_W = 0.2277 \pm 0.0013\,(stat) \pm 0.0009\,(syst)$ is 3.0 $\sigma$ above the

world average.

This anomaly may be due to physics within or beyond the Standard Model. All approaches to the former are due to QCD corrections. Nuclear shadowing may account for 20% of the NuTeV anomaly [66], strange quark contributions, allowing $s \neq \bar{s}$, for roughly 30% [67], but other groups, calculating the same quantities reported different results, partly even with the opposite sign. Allowing for isospin violating contributions, the phenomenological fits of the MRST group [68] show, that they are capable to remove the NuTeV anomaly completely (or make it twice as large) with this approach. If correct, these effects would be roughly three times the theoretical predictions; effects of this magnitude should be visible in future experiments.

Lacking an established explanation within the Standard Model, we turn our attention to an approach utilizing physics beyond the Standard Model.
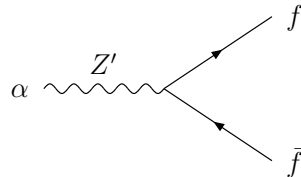
## 6.4 A Light $Z'$ and the UHECR Spectrum

It was proposed by Ref. [69], that a light $Z'$, which evades the current experimental bounds, may account for the NuTeV anomaly and at the same time be an attractive candidate for the production of UHECR events beyond the GZK cutoff via a $Z'$ burst. With the conditions for the new $U(1)'$ gauge symmetry – no mixing with the known $Z$ boson, quark and lepton masses unaffected by the extra $U(1)'$ and coupling of the $Z'$ to the leptons of second generation solely – one arrives at a $B - 3\,L_\mu$ gauge symmetry, for which the effective Lagrangian can be written as

$$\mathcal{L}_{Z'}^{\mathrm{eff}} \;=\; -\frac{g_{Z'}^2}{2\left(M_{Z'}^2 - t\right)} \left[\, \bar{Q}\gamma^\mu Q - \bar{U}^c\gamma^\mu U^c - \bar{D}^c\gamma^\mu D^c - 9\bar{L}_2\gamma^\mu L_2 + 9\bar{E}_2^c\gamma^\mu E_2^c \,\right]^2 \quad (6.4)$$

For consistency with experimental constraints [70, 71] from colliders the $Z'$ must either be light – below the experimental cuts – 2 GeV $< M_{Z'} <$ 10 GeV, or heavy – beyond the collider limits – $M_{Z'} >$ 600 GeV. Taking into account the results of the Muon $(g-2)$ measurements [72], we obtained for the effective coupling the restriction 0.71 TeV$^{-1} \gtrsim g_{Z'}/M_{Z'} \gtrsim$ 0.16 TeV$^{-1}$.

We derived the Feynman rules from Eq. (6.4) for the vertex



$$\pm i\,g_{Z'}\,\gamma^\alpha\,(v_f - a_f\gamma_5)\,c_f \ ,$$

where $c_f = 9(1)$ for leptons (quarks), $v_f = a_f = 1/2$ for neutrinos and $v_f = 1$, $a_f = 0$ for charged leptons and quarks and with the upper sign for the leptons and the lower for the quarks.

From this, we calculated, that for fully accounting for the NuTeV anomaly, an effective coupling of $g_{Z'}/M_{Z'} \approx (0.170 \pm 0.045)\,\mathrm{TeV}^{-1}$ is necessary, assuming $M_{Z'} = 10$ GeV and $t = -20\,\mathrm{GeV}^2$. Therefore the explanation of the NuTeV anomaly by a light $Z'$ is possible, though at the edge of being experimentally excluded.

Assuming a $Z'$ burst analogue to the $Z$ burst described in section 6.2 to account for all events beyond the GZK cutoff, conditions for the combination of the $Z'$ and neutrino masses can be inferred. Calculating the cross section and branching ratio with the Lagrangian (6.4) for the experimentally allowed parameter ranges for the effective coupling, we get the necessary EEC$\nu$ flux of a $Z'$ burst scenario.

For the fit parameters used in the $Z$ burst analysis, both, a heavy $Z'$ with a mass $\sim 600$ GeV as well as a very light $Z'$ with a mass $\sim 2$ GeV, are excluded, since the required neutrino masses are above or below the experimental limits, respectively.

Inferring the "new", $Z'$ induced quantities in terms of the fitted parameters from [63],

$$\frac{(m_\nu)_{Z'}}{(m_\nu)_Z} = \frac{M_{Z'}^2}{M_Z^2} \simeq 81 \quad \text{for} \quad M_{Z'} = 10 \text{ GeV} \qquad (6.5)$$

$$\frac{(F_\nu^{\mathrm{res}})_{Z'}}{(F_\nu^{\mathrm{res}})_Z} = \frac{\langle \sigma_{\nu\bar{\nu}} \rangle_Z}{\langle \sigma_{\nu\bar{\nu}} \rangle_{Z'}} \frac{\mathrm{Br}\,(Z \to \mathrm{hadrons})}{\mathrm{Br}\,(Z' \to \mathrm{hadrons})} \simeq 4.5 \quad \text{for} \quad \frac{g'_Z}{m'_Z} = 0.7 \text{ TeV}^{-1}, \quad (6.6)$$

we get, for the most optimistic values of $M_{Z'} = 10$ GeV and $\frac{g'_Z}{m'_Z} = 0.7$ TeV$^{-1}$ the following results. With the halo background model, it is possible to fit the neutrino mass to a reasonable value of $m_{\nu_3} \sim 0.06$ eV, but for the phenomenologically favored case, that the ordinary UHECRs are of extragalactic origin, the neutrino masses are much too small $0.003$ eV $\lesssim m_{\nu_3} \lesssim 0.01$ eV. Moreover, for all cases, the $Z'$ burst requires an EEC$\nu$ flux, which is $\sim 12$ times higher than in the case of the $Z$ burst. The $Z$ burst demand being at the observational upper limit already, the explanation of the UHECR events beyond the GZK cutoff by means of a light $Z'$ is excluded additionally for that reason.

# Chapter 7

# EEC$\nu$ Spectral Dips

Based on the up-to-date experimental status, the absorption of EEC$\nu$'s on the relic neutrino background seems to be the only process with sensitivity to the C$\nu$B [57, 73, 74, 75], measurable in the upcoming decade. In contrast to cosmological measurements, which link only indirectly to the C$\nu$B, this process might provide direct, scattering based evidence of the relic neutrinos. Therefore, it is worthwhile to extensively study the feasibility of measuring EEC$\nu$ spectral absorption dips.

Since the original proposal of the exploration of $Z$-dips from 1982 [57], significant progress has been made in theoretical and observational cosmology, in experimental neutrino physics and EEC$\nu$ physics. All these areas have direct impact on the observability of the C$\nu$B. A decade or two ago, there was a lot of space for speculations, whereas now, the phenomenologically allowed parameter range is quite strongly restricted. The new findings are:

- **Cosmology**
  In the original work, the calculation was done for a matter dominated, flat universe with a vanishing cosmological constant. Recent observations of large-scale gravity, deep-field galaxy counts and Type Ia supernovae favor a universe with density parameters $\Omega_\Lambda \simeq 0.7$ for the cosmological constant and $\Omega_M$ for (mainly cold and dark) matter [76, 30]. The position of the first acoustic peak in CMB measurements suggests that the universe is flat, i.e. the curvature term is negligibly small. These parameters together with the Hubble constant $H_0$ determine the expansion rate of the universe as a function of lookback time. The EEC$\nu$ dips are strongly affected by the evolution history, since almost certainly the sources are located at cosmological distances.

- **Neutrino masses**
  The oscillation interpretation of the atmospheric neutrino data offer a lower bound for the heaviest of the neutrino mass eigenstates

$$m_{\nu_3} \geq \sqrt{\triangle m_{\text{atm}}^2} > 0.04 \text{ eV} .\tag{7.1}$$

Combining cosmological analysis from large scale structure, gravitational lensing and CMB data, one obtains an upper bound on the sum of the neutrino masses [33, 77]

$$\sum_i m_{\nu_i} \lesssim 1.2 \text{ eV} \,, \tag{7.2}$$

cf. Subsec. 3.2.1, and even stronger bounds can be obtained by including more data sets. Oscillation studies reveal that the mass squared splittings are small compared to the square of (7.2), therefore the cosmological bound per neutrino infers an upper limit of $\sim 0.4$ eV. This bound is much better than laboratory bounds from tritium beta decay or neutrinoless double beta decay, but more model dependent. For the heaviest neutrino mass eigenstates we get

$$0.04 \text{ eV} \lesssim m_{\nu_3} \lesssim 0.4 \text{ eV} \tag{7.3}$$

equivalent to an allowed range for the $Z$-resonance energy in $\nu\bar{\nu}$ annihilation

$$1 \times 10^{22} \text{ eV} \lesssim E_{\nu_3}^{\text{res}} < 1 \times 10^{23} \text{ eV} \,. \tag{7.4}$$

It may be emphasized, that a decade or two ago, the neutrino masses were assumed to be zero but also compatible with being as large as 30 eV.

- **EEC$\nu$ experiments**
  Recent proposals for EEC$\nu$ detectors such as the Pierre Auger Observatory [78], IceCube [79], ANITA [80], EUSO [81], OWL [82], and SalSA [84] encourage the hope, to measure the EEC$\nu$ flux within the next decade. Furthermore, existing EEC$\nu$ observatories, such as RICE [87], GLUE [88], and FORTE [89] have set the first upper limits on the EEC$\nu$ flux in the energy interval of interest, (7.4). Theses limits are displayed in Fig. 7.1 (top).

The organization of this chapter is as follows: In the first section, we present the basic formulas and discuss the simplifications and assumptions we made within. In the next section, we show "pure" absorption dips, i.e. the flux arriving at Earth, divided by the corresponding non-observable flux, without absorption. This normalized quantity is particularly useful to study the dips since it reveals their dependencies on the parameters we used. Therefore, we end this section with the diagnostic potential of absorption dips. In the third section we leave the ground of an idealized model. We present real fluxes as they may be detected at Earth and explore the possibility to resolve and detect the absorption dips for different scenarios. In the last section we present our conclusions.
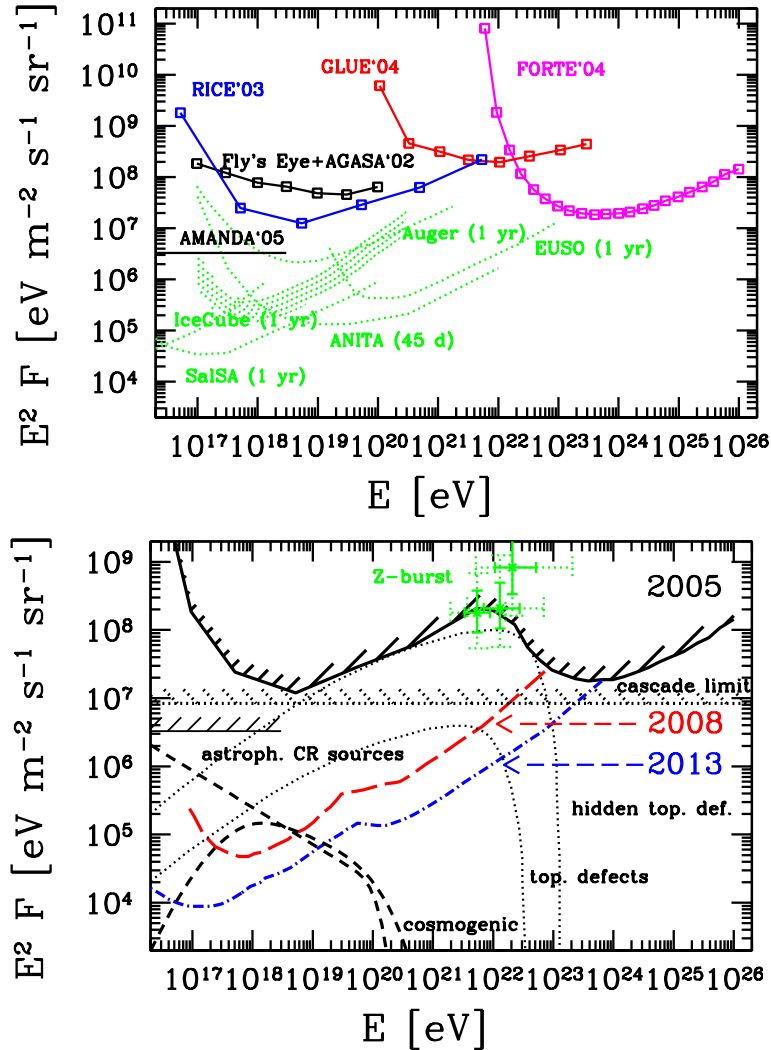
Figure 7.1: Current status and next decade prospects for EEC$\nu$ physics, expressed in terms of diffuse neutrino fluxes per flavor, $F_{\nu_\alpha} + F_{\bar{\nu}_\alpha}$, $\alpha = e, \mu, \tau$; full mixing among the flavors en route to Earth [86] is assumed.

*Top:* Upper limits from RICE [90], GLUE [91], FORTE [92], and Fly's Eye, AGASA [94] and Amanda (for a $E^{-2}$ spectrum) [95]. Also shown are projected sensitivities of Auger in $\nu_e$, $\nu_\mu$ modes and in $\nu_\tau$ mode (bottom swath) [96], ANITA [97], EUSO [98], and SalSA [99], corresponding to one event per energy decade and indicated duration.

*Bottom:* Roadmap for improvement in the next decade (2008 and 2013; adapted from Ref. [85]), corresponding to one event per energy decade, as well as the current (2003) observational upper bound (solid-shaded) obtained from Fig. 7.1 (top). For the year 2008 (long-dashed), we assume 3 years of Auger data and 15 days ANITA flight. For 2013 (dashed-dotted), we assume 8/3/4 years Auger/EUSO/SalSA, and 3 ANITA flights. The sensitivity will improve if further projects such as Auger North and OWL [82] are realized, or if the EUSO flight time is extended. Also shown is a wide sample of predictions for EEC$\nu$ fluxes (discussed in Sec. 7.1.3). Both figures from [83].

## 7.1 EEC$\nu$ Spectral Dips – Basic Formulae

The EEC$\nu$ flux arriving at Earth can be obtained by folding the source emissivity with the propagation function. The latter describes the propagation through the C$\nu$B and marks the absorption of the EEC$\nu$ flux on the cosmic neutrino background, and leaves, when performing the energy and redshift integration of the flux, sizable dips in an otherwise smooth spectrum. The EEC$\nu$ source emissivities are not known. Therefore, we introduce various parameterizations for them in Subsec. 7.1.3.

### 7.1.1 EEC$\nu$ Flux

The differential flux $F_{\nu_\alpha}$, which is defined as the number of neutrinos $N_{\nu_\alpha}$ arriving at Earth with energy $E$, per unit of energy, per unit of area $A$, per unit of time $t$ and per solid angle $\Omega$, is given by

$$F_{\nu_\alpha}(E) \equiv \frac{\mathrm{d}^4 N_{\nu_\alpha}}{\mathrm{d}E\,\mathrm{d}A\,\mathrm{d}t\,\mathrm{d}\Omega} = \tag{7.5}$$

$$\frac{1}{4\pi} \int\limits_0^\infty \mathrm{d}E_i \int\limits_0^\infty \mathrm{d}r \sum_\beta \frac{-\partial P_{\nu_\alpha|\nu_\beta}(E;E_i,r)}{\partial E} \, \mathcal{L}_{\nu_\beta}(r,E_i)\,,$$

where $E_i$ is the energy of the EEC neutrinos at a source located at a distance $r$. The source emissivity distribution $\mathcal{L}_{\nu_\beta}(r,E_i)$ characterizes the neutrino spectra emitted by the sources and the propagation function $P_{\nu_\alpha|\nu_\beta}(E;E_i,r)$ describes the deformation of the spectrum due to the propagation of the EEC$\nu$'s through the C$\nu$B, in the following way: The source emissivity distribution $\mathcal{L}_{\nu_\beta}(r,E_i)$ is defined as the number of neutrinos of flavor $\beta$ per comoving volume, per unit of time, per unit of energy as measured at the source, injected in the C$\nu$B at a distance $r$ with an energy $E_i$. The propagation function $P_{\nu_\alpha|\nu_\beta}(E;E_i,r)$ is given as the expected number of neutrinos of flavor $\alpha$ arriving at Earth above energy $E$, if one neutrino of flavor $\beta$ started with an energy $E_i$ at a distance $r$. The propagation distance $r = ct$ can be related to redshift by

$$\mathrm{d}z = (1+z)\,H(z)\,\mathrm{d}r\,, \tag{7.6}$$

with the evolving Hubble parameter given by

$$H^2(z) = H_0^2 \left[ \Omega_M \,(1+z)^3 + \Omega_k \,(1+z)^2 + \Omega_\Lambda \right]\,. \tag{7.7}$$

The present day value of the Hubble parameter is given by $H_0 = 100\,h\,\mathrm{km}\,s^{-1}\,\mathrm{Mpc}^{-1}$ with $h = 0.71$. The cosmological parameters $\Omega_i$ are contributions to the energy density of the universe as a fraction of the critical density. As default values we have taken $\Omega_M = 0.3$, $\Omega_\Lambda = 0.7$ and $\Omega_k = 0$. These values fit many data sets [76, 30] and are known as the cosmological "concordance model".

In the following, well justified simplifications are made: First, the cross section is assumed to be $Z$-resonance dominated. This leads to a delta function approximation in the s-channel cross section, which is taken into account in Eq.(7.19). Secondly, an interaction is counted as an absorption.

Therefore, particle loss is due to interaction, and energy loss is due to redshift solely. The latter simplification leads to a delta function, which relates the redshift with the energy, and the differential propagation function can be written as:

$$
\frac{-\partial P_{\nu_\alpha | \nu_\beta}(E; E_i, z)}{\partial E} = \delta\left(E - \frac{E_i}{1+z}\right) \sum_j |U_{\alpha j}|^2 \, P_{\nu_j}(E_i, z) \, |U_{\beta j}|^2 ,
\tag{7.8}
$$

where $U_{\alpha j}$ is the leptonic mixing matrix and $P_{\nu_j}(E_i, z)$ is the survival probability of a neutrino of mass eigenstate $m_{\nu_j}$ injected at a redshift $z$ with energy $E_i$. Note, that the neutrinos are produced and detected as flavor eigenstates $\nu_\beta$ (denoted with Greek subscripts), and the survival probability and consequently the dips are characterized by the mass eigenstates $m_{\nu_i}$ (Roman subscripts).

Performing the energy integration in Eq. (7.5) yields

$$
F_{\nu_\alpha}(E) = \frac{1}{4\pi} \int_0^\infty \frac{\mathrm{d}z}{H(z)} \sum_{\beta,\,j} |U_{\alpha j}|^2 \, P_{\nu_j}(E\,(1+z), z) \, |U_{\beta j}|^2 \, \mathcal{L}_{\nu_\beta}(z, E\,(1+z))
\tag{7.9}
$$

In the following, we are interested in two important scenarios of neutrino production. In the first scenario the EEC neutrinos originate from the pion decay chain $\pi^\pm \to \mu^\pm \nu_\mu \to e^\pm \, 2\nu_\mu \nu_e$. These are the so called "hadronic" sources, (Note, that neither we nor the experiments discriminate neutrinos from antineutrinos.) Here, the flavor ratios of the source emissivities are given by

$$
\mathcal{L}_{\nu_e} : \mathcal{L}_{\nu_\mu} : \mathcal{L}_{\nu_\tau} = 1 : 2 : 0 .
\tag{7.10}
$$

The second scenario is, that the neutrinos are emitted "democratically",

$$
\mathcal{L}_{\nu_e} : \mathcal{L}_{\nu_\mu} : \mathcal{L}_{\nu_\tau} = 1 : 1 : 1 ,
\tag{7.11}
$$

which might arise from topological defects not coupled directly to matter, such as for example, mirror matter "necklaces" [102, 103].

For both cases, $\mathcal{L}_{\nu_\mu} + \mathcal{L}_{\nu_\tau} = 2\,\mathcal{L}_{\nu_e}$ is valid. Because of this fact, and since experimentally measured $U_{e3} \ll 1$ and $U_{\mu 3} \simeq U_{\tau 3}$, the fluxes at Earth are well approximated by (see Appendix of [104])

$$
F_{\nu_\alpha}(E) \simeq \frac{1}{4\pi} \int_0^\infty \frac{\mathrm{d}z}{H(z)} \frac{1}{3} \mathcal{L}_\nu^{\text{tot}}(z, E\,(1+z))
\tag{7.12}
$$

$$
\times \sum_{j=1}^3 |U_{\alpha j}|^2 \, P_{\nu_j}(E\,(1+z), z) ,
$$

56
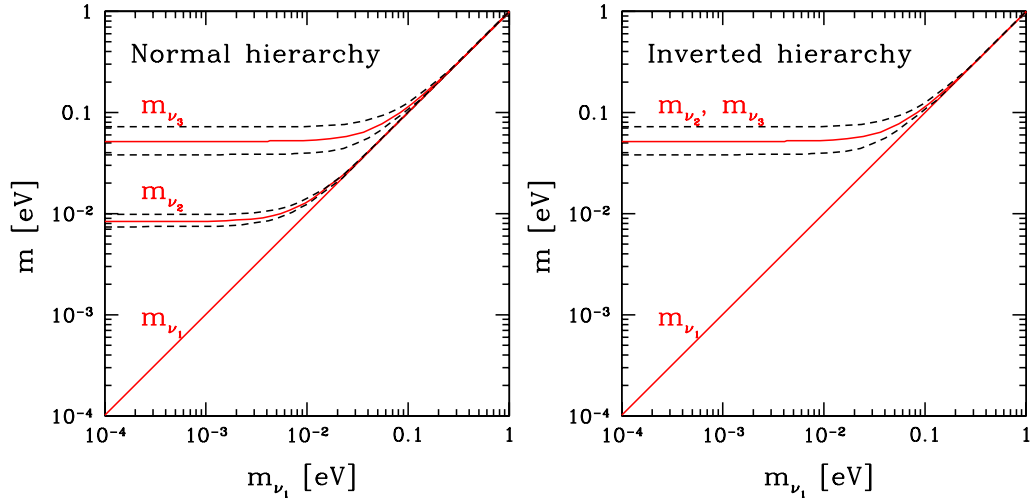
Figure 7.2: Allowed ranges for the neutrino masses as a function of the lightest neutrino mass $m_{\nu_1}$, in the normal (left) and inverted (right) three-neutrino scheme (adapted from Refs. [100, 101]).

where $\mathcal{L}_\nu^{\rm tot}(z, E(1+z))$ is the source emissivity, summed over all flavors.

It is very unlikely that neutrino observatories are fully sensitive to flavor at these high energies. If we take the sum over the neutrino flavors, and apply unitarity of the leptonic mixing matrices, the formula of the flux detected at Earth simplifies to

$$\sum_\alpha F_{\nu_\alpha}(E) \simeq \frac{1}{4\pi} \int_0^\infty \frac{{\rm d}z}{H(z)} \frac{1}{3} \mathcal{L}_\nu^{\rm tot}(z, E(1+z)) \times \sum_{j=1}^3 P_{\nu_j}(E(1+z), z). \quad (7.13)$$

If the neutrino masses are quasi-degenerate as it is the case for[1] $m_{\nu_1}^2 \gg \Delta m_{\rm atm}^2$ or, say, $m_{\nu_1} \gtrsim 0.1$ eV, see Fig. 7.2, the relation

$$m_{\nu_1} : m_{\nu_2} : m_{\nu_3} \simeq 1 : 1 : 1 \quad \text{holds, which implies} \quad P_{\nu_1} \simeq P_{\nu_2} \simeq P_{\nu_3} \quad (7.14)$$

and therefore Eq. (7.12) simplifies to

$$F_{\nu_\alpha}(E) \simeq \frac{1}{4\pi} \int_0^\infty \frac{{\rm d}z}{H(z)} P_{\nu_1}(E(1+z), z) \frac{1}{3} \mathcal{L}_\nu^{\rm tot}(z, E(1+z)), \quad (7.15)$$

for each flavor $\alpha = e, \mu, \tau$.

In the following two subsections we explore the two main ingredients: The survival probability $P_{\nu_j}(E(1+z), z)$ and the source emissivity $\mathcal{L}_{\nu_\beta}(z, E(1+z))$.

---

[1]Throughout this chapter, the smallest neutrino mass is denoted by $m_{\nu_1}$.

## 7.1.2 Survival Probability

The survival probability $P_{\nu_j}(E(1+z), z)$ is given by the number of neutrinos of mass $m_{\nu_j}$ expected at Earth if one neutrino was emitted at redshift $z$ with energy $E_i = E(1+z)$

$$P_{\nu_j}(E(1+z), z) = \exp\left[-\int_0^z \frac{\mathrm{d}\tilde{z}}{H(\tilde{z})(1+\tilde{z})} n_{\bar{\nu}_j}(\tilde{z}) \sigma^{\mathrm{ann}}_{\nu_j\bar{\nu}_j}(s)\right], \qquad (7.16)$$

where

$$s = 2 m_{\nu_j} E(1+\tilde{z}). \qquad (7.17)$$

Note, that the emission redshift is denoted by $z$ and the interaction redshift by $\tilde{z}$, the latter being integrated from emission time to the present time.

We assume the C$\nu$B to be standard, this means, a neutrino background, which decoupled at $t \sim 1\,\mathrm{s}$, no later thermalization happened, no neutrino decay and no neutrino asymmetry is assumed

$$n_{\nu_j}(\tilde{z}) = n_{\bar{\nu}_j}(\tilde{z}) = \langle n_\nu \rangle_0 (1+\tilde{z})^3 = \frac{3}{22} \langle n_\gamma \rangle_0 (1+\tilde{z})^3 = 56 \ \mathrm{cm}^{-3} (1+\tilde{z})^3. \qquad (7.18)$$

The reliability of this assumption is discussed in Chap. 3 and the effect of relaxing this assumption is discussed later. Furthermore, clustering effects are taken into account in Sec. 7.2.2.

As can be seen from Fig. 7.3, where all $\nu\bar{\nu}$- $\nu\nu$- and $\bar{\nu}\bar{\nu}$-cross sections are plotted, the total cross section is dominated by resonant $Z$ production, except for the high energy range. Since the EEC$\nu$ flux is expected to fall off powerlike with energy, these high energy contributions are neglected and a narrow width approximation leads to of the annihilation cross section

$$\sigma^{\mathrm{ann}}_{\nu_j\bar{\nu}_j}(s) = \langle \sigma^{\mathrm{ann}}_{\nu\bar{\nu}} \rangle \, \delta\left(\frac{s}{M_Z^2} - 1\right), \qquad (7.19)$$

where

$$\langle \sigma^{\mathrm{ann}}_{\nu\bar{\nu}} \rangle = \int \frac{\mathrm{d}s}{M_Z^2} \, \sigma^{\mathrm{ann}}_{\nu_j\bar{\nu}_j} = 2\pi\sqrt{2}\, G_F = 40.4 \ \mathrm{nb}. \qquad (7.20)$$

Performing the $\tilde{z}$-integration in Eq.(7.16), the survival probability reads

$$P_{\nu_j}(E(1+z), z) \simeq$$

$$\exp\left[-\left(\frac{\langle n_\nu \rangle_0 \langle \sigma^{\mathrm{ann}}_{\nu\bar{\nu}} \rangle}{H_0}\right) \frac{\left(\frac{E^{\mathrm{res}}_{\nu_j}}{E}\right)^3}{\left[\Omega_M \left(\frac{E^{\mathrm{res}}_{\nu_j}}{E}\right)^3 + \Omega_k \left(\frac{E^{\mathrm{res}}_{\nu_j}}{E}\right)^2 + \Omega_\Lambda\right]^{1/2}}\right] \qquad (7.21)$$

$$\text{for} \quad \frac{1}{1+z} < \frac{E}{E^{\mathrm{res}}_{\nu_j}} < 1, \qquad (7.22)$$
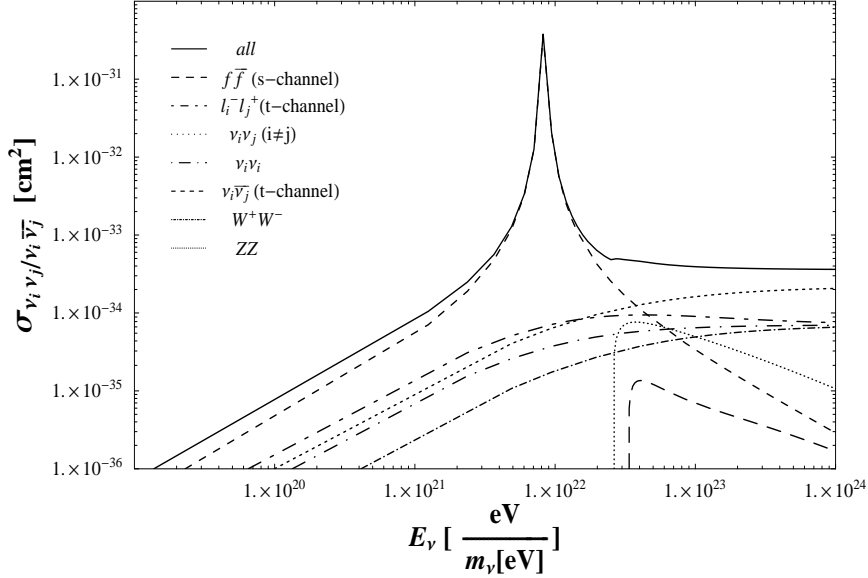
Figure 7.3: All tree level $\nu\bar{\nu}$ and $\nu\nu$ cross sections. The solid line shows the sum over all contributions. The dominant $Z$-resonance peak at $E_\nu = E^{\mathrm{res}} \simeq 4 \times 10^{21}$ eV $(\mathrm{eV}/m_\nu)$ is clearly visible.

and identically one otherwise. If the condition (7.22) is met, an interaction can take place, and the probability for this to happen is given by (7.21). In Fig. 7.4 (top), the energy dependence of the survival probability is shown for different redshifts with the modern concordance cosmological parameters. It exhibits, that using the narrow-width approximation (7.19) for the cross section instead of the full Breit-Wigner energy dependence (dashed) is justified within an overall 5% error. The impact of the most extreme allowed variances of the cosmological parameters is shown in Fig. 7.4 (bottom), amounting to a 5% effect.

Remarkable is the step at the resonance energy $E^{\mathrm{res}}$. It is the annihilation probability of today (neglecting cosmological expansion), which amounts to a few percent

$$\frac{\langle n_\nu \rangle_0 \, \langle \sigma_{\nu\bar{\nu}}^{\mathrm{ann}} \rangle}{H_0} = (0.71/h) \times 3.0 \ \% \ . \tag{7.23}$$

Taking cosmological expansion into account, the annihilation probability is enhanced, it evolves as we go back in time: The neutrino number density scales as $(E_{\nu_j}^{\mathrm{res}}/E)^3 = (1+\tilde{z})^3$, accounting for the higher target density at earlier times. The contribution in the denominator of the exponential function of Eq.(7.21), derives from the evolution of the path length per unit redshift.
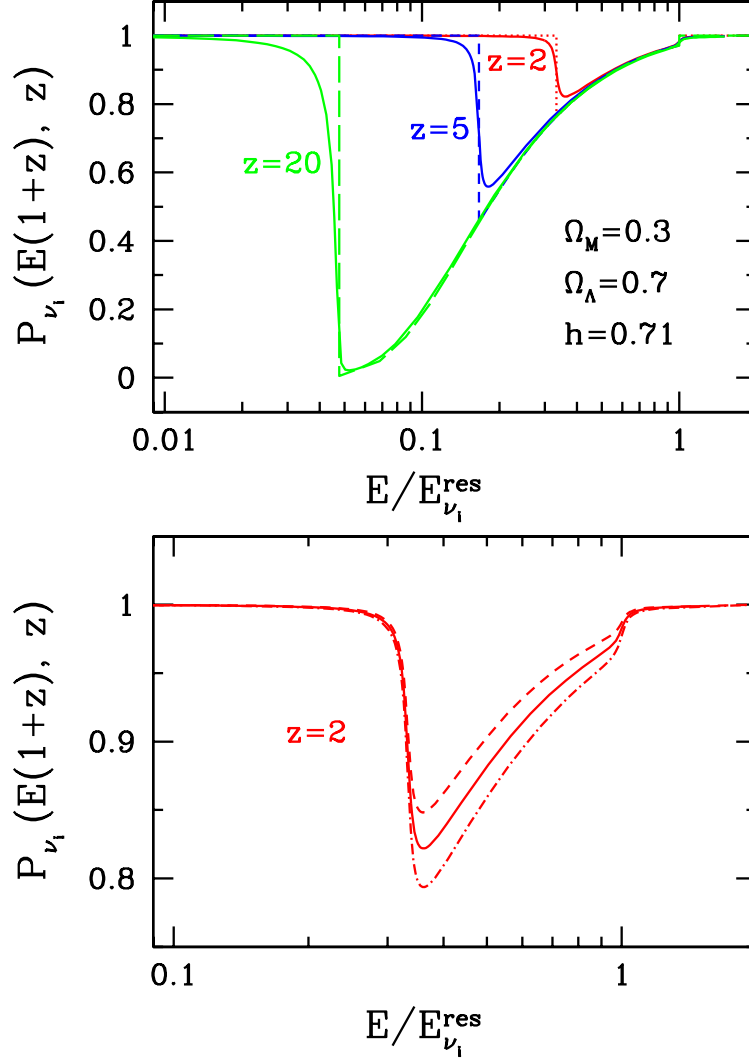
Figure 7.4: The survival probability $P_{\nu_i}(E_i, z)$ of a cosmic neutrino $\nu_i$, injected at redshift $z$ with energy $E_i$, as a function of the energy at Earth, $E = E_i/(1 + z)$, in units of the resonance energy $E_{\nu_i}^{\mathrm{res}} = M_Z^2/2\, m_{\nu_i}$.

*Top:* The narrow-width approximation (7.21), for $z = 2$ (dotted), $z = 5$ (short-dashed), $z = 20$ (long-dashed), and standard cosmological parameters ($\Omega_M = 0.3$, $\Omega_\Lambda = 0.7$, $h = 0.71$), compared with the complete energy dependence from the annihilation cross section of Ref. [74] (solid).

*Bottom:* The survival probability for $z = 2$ and standard cosmological parameters (solid) compared with the most extreme variations allowed by up-to-date global fits: $\Omega_M = 0.20$, $\Omega_\Lambda = 0.78$, $h = 0.81$ (dashed) and $\Omega_M = 0.40$, $\Omega_\Lambda = 0.61$, $h = 0.62$ (dashed-dotted) [30].

### 7.1.3 Neutrino Source Emissivity Distributions

In this subsection, we first parameterize the source emissivity distributions. Thereafter, the source scenarios which may be realized in nature are explained and the corresponding values of the parameters are given.

In the following, we assume, that the EEC$\nu$ sources have identical injection spectra $J_\nu$. Consequently, the redshift $z$ and energy $E$ dependencies of the source emissivity distribution factorize

$$\mathcal{L}_{\nu_\beta}(z, E_i) = \eta(z)\, J_{\nu_\beta}(E_i)\,. \tag{7.24}$$

The injection spectra $J_{\nu_\beta}(E_i)$ are the number of neutrinos $\nu_\beta$ emitted by a single source with energy $E_i$ per unit of energy and the activity $\eta(z)$ is given by the number of sources at redshift $z$, per comoving volume and unit of time. The activity describes any evolution, be it the evolution of a single source or the evolution of the number density of the sources.

In the following, we employ two simple parameterizations, which allow us to study a broad variety of sources. We start with a parameterization motivated by astrophysics [105]

$$\eta_{\mathrm{SFR}}(z) = \eta_0\, \frac{1+a}{(1+z)^{-n_1} + a(1+z)^{n_2}}\,, \tag{7.25}$$

with $\eta_0 = \eta(z=0)$ being the activity in the today's epoch. With the values $a = 0.005(0.0001)$, $n_1 = 3.3(4.0)$, and $n_2 = 3.0(3.0)$, the parameterization fits the star formation rate (SFR) history derived from the blue and UV luminosity density, in line with the extreme ranges of optical and UV measurements without [106] (with [107]) dust extinction corrections. We will refer to these two cases as conservative and generous SFR, respectively. The star formation rate is believed to map out the earliest structures sufficiently bound by gravity to undergo fusion. As such, they may map out the history of Active Galactic Nuclei (AGN) and Gamma Ray Burst (GRB) evolution, two potential sources of the extreme high energy cosmic rays (EHECR's) [105]. The peak activity of such a parameterization is given by

$$1 + z_{\mathrm{peak}} = \left(\frac{n_1}{a\, n_2}\right)^{\frac{1}{n_1 + n_2}}\,. \tag{7.26}$$

The second considered parameterization of the activity is a simple power law Ansatz with cutoffs for nearby and early-time sources $z_{\min}$ and $z_{\max}$

$$\eta_{\mathrm{pow}}(z) = \eta_0\,(1+z)^n\, \theta(z - z_{\min})\, \theta(z_{\max} - z)\,, \tag{7.27}$$

where the evolution is described by a single parameter $n$. This Ansatz has the advantage of easily tractable analytical expressions, and it approximates the SFR Ansatz, if we take $z_{\max} < z_{\mathrm{peak}}$. For astrophysical sources as AGN and GRB, the activity parameters are $n \simeq 3 \div 4$ and $z_{\max} \simeq 2$. For topological defects, the evolution parameter

is low, $n = 3/2$, but $z_{\max}$ arbitrarily large. Throughout this work, $z_{\min} = 0$ is used. The energy range of interest is one or two energy decades around the resonance energy. For this range, we parameterize the source injection spectra with a power law, which is simple, easily tractable and sufficient for our purposes

$$J_{\nu_\beta}(E_i) = j_{\nu_\beta} E_i^{-\alpha} \, \theta(E_i - E_{\min}) \, \theta(E_{\max} - E_i) \, . \qquad (7.28)$$

In most of the source models, the neutrinos originate from pion decay, the latter being produced in inelastic $p\gamma$ and $pp$ scatterings (astrophysical sources) or arising in fragmentation of QCD jets (top-down sources). The resulting neutrino spectra can be well calculated for given proton or pion spectra, but for our purposes it is not worth the effort. Once neutrino dips are measured, these kind of details may be included in the computation. The power law should mimic the neutrino spectra well, with a spectral index $\alpha$ for both, astrophysical and top-down sources, around $\alpha \simeq 1 \div 2$.

To obtain the value of the maximum energy, we need to know the production process of the neutrinos. We distinguish between acceleration of lower energetic particles, the so called bottom-up scenarios, which take place if the sources are of astrophysical origin, and the decay of topological defects or heavy, long lived particles (top-down scenario).

For an astrophysical source the maximum neutrino energy $E_{\max}$ is given by 5 % of the maximum proton energy, $E_{p\,\max}$. In the case of shock acceleration, the energy is determined by the requirement, that the gyromagnetic radius of the accelerated particle in the ambient magnetic field $B$ is less than the spatial dimension $R$ of the source

$$E_{p\,\max}^{\mathrm{shock}} \simeq 10^{21} \text{ eV} \, (R/\mathrm{kpc}) \, (B/\mathrm{mG}) \, . \qquad (7.29)$$

Even higher energies are possible in proposed non-shock mechanisms, such as unipolar induction, acceleration in strong electromagnetic waves in plasmas (wakefields) [108], or by magnetic recombination in the vicinity of massive black holes [109]. In any case, astrophysical sources are strongly restricted in maximum energy.

This is not the case in the same extent for top-down sources, where the neutrino maximum energy is given by roughly 10 % of the mass (energy) of the motherparticle (underlying phase transition). Popular examples are $M_{\mathrm{wimpzilla}} \sim 10^{11 \div 13}$ GeV from the end of inflation or $M_{\mathrm{GUT}} \simeq 10^{16}$ GeV from grand unification.

The minimum energy cutoff is taken to be zero, $E_{\min} = 0$ throughout this work.

In general, there may be several classes of sources with different parameters for the activity and source injection spectra. Taking the sum over all sources, would presumably give an overall spectrum with kinks and dips. But since sources, providing particles of these high energies we need for our investigation, are rare anyway, there may be only one class in the high energy regime. Therefore, we continue our work within the one class model.

Another possibility is, to look for point sources. Here, the disadvantage is that the event rate of a single source is presumably too low to resolve a detailed structure like an absorption dip.

## 7.2 Phenomenology of Absorption Dips

Equipped with the above parameterizations and formulas, prepared with the phenomenology and the allowed parameter ranges, we are ready to calculate the flux detected at Earth. For simplicity and to keep the overview, we present throughout this section the flux detected at Earth divided by the flux without absorption. This quantity gives excellent possibilities to study the influences of the different parameters to the size and shape of the dips.

The dependence of the $Z$-dips on various parameters may serve as an diagnostic tool for them. This is presented in the second subsection.

### 7.2.1 Case Studies of Absorption Dips

Since the EEC$\nu$ source type as well as the neutrino mass spectrum are not known, we present various scenarios for different source classes and neutrino mass parameters.

We start with an illustrative and simple example. Combining the power-law parameterizations for the activity, Eq. (7.27) and the source injection spectra, Eq. (7.28), the source emissivity reads

$$
\begin{aligned}
\mathcal{L}_{\nu_\beta}^{\mathrm{pow}}(E(1+z), z) \;=\; & \eta_0 \, j_{\nu_\beta} \, (1+z)^{n-\alpha} \, E^{-\alpha} \\
& \times \theta(z_{\max} - z)\, \theta(E_{\max} - E_i)\,,
\end{aligned}
\tag{7.30}
$$

where cutoffs for nearby and low energetic neutrinos have been omitted ($z_{\min} = E_{\min} = 0$, see previous section). Thus, in the normalized flux the explicit dependence on $\alpha$ drop out, being sensitive to the combination $(n - \alpha)$ solely. We vary only the source parameters $(n - \alpha)$, $z_{\max}$ and $E_{\max}$, while we assume the mass eigenstates to be quasi-degenerate.

In Fig. 7.5, the normalized spectrum is shown for three values of $z_{\max} = 2, 5, 20$ and three values of $n - \alpha = 0, 2, 4$. The maximum energy is chosen to be $E_{\max} \geq E_{\nu_1}^{\mathrm{res}}/(1 + z_{\max})$. The dips extend from $E = E^{\mathrm{res}}$ down to $E = E^{\mathrm{res}}/(1 + z_{\max})$. The depth increases, the earlier the sources started emission (larger $z_{\max}$), the stronger the source evolves and the flatter the injection spectrum is (larger $n - \alpha$). For fixed $n - \alpha$ and with increasing $z_{\max} = 2, 5, 10$ the absorption depths are roughly 5, 8 and 15 % for $n - \alpha = 0$; 7, 18 and 55 % for $n - \alpha = 2$; and 10, 27 and 77 % for $n - \alpha = 4$, respectively.

For the dips to be pronounced, there is a strong preference for sources, which turned on at early times with strong evolution and/or flat spectrum. The tendencies of the
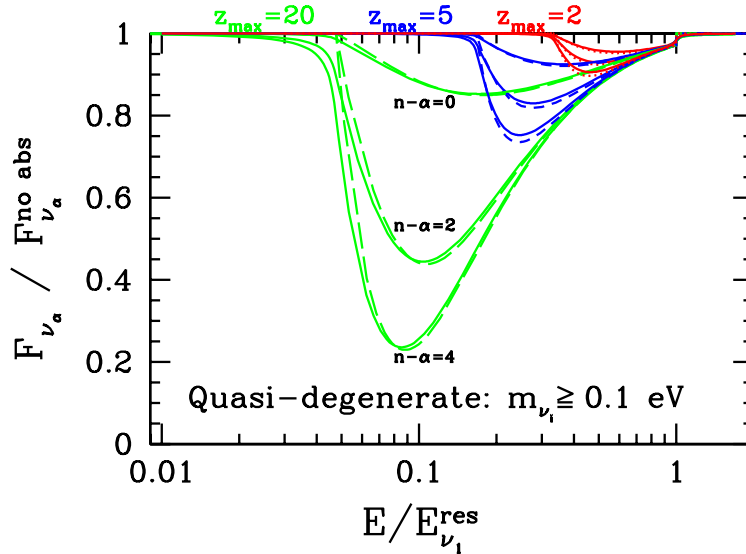
Figure 7.5: Predicted flux $F_{\nu_\alpha}$ of neutrinos $\nu_\alpha = \nu_e, \nu_\mu, \nu_\tau$ at Earth, normalized to the predicted flux without absorption, for a source emissivity characterized by power-law activity (7.27) and injection spectrum (7.28) and quasi-degenerate neutrino masses. $E/E_\nu^{\mathrm{res}}$ scales as the degenerate mass $m_\nu$. Its graph is shown for $z_{\max} = 2$ (dotted), 5 (short-dashed), and 20 (long-dashed), for each choice of $z_{\max}$ for $n - \alpha = 0$ (upper), 2 (middle), and 4 (lower). The corresponding solid lines show the same quantity evaluated with the complete energy dependence of the annihilation cross-section from Ref. [74] arising from the finite $Z$-width, instead of exploiting the zero-width approximation (7.19). For all curves, $E_{\max} > E_{\nu_1}^{\mathrm{res}} (1 + z_{\max})$ is assumed.

sources provided by nature is working in opposite direction: The sources of astrophysical origin may have a strong evolution, but turned on quite recently ($z_{\max} \sim 2$), furthermore, they are rather restricted in energy. Topological defect sources have no strong evolution, but on the other hand, they may have started to decay a long time ago, and the maximum energy can be large.

To understand the origin on the parameter dependencies of the dips, one may have a look to the 3-D plots in Appendix A, where the normalized flux in the $E$-$z$-plane is shown before performing the $z$-integration for different parameter choices. Next, we study the dependence of the absorption dips on the neutrino masses using four different scenarios for the activity: The generous and the conservative SFR and two power law activities - one mimicking a topological defect, the other a bottom-up acceleration source.

For the neutrino mass pattern, we take the mass-squared splittings from atmospheric and solar neutrino data, $\Delta m_{\mathrm{atm}}^2 = 2.6 \times 10^{-3}\,\mathrm{eV}^2$ and $\Delta m_{\mathrm{sun}}^2 = 6.9 \times 10^{-5}\,\mathrm{eV}^2$, respectively, then vary the smallest neutrino mass from $m_{\nu_1} = 0.4\,\mathrm{eV}$ to $m_{\nu_1} = 2 \times 10^{-3}\,\mathrm{eV}$

64

and employ different neutrino mass scenarios.

The resulting absorption dips are shown in Fig. 7.6 - 7.9 for different neutrino mass spectra from the upper to the lower panel, and different source types from the left to the right.

The upper panel shows a quasi-degenerate neutrino mass pattern with $m_{\nu_1} = 0.4$ eV for different sources. The three dips coincide at the same resonance energy, and therefore this scenario provides the deepest dip. Furthermore, in this case, all three masses carry not only a common, but also the largest neutrino mass, leading to the lowest resonance energy. The fluxes fall off with increasing energy, therefore, a lower the resonance energy implies a higher the flux at the relevant energies and thus a better statistics in an experiment.

The second panel shows a normal hierarchical neutrino mass spectrum with the lowest neutrino mass being $m_{\nu_1} = 0.01$ eV. Here, the two low energy dips – corresponding to neutrino masses $m_{\nu_2} = 0.013$ eV and $m_{\nu_3} = 0.053$ eV in Fig. 7.2 (left) – overlap significantly.

In the third panel, we choose a normal hierarchical neutrino mass spectrum with a very small neutrino mass $m_{\nu_1} = 0.002$ eV for the lightest neutrino and the corresponding central values of $m_{\nu_2} = 0.0085$ eV and $m_{\nu_3} = 0.052$ eV from Fig. 7.2 (left),. Here, we see neutrino absorption spectroscopy at its best! Together with a good experimental resolution - and, of course, high statistics - this scenario would provide a measurement of the three individual neutrino masses, resolving not only the absolute scale of the neutrino masses but also the unknown hierarchy.

The fourth panel shows an inverted hierarchy with the same lightest neutrino mass. With $m_{\nu_1} = 0.002$ eV, the central values for the nearly-degenerate heavy masses are $m_{\nu_2} \simeq m_{\nu_3} = 0.052$ eV, from Fig. 7.2 (right). The lower two dips are not resolved individually and thus appear twice as deep as the single dip of $m_{\nu_1}$.
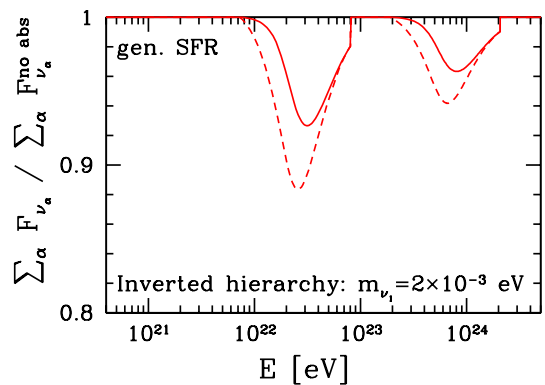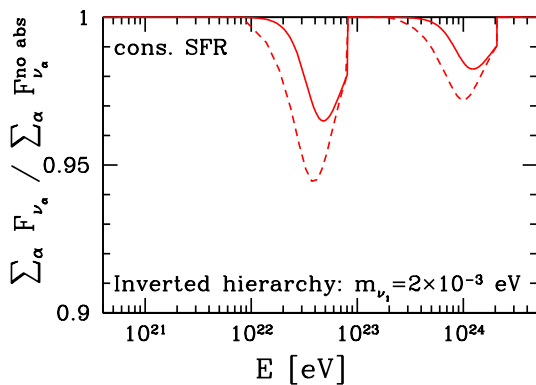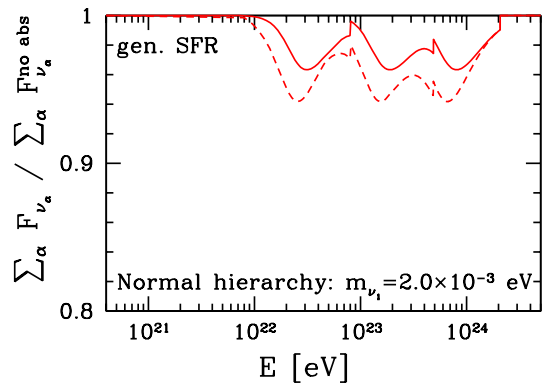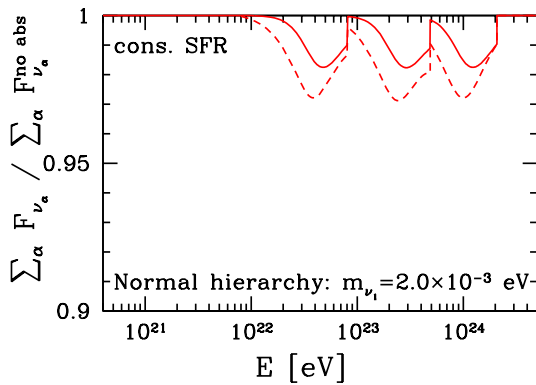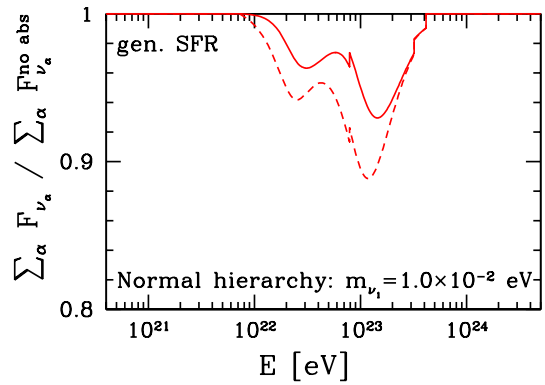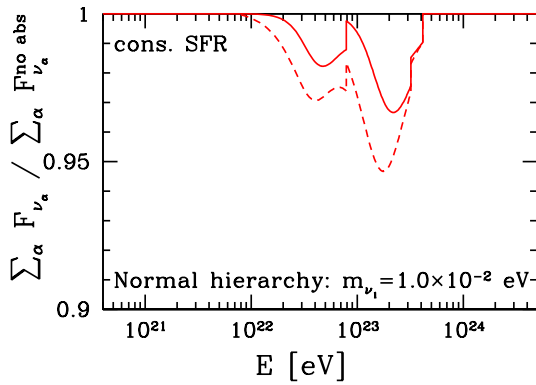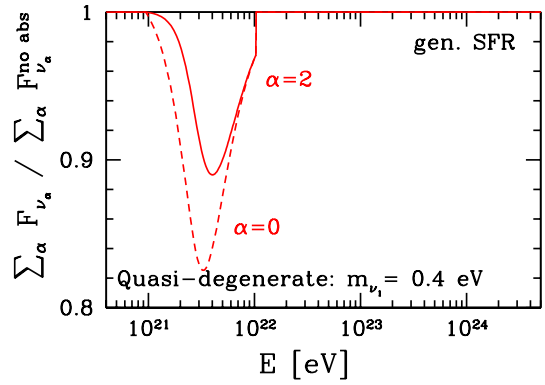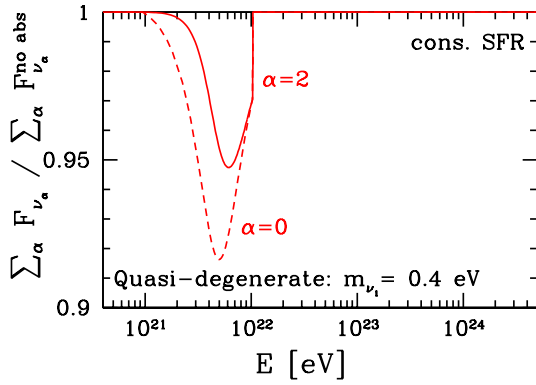
Figure 7.6: Description is given below.
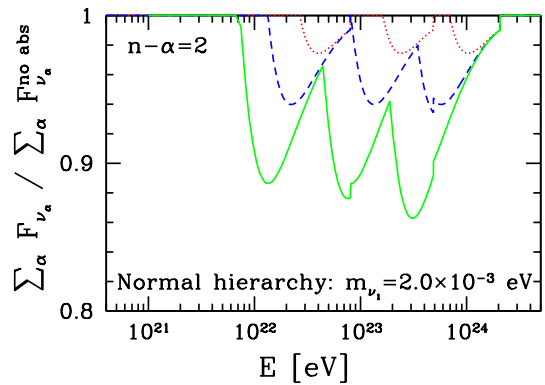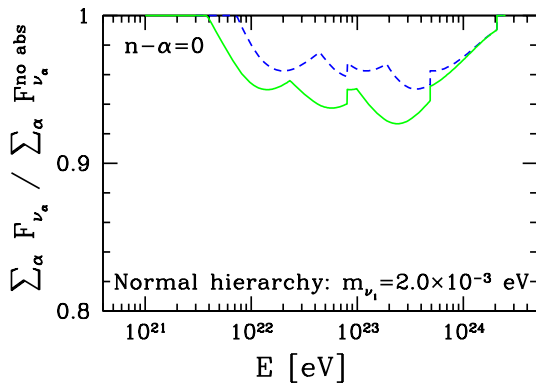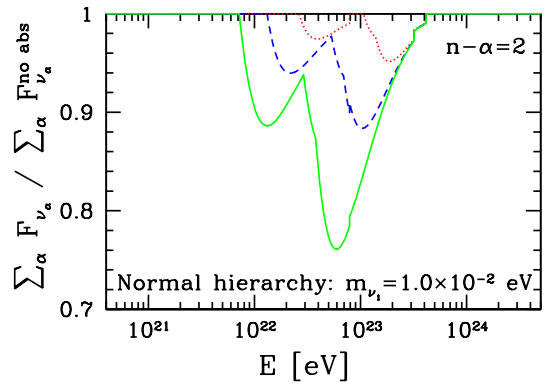


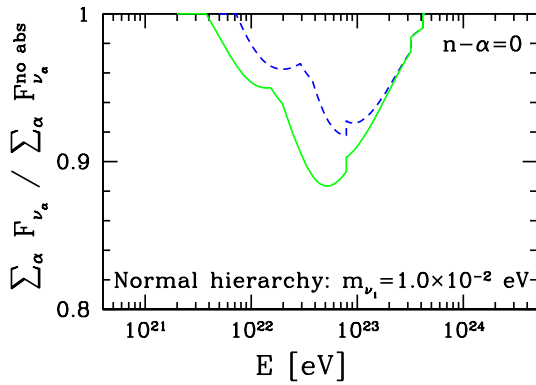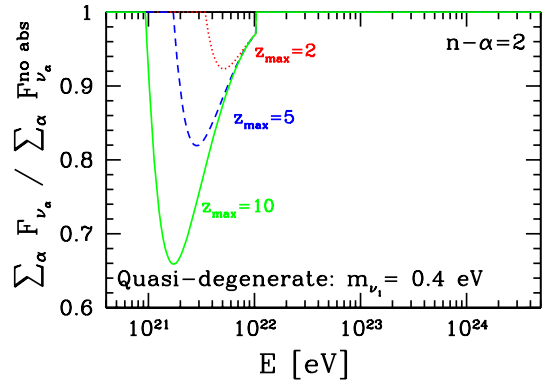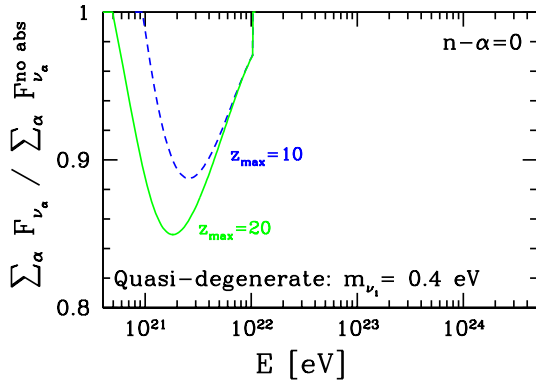Figure 7.7: Description is given below.
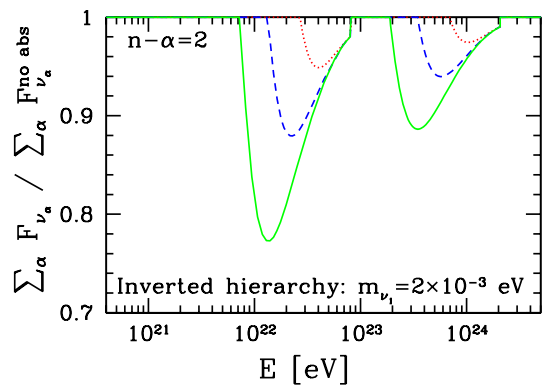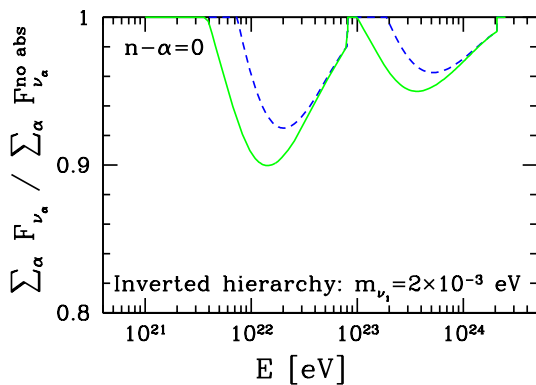
Figure 7.8: Description is given below.

Figure 7.9: Description is given below.

Figure 7.6:  Predicted flux of neutrinos summed over flavors at Earth (7.13), normalized to the predicted flux for no absorption, for a conservative SFR activity (7.25) injection-spectrum indices $\alpha = 2$ (solid) and $\alpha = 0$ (dashed) (7.28), and neutrino spectra which are quasi-degenerate (top), normal-hierarchical (2nd and 3rd panels), and inverted-hierarchical (bottom panel). For all curves it is assumed that $E_{\max} > E_{\nu_1}^{\rm res} (1 + z_{\max})$.

Figure 7.7:  Same as Fig. 7.6, but with the generous SFR activity (7.25).

Figure 7.8:  As in Fig. 7.6, but with a power-law activity (7.27) and $n - \alpha = 0$, with $z_{\max} = 10$ (short-dashed), 20 (solid), mimicking a topological defect source scenario. See also Fig. B.1 and B.2 in the Appendix.

Figure 7.9:  Same is Fig. 7.8, but with $n - \alpha = 2$ fixed, and $z_{\max} = 2, 5, 10$ (from upper to lower curves), corresponding to a bottom-up acceleration source scenario.

The $m_{\nu_1} = 2$ meV neutrino mass is critical in the sense, that all neutrinos are still non-relativistic for redshifts upto $z = 2$. For lighter neutrinos and/or larger $z$, the neutrinos become relativistic. The resulting effect is, that the equation for the resonance energy changes, the neutrino mass must be replaced by the averaged energy $m_\nu \rightarrow \langle E_\nu \rangle$, which is redshift dependent $\langle E_\nu \rangle = (\langle p_\nu^2 \rangle + m_\nu^2)^{1/2} = (\langle p_{\nu 0}^2 \rangle (1 + z)^2 + m_\nu^2)^{1/2}$. This leads to the effect, that the peak in the cross section is smeared out and thus reduced (disadvantage for the detectability) as well as shifted to lower energies (advantage for the detectability). These effects have been calculated in Ref. [93] at the level of survival probabilities.

We are mainly interested in the high mass dips, since these seem to be the only ones, which are detectable. In this case, the contributions arising from times, when neutrinos were nonrelativistic, are subdominant, therefore we continue without taking into account these relativistic effects.

It may be noted, that the two lower panels in Figs. 7.6–7.9 remain exact applicable for $z_{\max} > 2$, only if one simply removes the contribution from the highest energy dip, at $\sim 10^{24}$ eV. These high energies are not very likely to be observed.

**To conclude:**
First of all, the existence of absorption dips requires a neutrino flux at resonance energy, therefore $E_{\max}$ has to be large enough. The resonance energies in turn are determined by the neutrino mass spectrum.

Secondly, large values of $n - \alpha$, $z_{\max}$ and/or $E_{\max}$ as well as a quasi-degenerate neutrino mass spectrum contribute separately to an enhancement of the dip depth. Unfortu-

nately, typical source candidates feature optimal values with regard to a suitable dip only for some of the parameters. While bottom-up sources may have large evolution ($n - \alpha$ large), they are strongly restricted in maximum energy and redshift ($E_{max}$ and $z_{max}$). Topological defects are not restricted in redshift and their spectrum may extend to comparatively large energies – but their evolution is very low.

Thirdly, perfectly resolved dips are not only a measurement of the C$\nu$B, but also a determination of all neutrino masses – and other parameters as the next subsection will present.

## 7.2.2 Diagnostic Potential of EEC$\nu$ Dips

As we have seen in the previous subsection, the shape, depth and size of the dips is sensitive to parameters from different physics areas, namely cosmology, astrophysics and neutrino physics. The fact, that the dip is dependent on many unknown parameters may be a disadvantage on the one hand, but on the other hand, once measured with high accuracy, the dip may exhibit information about all these parameters with hardly no degeneracy. In the following, we give a brief overview of determination and disentanglement of the parameters.

- **Neutrino mass pattern** – The neutrino mass determines the resonance energy, which in turn fixes the high energy tail of the neutrino dip. The otherwise smooth fluxes shown in Figs. 7.6 – 7.9 feature a characteristic step at the resonance energy with the relative height $\langle n_\nu \rangle \langle \sigma \rangle / H_0 \simeq 1\%$, 2% or 3% for non-, double- and total-degenerate neutrino masses, respectively.

  However, this oversimplified picture changes, if the secondary neutrinos, produced in the $Z$ decay are taken into account[2]. These neutrinos amount to 40% of the primary EEC$\nu$'s and show up at half of the original energy, $E = \frac{1}{2} E^{res}/(1 + z)$. The effect on a single dip is the partial fill-up of the dip and the occurence of a bump below the low energy end of the dip. An example is shown in Fig. 7.10. For more than one dip, the characteristic drop in the spectrum at the resonance energy can be wiped out by secondary neutrinos at appropriate energies. In particular, the characteristic drop in the spectrum is not affected for degenerate neutrino masses or sufficient separation of the dips with respect to the energy.

  As stated above, relativistic effects due to the thermal motion of the relic neutrinos shift the dips to lower energies and let them appear shallower. These relativistic effects should be irrelevant, if neutrino masses are degenerate. Including all cross section contributions, see Fig. 7.3, will soften the "step" at resonance energy, but not wipe it out.

---

[2]Additionally, tertiary neutrinos arise from e.g. $\pi$ or $\mu$ decay. They occur at considerably lower energies and are omitted in the discussion for simplicity.

- **Maximum redshift and maximum energy** – Either the maximum redshift or the maximum energy determines the low energy tail of the dip. At a certain time $z_{max}$ sources started to emit neutrinos with a certain maximum energy $E_{max}$. This energy evolves with time as $E_{max}/(1+z)$.

  If we consider a fixed energy $E$ at Earth, and go back in time, then the flux drops down to zero at a certain value of the redshift. This may be due to the fact, that the sources did not emit neutrinos earlier ($z_{max}$ restriction) or due to the fact, that at this time this was the maximum energy ($E_{max}$ restriction), see 3-D in Appendix A in the Appendix.

  If the discussed low redshift cutoff of the flux is restricted by $z_{max}$, the low energy tail of the dip is rather sharp and the position in energy of this edge at $E = E^{res}/(1+z_{max})$ determines directly $z_{max}$, see for example 7.5. If the integrand of the flux in lookback time is restricted by $E_{max}$ rather than $z_{max}$, the dip shows a different behaviour, namely a low energy tail without a sharp edge. In both cases, the maximum energy can be determined from the high energy end of the EEC$\nu$ flux.

  This discrimination is motivated by the expectation, that the "$z_{max}$ restriction" applies to astrophysical sources, while the "$E_{max}$ restriction" is relevant for bottom-down sources (topological defects or the decay of supermassive particles). An example for the possibility to disentangle these two classes of sources is shown in Fig. 7.11.

  Again, the question occurs, whether these effects are still visible, if one takes into account relativistic effects. A dip restriction by $z_{max}$ implies, that $z_{max}$ is not too large (because a huge maximum energy is rather unlikely, although very welcome,) therefore, if the neutrino masses are not too small, relativistic effects should be negligible in this case. In the other case, where $E_{max}$ limits the integrand, relativistic effects smooth the low energy tail of the dip in addition, while the high energy tail of the dip remains unaffected, if neutrinos are non-relativistic today. However, to resolve these effects, a good energy resolution is required.

- **Cosmological parameters** - The cosmological evolution affects the shape and the depth of the dip in a characteristical way. The degeneracy with the source parameters $(n - \alpha)$ will not be resolvable within an overall 5% error. Therefore, absorption dips do not provide an independent measurement of the cosmological parameters and we refer to the values from recent CMB fits. Compared to the previously favored flat matter dominated model with $\Omega_M = 1$, the currently preferred $\Lambda$CDM concordance model predicts deeper dips, see Fig. 7.12.

- **Spectral index $\alpha$** - The spectral index $\alpha$ must be determined from the spectrum at energies higher or lower than the dip.

- **Source evolution index $n$** - Once $\alpha$, $z_{\max}$ and $E_{\max}$ are determined, the evolution index $n$ is simply fixed by the depth of the dip – if we assume the cosmological parameters to be determined from other measurements. The shape, if resolved, then serves as a cross check for the source parameters.

- **Neutrino mixing matrix** – Flavor discrimination is experimentally not established, but a simulation, which effectively discriminates $\nu_e$-$\nu_{\mu,\tau}$, is required for the dip analysis, and seems feasible (see discussion in Subsec. 7.3.2), depending on the available statistics. If flavor discrimination is possible, it is a powerful tool to acquire information about the neutrino mixing matrix.
  Neutrino oscillations tend to produce a flux of roughly equal admixtures of each flavor after the propagation lengths considered here. Therefore the different depths of the dips of one mass eigenstate, but in the EEC$\nu$ fluxes of different flavor, show the flavor content of the corresponding mass eigenstate. The predicted EEC$\nu$ fluxes arriving at Earth

$$ F_{\nu_\alpha}(E) \simeq \frac{1}{4\pi} \int\limits_0^\infty \frac{\mathrm{d}z}{H(z)} \frac{1}{3} \mathcal{L}_\nu^{\text{tot}}(z, E(1+z)) \times \sum_{j=1}^3 |U_{\alpha j}|^2 P_{\nu_j}(E(1+z), z) \ (7.31) $$

  for $\nu_\alpha$ being $\nu_e$, $\nu_\mu$ and $\nu_\tau$ are shown in Fig. 7.13 for different neutrino mass spectra. Noticeable here is, that even if revealing only the heaviest mass eigenstate, the normal and the inverted mass hierarchy would be distinguishable. More on that topic can be found in [93].

- **Neutrino clustering** – If neutrinos are heavy enough to cluster locally, this may be visible in the neutrino dips. The signature would be a depletion of the EEC$\nu$ flux in a certain energy range corresponding to the respective redshift distance and spatial dimension of a cetain object. In Fig. 7.14 the normalized EEC$\nu$ flux is shown for a scan into the direction of the Virgo cluster. Remarkably is that, if resolved perfectly, even a "small" overdensity of a factor of two would be easily visible. Being not deflected by a magnetic field, neutrinos could provide a great tool to explore the mass distribution of the universe by tomography. Problems will occur in resolving such small energy ranges, in particular if considering the fact, that in Fig. 7.14 a point source observation is shown, meaning only events arriving from the direction of the Virgo cluster are taken into account. Furthermore, a limitation arises due to the fact, that light neutrinos would cluster only at late times [26], making it impossible to record the density contrast for large redshifts.

- **Lepton asymmetry** – In this work we considered the neutrino asymmetry to be negligible. Assuming a suppression of the equilibration between the flavors, see Subsec. 3.2.3, $\xi_{\mu,\tau} \sim 2.6$ is allowed [35]. In comparison to $\xi = 0$, this

enhances the neutrino number density summed over all flavors by a factor of 3, thus increases the depth of the dip and in particular the characteristic drop in the spectrum at the resonance energy by the same amount. In the case, that all three dips are revealed, or, later, all neutrino masses are fixed from other experiments, this would provide a unique possibility to be sensitive to the present-day neutrino asymmetry. Usually, oscillation induced flavor equilibration is assumed, then the neutrino asymmetries are restricted from BBN to be $\xi \lesssim 0.22$, which leads to an increase in the number density of $\lesssim 2\%$. We see, the measurement of neutrino spectral dips can exclude large present-day neutrino asymmetries, but is not sensitive enough to probe a small neutrino asymmetry.
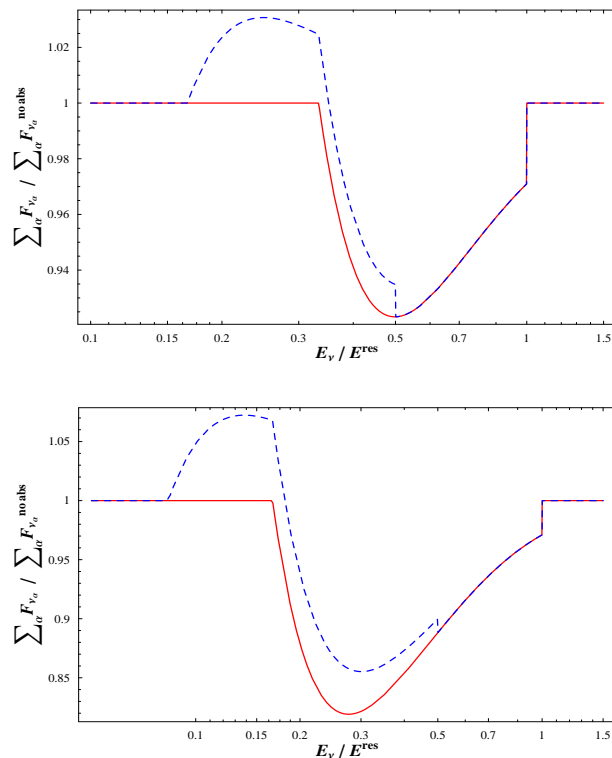


Figure 7.10: Predicted EEC$\nu$ flux arriving at Earth normalized to a flux without absorption, for the approximation, that every interaction is counted as an absorption (solid) and, for the case that secondary neutrinos from the $Z$-boson decay are taken into account (dashed) – for the parameter choices $z_{\mathrm{max}} = 2$, $n - \alpha = 2$ (top) and $z_{\mathrm{max}} = 5$, $n - \alpha = 2$ (bottom). The significant pile-up effect at the low energy edge of the dip may facilitate the detection of the dips. The impact of the secondary neutrinos on the dip is strongly dependent on the source (mainly $z_{\mathrm{max}}$).
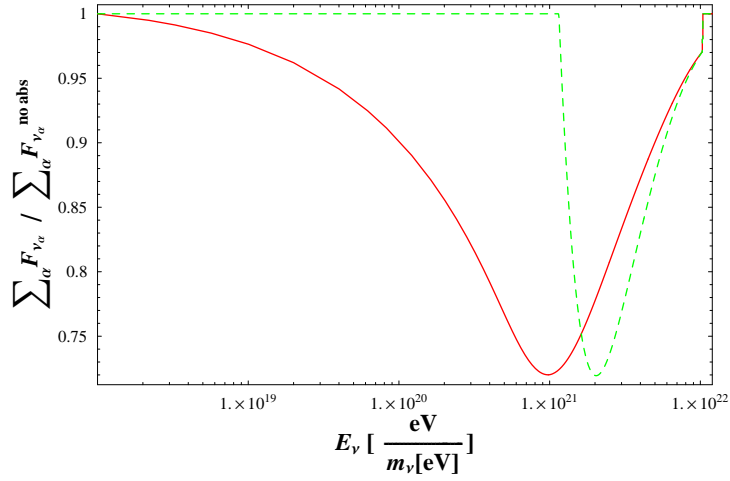
Figure 7.11: Predicted EEC$\nu$ flux arriving at Earth normalized to a flux without absorption for "$z_{max}$-" (dashed) and "$E_{max}$-restricted" (solid) sources with $E_{max} = 10^{25}$ eV (see also text). The dashed curve shows the predicted flux of an astrophysical source with the parameters $n - \alpha = 2$ and $z_{max} = 8$, the solid curve shows the flux of an topological defect source with the parameters $n - \alpha = 0$ and $z_{max} = \infty$. The depths are the same, but the shape shows significant differences in particular at the low enegy tail.
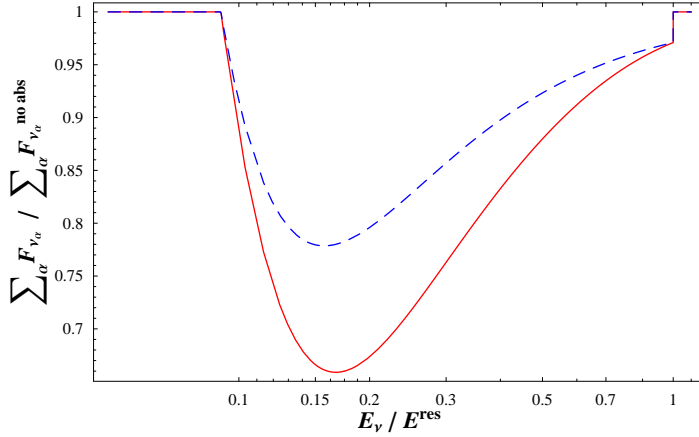


Figure 7.12: Predicted EEC$\nu$ flux arriving at Earth normalized to a flux without absorption with source parameters $z_{max} = 10$ and $n - \alpha = 2$ for a flat universe $\Omega_{tot} = 1$. The red (solid) curve corresponds to the standard comological parameters $\Omega_M = 0.3$ and $\Omega_\Lambda = 0.7$ and the blue (dashed) curve corresponds to a matter dominated flat universe without cosmological constant, $\Omega_M = 1$ and $\Omega_\Lambda = 0$.
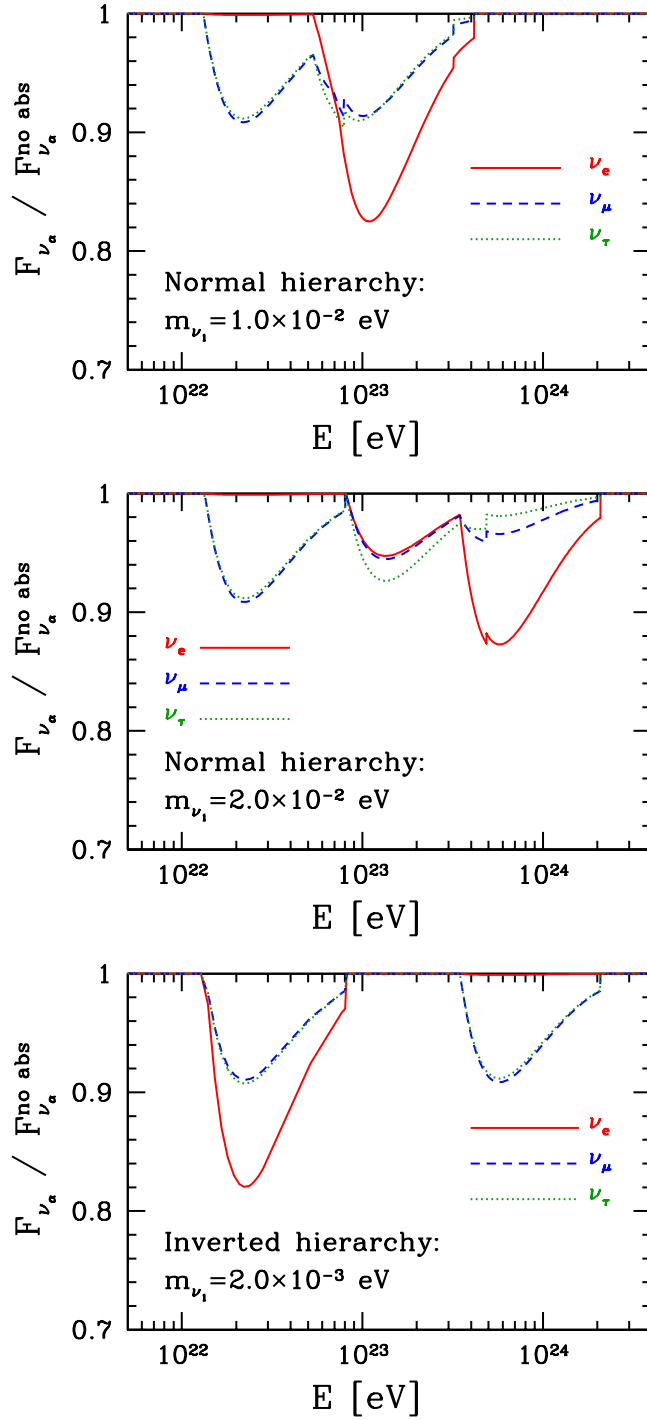
Figure 7.13: Predicted EEC$\nu$ flux $F_{\nu_\alpha}(E)$ arriving at Earth normalized to a flux without absorption for $\nu_\alpha$ being $\nu_e$ (solid), $\nu_\mu$ (dashed) and $\nu_\tau$ (dotted) and for different neutrino mass spectra. The parameters of the leptonic mixing matrix are current best fit values taken from Ref. [110]. The source parameters are $n - \alpha = 2$ and $z_{\max} = 5$, mimicking an astrophysical source.
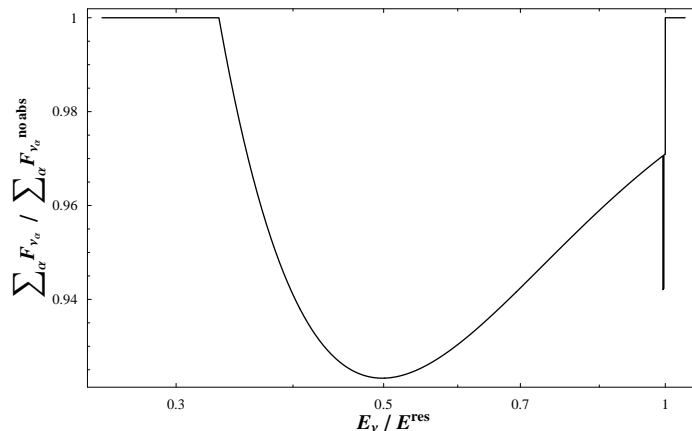
Figure 7.14: Predicted EEC$\nu$ flux arriving at Earth normalized to a flux without absorption from the direction of the Virgo cluster located at an distance of 15 Mpc, with a size corresponding to an angle on the sky of $\theta_{Virgo} = 10°$, with an assumed overdensity of $n_\nu/\langle n_\nu \rangle = 2$, parameters are taken from [26]. Only events arriving from this particular angle $\theta_{Virgo}$ are plotted.

## 7.3   Experimental Prospects

In this section, we explore the detectability of the neutrino dips. In section 7.2.1, we studied all interesting features of the spectral dips, i.e. shape, size and depth, and analyzed the dependencies on the corresponding parameters. We did not examine the possibility to detect and resolve them experimentally within the forseeable future. To investigate this, we have to include the statistics-significant quantity $\eta_0 \, j_\nu$, which determines the absolute mormalization of the neutrino flux and was omitted in our discussion upto now. Throughout this section, we work with two categories of sources with respect to the scale, which are described in the following.

The cascade limit applies to sources, where the neutrinos are produced in the decay of pions [111, 112]. Since pions are produced isospin-symmetric, $\pi^+$, $\pi^-$ and $\pi^0$ occur with the same probability. Neutral pions decay to photons, $\pi^0 \rightarrow 2\gamma$, the photons cascade down in energy and are then detected at low energies (30 MeV – 100 GeV) as diffuse gamma-ray background. Therefore, from the number of photons at low energy, we are able to introduce an upper bound for high energy neutrinos. This type of sources are called "transparent" sources or hadronic sources.

This limit does not apply, if the neutrinos originate from the decay of particles, which do not couple directly to Standard Model particles. The decay processes then take place in a hidden or "mirror" sector. This kind of source, where neither nucleons nor photons escape, is called "hidden" source.

Table 7.1: Expected number of neutrinos (including anti-neutrinos) to be detected in upcoming EEC$\nu$ observatories with energies in the indicated intervals until the indicated year, for two different EEC$\nu$ flux scenarios – one saturating the current observational upper bound and one saturating the cascade limit (cf. Fig. 7.1 (bottom)).

| | $\sum_\alpha \triangle (N_{\nu_\alpha} + N_{\bar{\nu}_\alpha})$ | | | | | |
|---|---|---|---|---|---|---|
| energy decade | $10^{21 \div 22}$ eV | | $10^{22 \div 23}$ eV | | $10^{23 \div 24}$ eV | |
| year | 2008 | 2013 | 2008 | 2013 | 2008 | 2013 |
| observ. limit | 240 | 700 | 30 | 90 | 2 | 5 |
| cascade limit | 13 | 40 | 3 | 10 | 1 | 2 |

In the following we first present some benchmark flux scenarios and discuss the observability of the dips. Then, we examine experimental issues, which we have left out so far – and which most of them complicate the detectablity of neutrino dips.

## 7.3.1 Benchmark Flux Scenarios

### Most Optimistic Scenario - Hidden Sources

The most optimistic scenario for neutrino dip detection is an EEC neutrino flux, which saturates the present-day observed upper bound. This kind of flux can only be provided by a "hidden" source.

To optimize further, we start with a quasi-degenerate neutrino mass spectrum. Therefore, the neutrino mass is given by $m_{\nu_1} > 0.1$ eV, and the corresponding resonance energy is $E^{\text{res}} < 4 \times 10^{22}$ eV.

As can be seen from Fig. 7.1 and Tab. 7.1, the number of neutrino events observed by the year 2013, in the appropriate energy interval $10^{21} \div 10^{22}$ eV amount to a total of 700, summing over all flavors and particles as well as antiparticles. This implies a 1-$\sigma$ fluctuation of $\sqrt{N} \simeq 26$. For a 3-$\sigma$ evidence, we need an absorption-depth of $3\sqrt{N}/N \simeq 11$ %, and for a 5-$\sigma$ discovery, a depth of $5\sqrt{N}/N \simeq 19$ %.

Based on the analysis of the last section and figures within, we can deduce, which class of source could produce a dip with the appropriate depth. For example, power law emissivities with $n - \alpha \gtrsim 0$ and/or $z_{\max} \gtrsim 10$ fulfill the requirements (see Fig. 7.6 – 7.9, upper panel). What class of sources in "real nature" feature these properties? Astrophysical sources produce by no means such a flux, since they are transparent. A topological defect, which couples to Standard Model particles only indirectly may provide such a high flux at these extreme energies. As an example for this type of
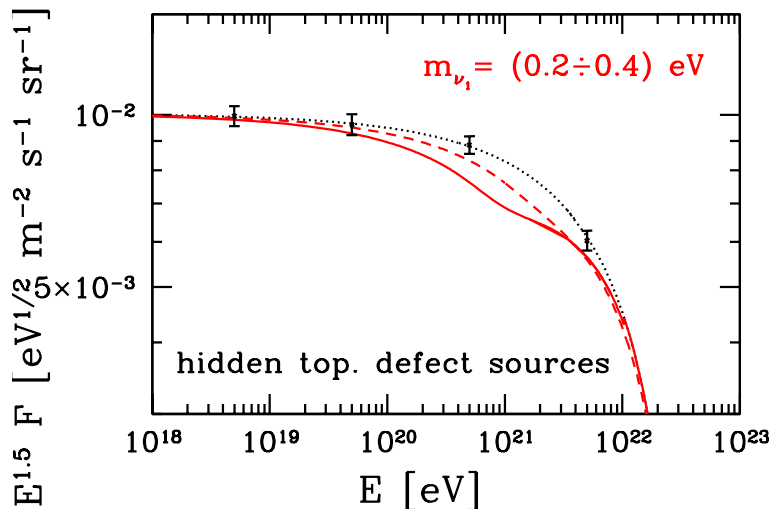
Figure 7.15: Predicted neutrino flux at Earth, summed over all flavors, from a power-like source emissivity, with $n = 1.5$, $z_{max} = \infty$, $\alpha = 1.5$, and $E_{max} = 4 \times 10^{22}$ eV, mimicking a hidden-sector topological defect source with $M_X = 4 \times 10^{14}$ GeV (cf. Fig. 7.1 (bottom)). This flux is also sufficient to explain the EHECR's above $E_{GZK}$ via the $Z$-burst mechanism. Curves are without (dotted) and with relic neutrino absorption for degenerate neutrino masses $m_{\nu_1} = 0.2$ eV (dashed) and $m_{\nu_1} = 0.4$ eV (solid). The error bars indicate the statistical accuracy achievable per energy decade by the year 2013, for a flux which saturates today's observational bound, see Fig. 7.1 (bottom).

source, Fig. 7.15 shows the resulting flux at Earth. It exhibits a significant wiggle due to neutrino absorption. We have taken the energy scale $M_X = 4 \times 10^{23}$ eV – by design, the flux gets maximal and saturates the observed upper bound – see Fig. 7.1. The source parameters are characteristic for a topological defect, $n = 3/2$ and $\alpha = 3/2$. The neutrino mass is chosen to be $m_{\nu_1} = 0.4$ eV (solid) and $m_{\nu_1} = 0.2$ eV (dashed), respectively. The indicated error bars show the statistical significance that is expected with planned and proposed experiments by the year 2013 (cf. Fig. 7.1 (bottom)). These dips reach a depth of about 18 % see Fig. 7.8, which implies, that the realization of this scenario would lead us close to discovery of the C$\nu$B by 2013 !

If the neutrino mass pattern is hierarchical, the dips become separated and thus shallower and, in addition, the masses are smaller in this case, therefore the flux at the largest resonance energy is lower. In numbers this means: If $m_{\nu_1} \lesssim 0.04$ eV, the lowest resonance energy, belonging to the heaviest neutrino, is $E_3^{res} \sim 10^{23}$ eV. From Tab. 7.1 we see, even for a flux reaching the observational limit, not more than 90 events are expected by 2013 in the corresponding energy interval $10^{22} \div 10^{23}$ eV. Therefore, the depth of the dip is required to be 32% for a 3-$\sigma$-evidence, and 53 %

for a 5-$\sigma$-discovery a 53 %. Checking Fig. 7.8, we notice, that such depths are not expected. If nature provides this kind of scenario, for the observation of the dips an increase of statistics is mandatory.

**Less Optimistic Scenario: Transparent Sources**

If the sources are transparent, the absolute flux is restricted to the cascade limit (see Fig. 7.1). The corresponding event numbers per energy decade are given in Tab. 7.1. For such a flux, 40 events are expected in the energy bin $10^{21} \div 10^{22}$ eV observed by 2013. This implies a required absorption depth of 47 % (79 %) for a 3-$\sigma$ evidence (5-$\sigma$ discovery). As shown in Fig. 7.5 and Fig. 7.8, this kind of dips are only possible for the extreme parameter ranges $n - \alpha \gtrsim 2$ and $z_{\max} \gtrsim 20$. For bottom-up sources, the first condition can be achieved, the second can not. For top-down sources, the second condition is likely to be achieved, but the first one fails. There are no predicted sources which fulfill both conditions.

However, the statistics may be increased by undertaking more ANITA flights, extending the EUSO flight time or by developing OWL or SalSA. The increase of statistics by a factor of 10 reduces the required absorption depth by a factor of $\sim 3$, that is a depth of 15% for a 3-sigma evidence and $\sim$ 25% for a 5-sigma discovery. If pre-2008 experiments detected the $\sim 13$ neutrino events predicted for a flux saturating the cascade limit, such extentions of EEC$\nu$ experiments would be strongly motivated.

Which kind of source provides a flux, which saturates the cascade limit at the required energies? Bottom-up sources in principle can do, if $E_{p\,\max} \gtrsim 10^{23}$ eV. Topological defects with $M_X \gtrsim 10^{14}$ GeV, would be another candidate.

As examples, we show in Fig. **??** and Fig. 7.16 the predicted dips for various neutrino mass pattern. Note, that $E_{\max}$ is chosen to be larger than in the hidden source scenario (simply because it fits into the limits, see Fig. 7.1) therefore more individual dips can be seen in the spectrum. The error bars indicate the statistical accuracy achievable by 2013 at 3-$\sigma$. In order to establish absorption dips, an increase in statistics of $10 \div 100$ is necessary, such that the error bars are reduced by a factor of $3 \div 10$. Moreover, a quasi-degenerate neutrino mass spectrum is required.

## 7.3.2   Further Experimental Issues

Three further issues mitigate the experiments ability to cleanly reconstruct an absorption dip: (i) The resolution with which the initial neutrino energy can be cleanly reconstructed from the visible event energy (ii) the flavor dependent nature of the energy reconstruction (iii) the ambiguity in the origin of a deviation from the assumed powerlaw spectrum due to absorption or due to other effects. We will discuss each of this in turn.

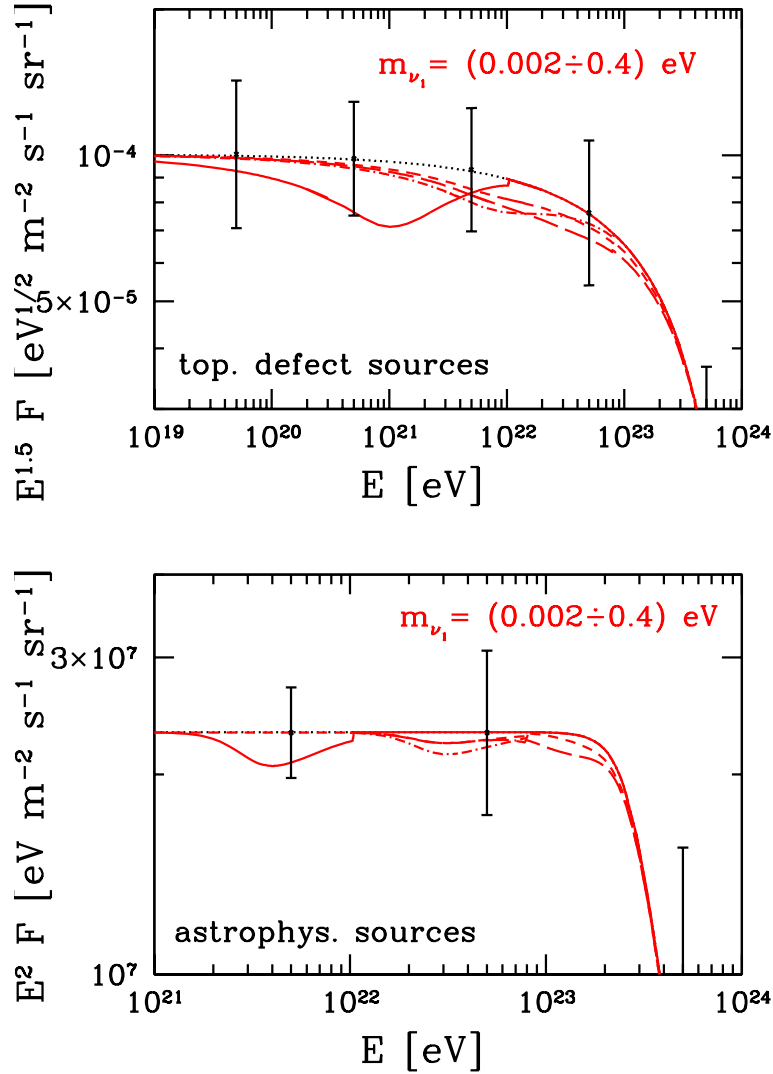Proposed EEC$\nu$ experiments will measure the shower energy from ground based scin-

Figure 7.16: *Top:* As in Fig. 7.15, but with $E_{max} = 10^{24}$ eV, to mimic topological defects with $M_X = 10^{16}$ GeV (cf. Fig. 7.1 (bottom)). The assumed neutrino spectra are: (i) quasi-degenerate, $m_{\nu_1} = 0.4$ eV (solid), (ii) normal hierarchical, $m_{\nu_1} = 0.01$ eV (long-dashed) and $m_{\nu_1} = 0.002$ eV (short-dashed), and (iii) inverted hierarchical, $m_{\nu_1} = 0.002$ eV (dashed-dotted). The error bars indicate the statistical accuracy achievable per energy decade by the year 2013, for a flux which saturates today's cascade limit from Fig. 7.1 (bottom).
*Bottom:* As above, but with a generous SFR activity (7.25), $z_{max} = 20$, injection spectrum index $\alpha = 2$, and $E_{max} = 10^{24}$ eV, to mimic astrophysical sources with $E_{p\,max} = 2 \times 10^{16}$ GeV.

tillator or water, atmospheric nitrogen fluorescence or radio signals in ice, salt or from the moons regolith. The energy reconstruction is expected to have error of about 25%. Our analysis, which is based on events per decade, and therefore should be compatible with this resolution.

The final state neutrinos in NC events and the produced charged leptons in $\nu_\mu$, $\nu_\tau$ CC events are generally unobservable and carry away about 80% of the energy – with some event by event variance. The $\nu_e$ CC events will produce a hadronic jet plus an electron, which creates an electromagnetic jet, and so the interaction deposits 100% of the incident energy in the combined showers. Therefore, we observe a superposition of two event types, where for only one of the two the observed energy is displaces by a factor of $\sim 0.2$ with respect to the initial neutrino energy. Knowing the CC/NC ratio and assuming equal neutrino fluxes for all flavor, a sufficient correction for this effect seems feasible in the case of appropriate statistics.

It was mentioned earlier in this work, that the deviation from an otherwise power-like spectrum near the high energy end of the spectrum may be due to differences among the individual contributing sources. To assure the occurring feature to be a real absorption dip, the spectrum above the dip region should be measured. This implies the requirement for more events at higher energies than discussed before. To ensure to observe an absorption dip, again these facts demand for a low resonance energy, and therefore for quasi-degenerate neutrino masses.

## 7.4   Conclusion

The detection of the cosmic neutrino background by means of the observation of dips in the EEC$\nu$ flux may be feasible. If observed, $Z$-dips are rich in particle and astroparticle physics information. We would like to emphasize, that the absorption due to the weak interactions on the C$\nu$B leave a characteristical fingerprint in the EEC$\nu$ flux, most sensitive to the individual neutrino masses.

The necessary condition for the dips to occur, is, that there is a EEC$\nu$ flux at resonance energy, which imposes a requirement on the neutrino mass spectrum and the energy range of the source.

For the dips to be resolved, the depth of the dip and the magnitude of the flux must be sufficiently large. Where the necessary condition will never relax, the statistics can be increased, when more event samples are provided. EEC$\nu$ experiments in this energy region are mainly based on radio detection, which is a rapidly evolving field. Large event samples $N \gg 100$ beyond an energy of $\sim 10^{21}$ eV are needed to reveal the dips with statistical significance. To get these event numbers, large fluxes are required, at least as large as the cascade limit, most probable, larger fluxes are necessary.

Most probably a quasi-degenerate neutrino mass spectrum is needed, to get a detectably deep dip at an possibly-accessible energy. Other experiments may prove the mass spectrum independently. The tritium beta decay experiment KATRIN has claimed to reach a limit of $m_\nu \sim 0.2$ eV.

The above discussion of statistical significance is restricted to the currently confirmed sensitivities of Fig. 7.1 (bottom). The Westerbork radio observatory may offer to improve the event rates by nearly 4 orders of magnitude in the energy region $5 \times 10^{21}$ eV to $10^{24}$ eV within 1 year [113].

Furthermore, if neutrino dips are perfectly resolved, their diagnostic potential is large. They deliver information about neutrino properties and about the source features as shortly summarized in the following.

The high energy tail of the dip determines the neutrino mass, if quasi-degenerate. If the neutrino mass spectrum is non-degenerate, but the dips are sufficiently separated, the neutrino masses can be determined individually.

The low energy edge of the dip might determine the point in time, about when the sources started to emit neutrinos. Furthermore, the characteristical shape may discriminate between astrophysical sources and topological defects.

If flavor discrimination in $\nu_e$-$\nu_{\mu,\tau}$ is established, one can distinguish between an inverted and a normal hierarchy by observation of the dip of the lowest resonance energy solely.

A large neutrino asymmetry $\xi \sim 2.6$ may be ruled out by observation of absorption dips, whereas a small asymmetry $\xi \sim 0.22$ does not change the resulting EEC$\nu$ flux significantly in comparison to $\xi = 0$.

# Chapter 8

# Conclusions

Merging the results for the considered approaches, a C$\nu$B detection plan can be outlined as follows.

(i) The EEC$\nu$ flux necessary for a $Z$-burst will be confirmed or refuted by the year 2008 – or even earlier, if we include the Westerbork sensitivity. In case of refutation, the $Z$-burst is ruled out as the only explanation of the UHECR events beyond the GZK cutoff. In case of confirmation, this result will strongly suggest the $Z$-burst scenario with a prediction of $m_{\nu_3} \sim 0.3$ eV and, whose subsequent analysis would require an independent determination of the heaviest neutrino mass – be it by tritium beta decay experiments, by cosmological measurements or via the detection of $Z$-dips in the EEC$\nu$ flux.

(ii) The realization of a $Z$-burst implies most probably a C$\nu$B detection by the year 2013 via absorption dips in the EEC$\nu$ spectrum.

In general, the possibility to detect absorption dips is dependent on the neutrino mass pattern as well as the source parameters. For the statistics to be sufficient for C$\nu$B detection within the next decade, a flux as large as the cascade limit or even above seems to be required – this condition might be relaxed by not yet confirmed improved sensitivities of upcoming experiments, e.g. the Westerbork radio observatory.

Almost certainly, a quasi-degenerate neutrino mass spectrum is required for the dip to emerge at an accessible energy and with a detectable depth.

It may be noted, that if perfectly resolved, the absorption dips could provide detailed information about the sources and reveal neutrino properties. Due to the latter, the observation of absorption dips can be claimed to be the most solid proof of the existence of the C$\nu$B considered upto now.

(iii) For the detection of the anisotropic relic neutrino flux at Earth by elastic scattering on nuclei in a torsion balance experiment, experimental progress beyond the estimates for the next decade is required.

(iv) C$\nu$B detection via inverse beta decay at hadron colliders presents no promising option for the conceivable future, since the LHC is excluded due to kinematical rea-

sons and a potential successor reaching the necessary energy is not expected to allow for measurable event rates.

# Acknowledgements

# Appendix A

# Elements of the EEC$\nu$ Flux Absorption
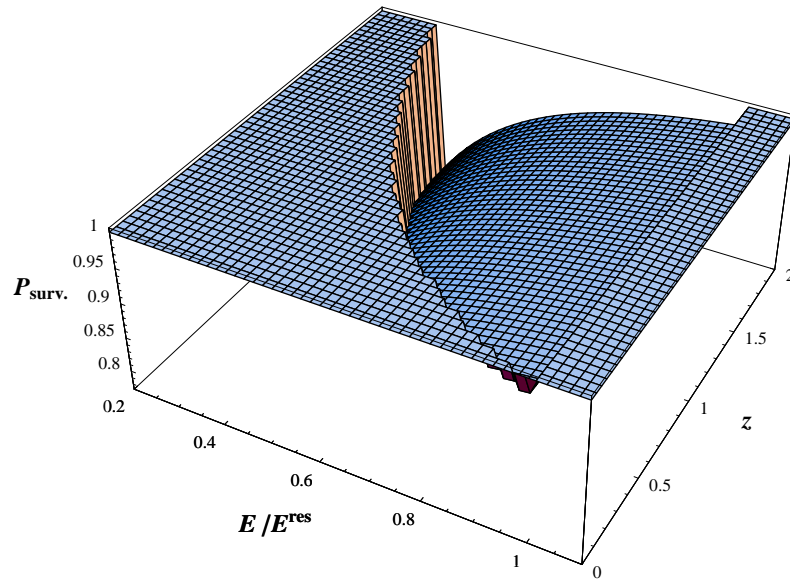
Figure A.1: The survival probability as a function of the relative energy $E/E^{\mathrm{res}}$ and the redshift $z$.
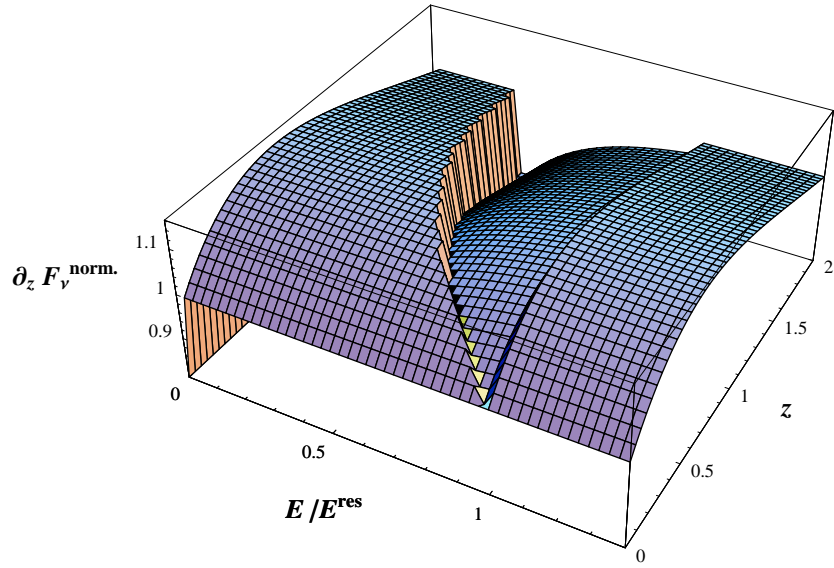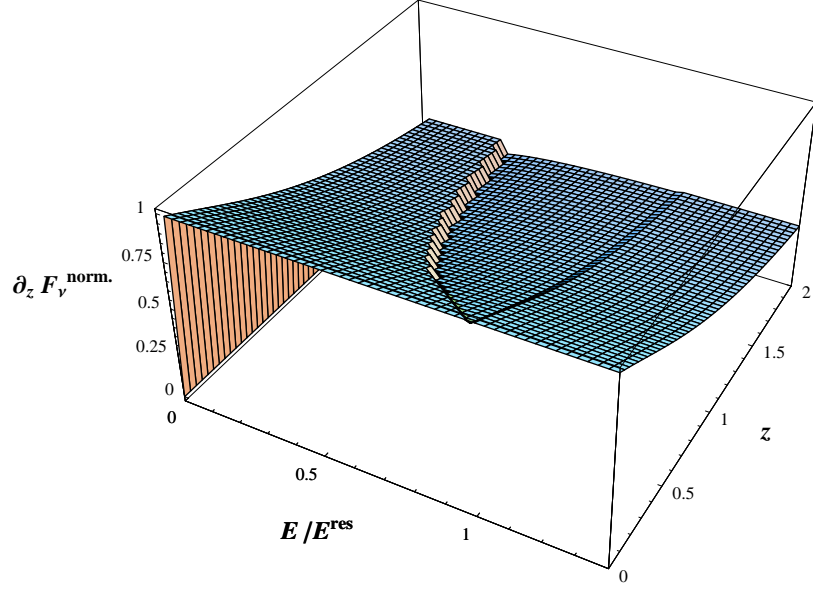
Figure A.2: 3-D figures in the $E/E^{\mathrm{res}}$-$z$-plane for the full integrand of the normalized flux in arbitrary units before performing the $z$ integration with the parameter choices $n - \alpha = 0, 1$ (from the top to the bottom) and $E_{\mathrm{max}}$ large.
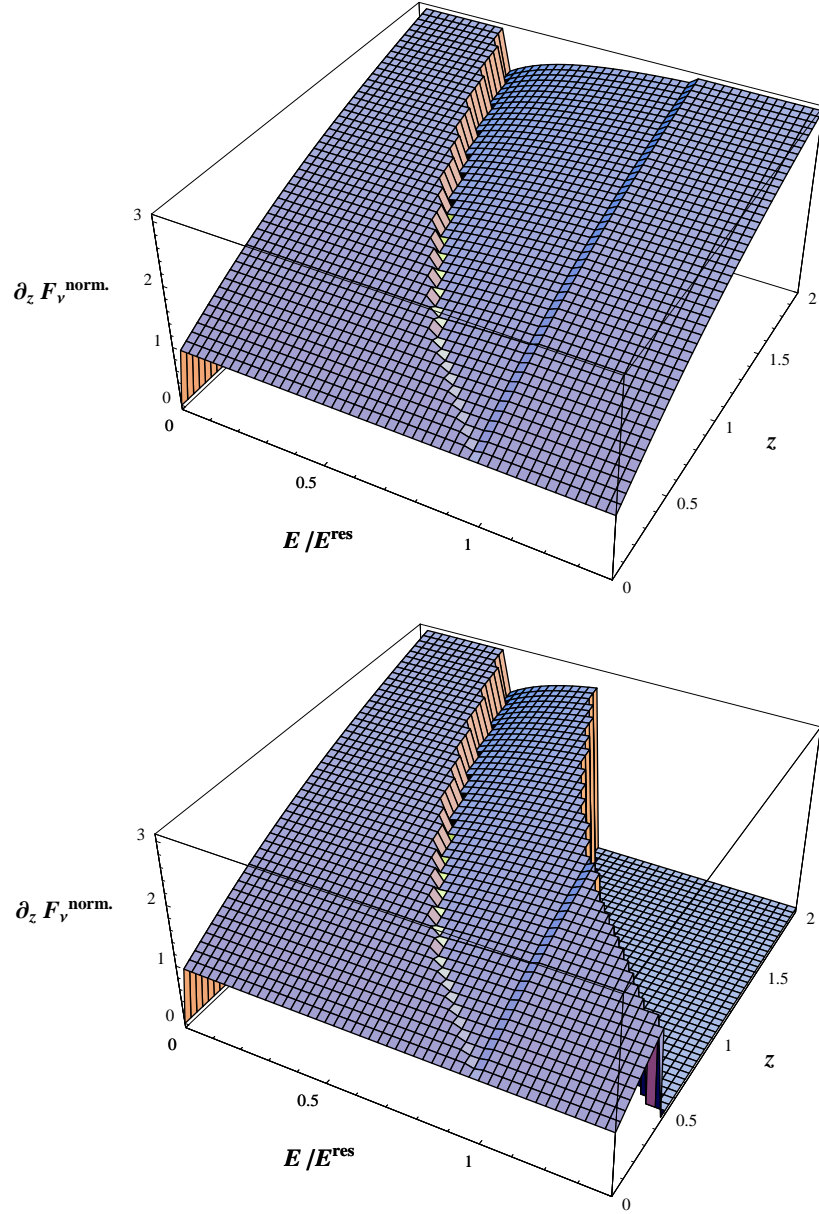
Figure A.3: 3-D figures in the $E/E^{\mathrm{res}}$-$z$-plane for the full integrand of the normalized flux in arbitrary units before performing the $z$ integration with the parameter choices $n - \alpha = 2$ and $E_{\mathrm{max}}$ large (top) and $n - \alpha = 2$ and $E_{\mathrm{max}} = 2\,E^{\mathrm{res}}$ (bottom).

# Appendix B

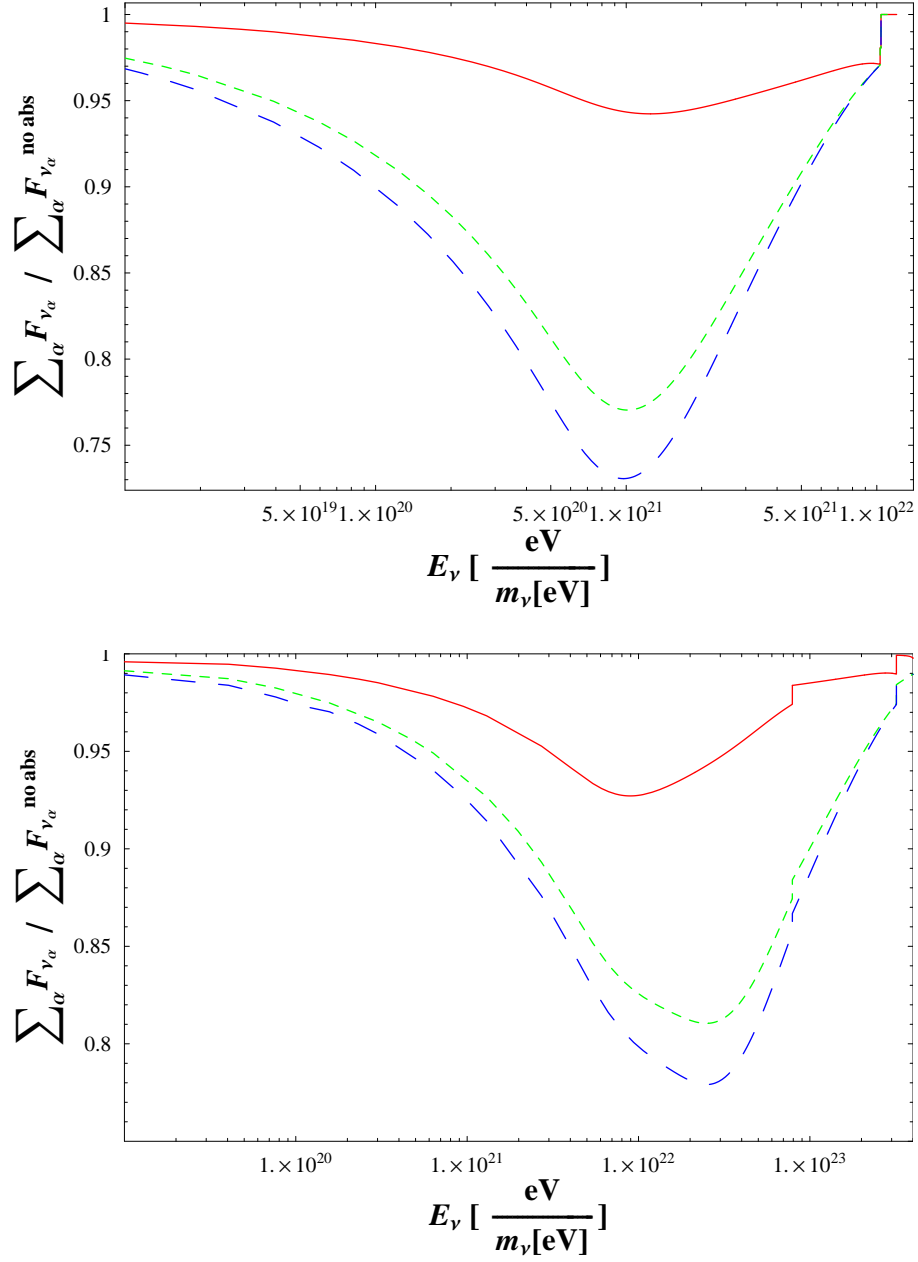# EECν Spectral Dips for Various Sources

Figure B.1: Predicted EEC$\nu$ flux arriving at earth normalized to a flux without absorption for the same mass parameters as in Fig. 7.8, but with $n - \alpha = 0$ and $z_{\max} = \infty$ and $E_{\max} = 1.4 \times 10^{22}$ eV (solid), $1.4 \times 10^{23}$ eV (dashed), $1.4 \times 10^{24}$ eV (long-dashed), (upper) $4.2 \times 10^{23}$ eV (solid), $4.2 \times 10^{24}$ eV (dashed), $4.2 \times 10^{25}$ eV (long-dashed), (lower), mimicking a topological defect source.
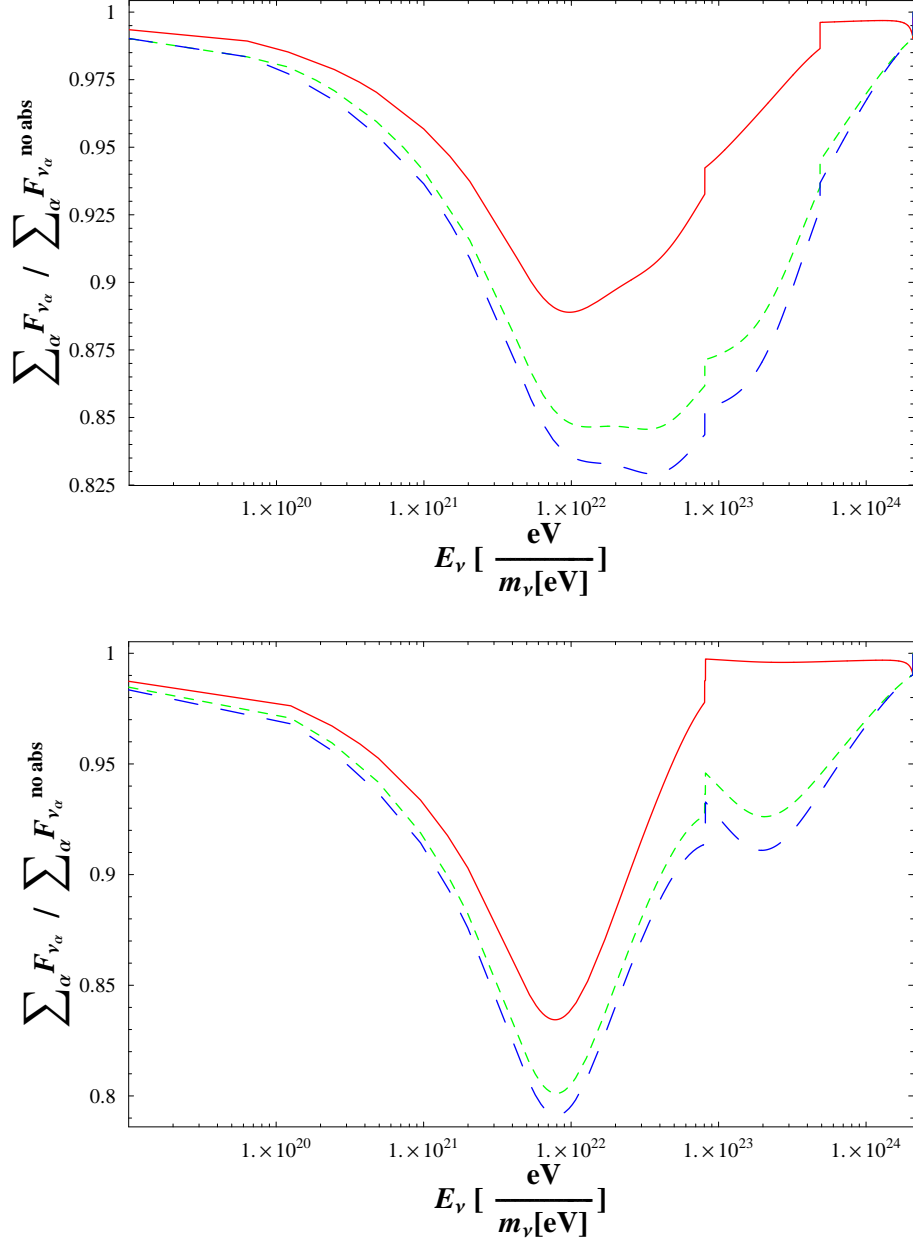
Figure B.2: Same as in Fig. B.1, but with $E_{\text{max}} = 2.2 \times 10^{24}$ eV (solid), $2.2 \times 10^{25}$ eV(dashed), $2.2 \times 10^{26}$ eV (long-dashed), (upper and lower), mimicking a topological defect source.

# Bibliography

[1] S. Eidelman *et al.* [Particle Data Group Collaboration], *Phys. Lett.* **B592**, 1 (2004).

[2] L. Wolfenstein, Phys. Rev. D **17**, 2369 (1978).

[3] S. P. Mikheev and A. Y. Smirnov, Sov. J. Nucl. Phys. **42**, 913 (1985) [Yad. Fiz. **42**, 1441 (1985)]. S. P. Mikheev and A. Y. Smirnov, Sov. Phys. JETP **64** (1986) 4 [Zh. Eksp. Teor. Fiz. **91** (1986) 7]. S. P. Mikheev and A. Y. Smirnov, Nuovo Cim. C **9**, 17 (1986).

[4] B.T. Cleveland *et al.*, *Astrophys. J.* **496**, 505 (1998); J. N. Abdurashitov *et al.* [SAGE Collaboration], *Phys. Rev.* **C 60**, 055801 (1999); W. Hampel *et al.* [GALLEX Collaboration], *Phys. Lett.* **B447**, 127 (1999); S. Fukuda *et al.* [Super-Kamiokande Collaboration], *Phys. Lett.* **B539**, 179 (2002); Q. R. Ahmad *et al.* [SNO Collaboration], *Phys. Rev. Lett.* **89**, 011301 (2002); **89**, 011302 (2002); T.A. Kirsten for the GNO Collaboration, *Nucl. Phys. Proc. Suppl.* **118**, 33 (2003); S. N. Ahmed *et al.* [SNO Collaboration], *Phys. Rev. Lett.* **92**, 181301 (2004).

[5] Y. Fukuda *et al.* [Super-Kamiokande Collaboration], *Phys. Rev. Lett.* **81**, 1562 (1998); A. Surdo [MACRO Collaboration], *Nucl. Phys. Proc. Suppl.* **110**, 342 (2002); G. Giacomelli and A. Margiotta [MACRO Collaboration], *Phys. Atom. Nucl.* **67**, 1139 (2004) [*Yad. Fiz.* **67**, 1165 (2004)]. M. Sanchez *et al.* [Soudan 2 Collaboration], *Phys. Rev.* **D 68**, 113004 (2003).

[6] M.H. Ahn *et al.* [K2K Collaboration], *Phys. Rev. Lett.* **90**, 041801 (2003).

[7] T. Araki *et al.* [KamLAND Collaboration], hep-ex/0406035; K. Eguchi *et al.* [KamLAND Collaboration], *Phys. Rev. Lett.* **90**, 021802 (2003).

[8] A. Aguilar *et al.* [LSND Collaboration], *Phys. Rev.* **D 64**, 112007 (2001).

[9] M. Maltoni, T. Schwetz, M. A. Tortola and J. W. F. Valle, hep-ph/0405172, and many references therein.

[10] O. Mena and S. J. Parke, Phys. Rev. D **69**, 117301 (2004) [arXiv:hep-ph/0312131].

[11] C. Kraus *et al.* European Physical Journal C (2003), proceedings of the EPS 2003 - High Energy Physics (HEP) conference.

[12] J. Angrik *et al.* [KATRIN Collaboration], FZKA-7090 `http://www-ik.fzk.de/katrin/`

[13] S. Hannestad, Eur. Phys. J. C **33**, S800 (2004) [arXiv:hep-ph/0310220].

[14] U. Seljak *et al.*, astro-ph/0407372.

[15] H. V. Klapdor-Kleingrothaus, I. V. Krivosheina, A. Dietz and O. Chkvorets, Phys. Lett. B **586**, 198 (2004) [arXiv:hep-ph/0404088].

[16] J. Drees, Int. J. Mod. Phys. A **17**, 3259 (2002) [arXiv:hep-ex/0110077].

[17] R. H. Cyburt, B. D. Fields, K. A. Olive and E. Skillman, Astropart. Phys. **23**, 313 (2005) [arXiv:astro-ph/0408033].

[18] A. Strumia, Phys. Lett. B **539**, 91 (2002) [arXiv:hep-ph/0201134].
T. Schwetz, arXiv:hep-ph/0311217.

[19] M. Sorel, J. M. Conrad and M. Shaevitz, Phys. Rev. D **70**, 073004 (2004) [arXiv:hep-ph/0305255].

[20] V. Barger, D. Marfatia and K. Whisnant, Phys. Lett. B **576**, 303 (2003) [arXiv:hep-ph/0308299].

[21] G. Barenboim and N. E. Mavromatos, JHEP **0501**, 034 (2005) [arXiv:hep-ph/0404014].

[22] E. W. Kolb and M. S. Turner, "The Early Universe".

[23] A. D. Dolgov, Phys. Rept. **370**, 333 (2002) [arXiv:hep-ph/0202122].

[24] G. Hinshaw *et al.*, Astrophys. J. Suppl. **148**, 135 (2003) [arXiv:astro-ph/0302217].

[25] M. Tegmark, arXiv:hep-ph/0503257.

[26] A. Ringwald and Y. Y. Y. Wong, JCAP **0412**, 005 (2004) [arXiv:hep-ph/0408241].

[27] S. S. Gershtein and Y. B. Zeldovich, JETP Lett. **4** (1966) 120 [Pisma Zh. Eksp. Teor. Fiz. **4** (1966) 174].

[28] S. Tremaine and J. E. Gunn, Phys. Rev. Lett. **42**, 407 (1979).

[29] W. Hu, D. J. Eisenstein and M. Tegmark, Phys. Rev. Lett. **80**, 5255 (1998) [arXiv:astro-ph/9712057].

[30] M. Tegmark *et al.* [SDSS Collaboration], Phys. Rev. D **69**, 103501 (2004) [arXiv:astro-ph/0310723].

[31] P. Crotty, J. Lesgourgues and S. Pastor, Phys. Rev. D **69**, 123007 (2004) [arXiv:hep-ph/0402049].

[32] V. Barger, J. P. Kneller, H. S. Lee, D. Marfatia and G. Steigman, Phys. Lett. B **566**, 8 (2003) [arXiv:hep-ph/0305075].

[33] S. Hannestad, JCAP **0305**, 004 (2003) [arXiv:astro-ph/0303076].

[34] S. Eidelman *et al.* [Particle Data Group], Phys. Lett. B **592** (2004) 1.

[35] S. H. Hansen, G. Mangano, A. Melchiorri, G. Miele and O. Pisanti, Phys. Rev. D **65**, 023511 (2002) [arXiv:astro-ph/0105385].

[36] A. D. Dolgov, S. H. Hansen, S. Pastor, S. T. Petcov, G. G. Raffelt and D. V. Semikoz, Nucl. Phys. B **632**, 363 (2002) [arXiv:hep-ph/0201287].

[37] Y. Y. Y. Wong, Phys. Rev. D **66**, 025015 (2002) [arXiv:hep-ph/0203180].

[38] K. N. Abazajian, J. F. Beacom and N. F. Bell, Phys. Rev. D **66**, 013008 (2002) [arXiv:astro-ph/0203442].

[39] L. Stodolsky, Phys. Rev. Lett. **34**, 110 (1975) [Erratum-ibid. **34**, 508 (1975)].

[40] N. Cabibbo and L. Maiani, Phys. Lett. B **114**, 115 (1982).

[41] P. Langacker, J. P. Leveille and J. Sheiman, Phys. Rev. D **27**, 1228 (1983).

[42] B. F. Shvartsman, V. B. Braginsky, S. S. Gershtein, Y. B. Zeldovich and M. Y. Khlopov, JETP Lett. **36**, 277 (1982) [Pisma Zh. Eksp. Teor. Fiz. **36**, 224 (1982)].

[43] P. F. Smith and J. D. Lewin, Phys. Lett. B **127**, 185 (1983).

[44] P. F. Smith, Nuovo Cim. A **83**, 263 (1984).

[45] I. Ferreras and I. Wasserman, Phys. Rev. D **52**, 5459 (1995).

[46] R. Opher, Astron. Astrophys. **37**, 135 (1974).

[47] R. R. Lewis, Phys. Rev. D **21**, 663 (1980).

[48] C. Hagmann, arXiv:astro-ph/9902102.

[49] G. Duda, G. Gelmini and S. Nussinov, Phys. Rev. D **64**, 122001 (2001) [arXiv:hep-ph/0107027].

[50] M. Honda, T. Kajita, K. Kasahara and S. Midorikawa, Phys. Rev. D **70** (2004) 043008 [arXiv:astro-ph/0404457].

[51] P. F. Smith, Phil. Trans. Roy. Soc. Lond. A **361** (2003) 2591.

[52] A. C. Melissinos, *Prepared for Conference on Probing Luminous and Dark Matter: Adrian Fest, Rochester, New York, 24-25 Sep 1999*

[53] T.-Mayer-Kuckuk, "Kernphysik" Teubner 1979, p.27 (2.1)-(2.7c)

[54] A. Ringwald, arXiv:hep-ph/0505024.

[55] D. Fargion, B. Mele and A. Salis, Astrophys. J. **517**, 725 (1999) [arXiv:astro-ph/9710029].

[56] T. J. Weiler, Astropart. Phys. **11**, 303 (1999) [arXiv:hep-ph/9710431].

[57] T. J. Weiler, Phys. Rev. Lett. **49**, 234 (1982);

[58] G. T. Zatsepin and V. A. Kuzmin, JETP Lett. **4**, 78 (1966) [Pisma Zh. Eksp. Teor. Fiz. **4**, 114 (1966)].

[59] K. Greisen, Phys. Rev. Lett. **16**, 748 (1966).

[60] S. C. Corbato *et al.*, Nucl. Phys. Proc. Suppl. **28B**, 36 (1992); R. U. Abbasi *et al.* [High Resolution Fly's Eye Collaboration], Phys. Rev. Lett. **92**, 151101 (2004) [arXiv:astro-ph/0208243]; T. Abu-Zayyad *et al.* [High Resolution Fly's Eye Collaboration], Astropart. Phys. **23**, 157 (2005) [arXiv:astro-ph/0208301].

[61] M. Takeda et al., Phys. Rev. Lett. 81 (1998) 1163; M. Takeda et al. [arXiv:astro-ph/9902239] N. Hayashida et al. Phys. Rev. Lett. 73 (1994) 3491; D. J. Bird et al. Astrophys J. 441 (1995) 144; Phys. Rev. Lett. 71 (1993) 3401; Astrophys. J. 424 (1994) 491; M. A. Lawrence, R. J. O. Reid and A. A. Watson, J. Phys. G. Nucl. Part. Phys. 17 (1991) 773; N. N. Efimov et al., Ref. Proc. International Symposium on *Astrophysical Aspects of the Most Energetic Cosmic Rays*, eds. M. Nagano and F. Takahara (World Scientific, Singapore, 1991), p. 20.

[62] http://www-akeno.icrr.u-tokyo.ac.jp/AGASA/

[63] Z. Fodor, S. D. Katz and A. Ringwald, JHEP **0206**, 046 (2002) [arXiv:hep-ph/0203198].

[64] A. Ringwald, physics Nucl. Phys. Proc. Suppl. **136**, 111 (2004) [arXiv:hep-ph/0409151].

[65] G. P. Zeller *et al.* [NuTeV Collaboration], Phys. Rev. Lett. **88**, 091802 (2002) [Erratum-ibid. **90**, 239902 (2003)] [arXiv:hep-ex/0110059].

[66] S. J. Brodsky, I. Schmidt and J. J. Yang, Phys. Rev. D **70**, 116003 (2004) [arXiv:hep-ph/0409279].

[67] S. Kretzer, arXiv:hep-ph/0405221. F. Olness *et al.*, Eur. Phys. J. C **40**, 145 (2005) [arXiv:hep-ph/0312323]. S. Kretzer, F. Olness, J. Pumplin, D. Stump, W. K. Tung and M. H. Reno, Phys. Rev. Lett. **93**, 041802 (2004) [arXiv:hep-ph/0312322].

[68] A. D. Martin, R. G. Roberts, W. J. Stirling and R. S. Thorne, Eur. Phys. J. C **35**, 325 (2004) [arXiv:hep-ph/0308087].

[69] S. Davidson, S. Forte, P. Gambino, N. Rius and A. Strumia, JHEP **0202**, 037 (2002) [arXiv:hep-ph/0112302].

[70] F. Abe *et al.* [CDF Collaboration], Phys. Rev. Lett. **79**, 2192 (1997).

[71] D. Buskulic *et al.* [ALEPH Collaboration], Z. Phys. C **66**, 3 (1995).

[72] M. Knecht and A. Nyffeler, Phys. Rev. D **65**, 073034 (2002) [arXiv:hep-ph/0111058].

[73] T. J. Weiler, Astrophys. J. **285**, 495 (1984).

[74] E. Roulet, Phys. Rev. D **47**, 5247 (1993).

[75] S. Yoshida, H. y. Dai, C. C. H. Jui and P. Sommers, Astrophys. J. **479**, 547 (1997) [arXiv:astro-ph/9608186].

[76] D. N. Spergel *et al.* [WMAP Collaboration], Astrophys. J. Suppl. **148**, 175 (2003) [arXiv:astro-ph/0302209].

[77] S. Hannestad, arXiv:hep-ph/0412181.

[78] Pierre Auger Observatory, http://www.auger.org/

[79] IceCube, http://icecube.wisc.edu/

[80] ANtarctic Impulse Transient Array,
http://www.ps.uci.edu/~anita/

[81] Extreme Universe Space Observatory,
http://www.euso-mission.org/

[82] Orbiting Wide-angle Light-collectors,
http://owl.gsfc.nasa.gov/

[83] A. Ringwald, T. J. Weiler and Y. Y. Y. Wong, arXiv:astro-ph/0505563.

[84] Saltdome Shower Array,
P. Gorham *et al.*, Nucl. Instrum. Meth. A **490**, 476 (2002).

[85] C. Spiering, J. Phys. G **29**, 843 (2003); private communication.

[86] J. G. Learned and S. Pakvasa, Astropart. Phys. **3**, 267 (1995);
L. Bento, P. Keranen and J. Maalampi, Phys. Lett. B **476**, 205 (2000);
H. Athar, M. Jezabek and O. Yasuda, Phys. Rev. D **62**, 103007 (2000).

[87] Radio Ice Cerenkov Experiment,
http://www.bartol.udel.edu/~spiczak/rice/rice.html

[88] Goldstone Lunar Ultra-high energy neutrino Experiment,
http://www.physics.ucla.edu/ moonemp/public/

[89] Fast On-orbit Recording of Transient Events satellite,
A. R. Jacobson, S. O. Knox, R. Franz and D. C. Enemark, Radio Sci. **34**, 337 (1999).

[90] I. Kravchenko, astro-ph/0306408.

[91] P. W. Gorham, C. L. Hebert, K. M. Liewer, C. J. Naudet, D. Saltzberg and D. Williams, astro-ph/0310232.

[92] N. G. Lehtinen, P. W. Gorham, A. R. Jacobson and R. A. Roussel-Dupre, astro-ph/0309656.

[93] G. Barenboim, O. Mena Requejo and C. Quigg, Phys. Rev. D **71**, 083002 (2005) [arXiv:hep-ph/0412122].

[94] R. M. Baltrusaitis *et al.*, Phys. Rev. D **31**, 2192 (1985);
S. Yoshida *et al.* [AGASA Collaboration], in: *Proc. 27th International Cosmic Ray Conference*, Hamburg, Germany, 2001, Vol. 3, pp. 1142-1145;
L. A. Anchordoqui, J. L. Feng, H. Goldberg and A. D. Shapere, Phys. Rev. D **66**, 103002 (2002).

[95] M. Ackermann *et al.*, Astropart. Phys. **22**, 339 (2005).

[96] X. Bertou, P. Billoir, O. Deligny, C. Lachaud and A. Letessier-Selvon, Astropart. Phys. **17**, 183 (2002).

[97] P. Gorham *et al.*, [ANITA collaboration], Proposal SMEX03-0004-0019, April 19, 2003.

[98] S. Bottai and S. Giurgola [EUSO Collaboration], in: *Proc. 28th International Cosmic Ray Conference*, Tsukuba, Japan, 2003, pp. 1113-1116;
S. Bottai [EUSO Collaboration], to appear in: *Proc. Incontro Nazionale di Astrofisica delle Alte Energie*, Roma, May 15-16, 2003.

[99] P. Gorham, private communication.

[100] J. F. Beacom and N. F. Bell, Phys. Rev. D **65**, 113009 (2002).

[101] C. Giunti and M. Laveder, to be published in: *Progress in Quantum Physics Research*, V. Krasnoholovets (ed.), Nova Science Publishers, Inc., hep-ph/0310238.

[102] V. S. Berezinsky and A. Vilenkin, Phys. Rev. D **62**, 083512 (2000) [arXiv:hep-ph/9908257].

[103] V. Berezinsky, M. Narayan and F. Vissani, Nucl. Phys. B **658**, 254 (2003) [arXiv:hep-ph/0210204].

[104] B. Eberle, A. Ringwald, L. Song and T. J. Weiler, Phys. Rev. D **70**, 023007 (2004) [arXiv:hep-ph/0401203].

[105] S. D. Wick, C. D. Dermer and A. Atoyan, Astropart. Phys. **21**, 125 (2004) [arXiv:astro-ph/0310667].

[106] P. Madau, L. Pozzetti and M. Dickinson, Astrophys. J. **498**, 106 (1998) [arXiv:astro-ph/9708220].

[107] A. W. Blain, A. Jameson, I. Smail, M. Longair, J. P. Kneib and R. Ivison, Mon. Not. Roy. Astron. Soc. **309**, 715 (1999) [arXiv:astro-ph/9906311].

[108] P. Chen, T. Tajima and Y. Takahashi, Phys. Rev. Lett. **89**, 161101 (2002) [arXiv:astro-ph/0205287].

[109] H. Li, S. A. Colgate, M. Kusunose and R. V. E. Lovelace, arXiv:astro-ph/9812418.

[110] N. Li and B. Q. Ma, Phys. Rev. D **71**, 017302 (2005) [arXiv:hep-ph/0412126].

[111] V. S. Berezinsky and A. Y. Smirnov, Phys. Lett. B **48**, 269 (1974).

[112] K. Mannheim, R. J. Protheroe and J. P. Rachen, Phys. Rev. D **63**, 023003 (2001) [arXiv:astro-ph/9812398].

[113] J. Bacelar, Talk given at the International ARENA Workshop, May 17–19, 2005, Zeuthen, Germany,
http://www-zeuthen.desy.de/nuastro/arena/